The Effect of Pygmy Resonances in *p*-process Nucleosynthesis

by
Christoper T. Angell

A dissertation submitted to the faculty of the The University of North Carolina at Chapel Hill in partial fulfillment of the requirements for the degree of Doctor of Philosophy in the Department of Physics and Astronomy.

Chapel Hill
2008

Approved by:

Dr. Hugon J. Karwowski, Advisor

Dr. Anton P. Tonchev, Reader

Dr. Christian Iliadis, Reader

Dr. Jonathan Engel, Reader

Dr. Jim Rose, Reader

ABSTRACT

Christoper T. Angell

The Effect of Pygmy Resonances in *p*-process Nucleosynthesis.
(Under the direction of Dr. Hugon J. Karwowski.)

The γ-ray strength function (γSF) is a key component for calculating photodisintegration reaction rates used for the simulation of the *p*-process. During the *p*-process, the nucleus can be thermally excited lowering the threshold for photodisintegration, thus significantly enhancing the reaction rate for neutron photodisintegration. To calculate the (γ, n) reaction rates for excited states the γSF needs to be known below the neutron separation energy. The presence of a pygmy dipole resonance (PDR) near the neutron separation energy could further enhance the reaction rate. To study the low energy γSF, particularly the PDR, and its dependence on the neutron number, measurements to determine the γSF both above and below the neutron separation energy were done on ^{142}Nd and ^{150}Nd. To determine the γSF above the neutron separation energy the (γ, n) cross sections were measured near threshold for ^{142}Nd, and, for the first time, for ^{150}Nd. The (γ, n) measurements were made using the monoenergetic γ-ray beam at the AIST TERAS facility in Tsukuba, Japan. To determine the γSF below the neutron separation energy a new technique using nuclear resonance fluorescence was developed, and measurements were taken for ^{142}Nd at E_γ= 3.4 – 9.7 MeV, and ^{150}Nd at E_γ= 5.6 – 7.2 MeV. The experiment was performed using a polarimeter consisting of four Clover detectors at the mono-energetic γ-ray beam facility, HIγS, at the DFELL in Durham, NC. The results will be compared to theoretical calculations using the quasi-particle random phase approximation (QRPA), and the neutron number dependence of the low-energy E1 γSF, and the potential effects of the results on the *p*-process will be discussed.

To my wife, Kokoro, and our son.

ACKNOWLEDGMENTS

Many people on two continents contributed to this dissertation. Without their help none of it would be possible. First and foremost, I'd like to thank my advisor, Dr. Hugon Karwowski, for his constant guidance, support, and encouragement, and for bringing me into graduate school in the first place. With out him, this project would not have been possible. I am greatly indebted to him. I'd like to thank Dr. Anton Tonchev for teaching me many of the experimental techniques that I used through out the course of this project, and for the much effort he contributed to the experiments at HIγS. I am greatly indebted to Dr. Hiroaki Utsunomiya at Konan U. for providing the initial ideas for this project, inviting me to participate on the experiments in Japan, teaching me the experimental techniques of (γ, n) measurements, and much invaluable help and support. Borrowing an expression from Japanese, I carry a great *On* to him.

I'd like to also thank the many other members of the UNC nuclear group that have helped, especially Dr. Art Champagne for providing the funding for me to complete the research in Japan, and Dr. Christian Iliadis and Dr. Tom Clegg for the help they've provided through out the project, and for help from Dr. Mitzi Boswell, Samantha Hammond, Jeremy Tompkins, Charles Arnold, and Tim Daniels, and from the Duke side, Dr. Tony Hutcheson, Dr. Elaine Kwan and Dr. Gencho Rusev. I am very grateful for all the help I've received from individuals from Konan University in Kobe, especially Ayano Makinaga for helping me while I was in Japan, and coming to TUNL to participate on the (γ, γ') experiment, and bringing the ^{150}Nd target with her, and to Dr. H. Akimune, Dr. Shinji Goko, Takeshi Kaihori, and from the Advanced Institute of Science and Technology in Tsukuba, Dr. Hiroyuki Toyokawa. This project has truly been an international effort.

Special thanks go to Dr. Stephane Goriely of Universit Libre de Bruxelles, and Dr. Jorge Piekarewicz of Florida State University for providing theoretical calculations. I am much indebted to Dr. Jon Engel at UNC for the countless hours of discussion.

Contents

List of Tables

List of Figures

Chapter 1

Introduction

The primary motivation for this dissertation is to better understand the effect of the low-energy γ-ray strength function (γSF), and particularly the pygmy resonance, on the *p*-process by measuring the γSF both above and below the neutron separation energy for ^{142}Nd and ^{150}Nd. The γSF is measured above the neutron separation energy directly by measuring the (γ, n) cross-section, and below the neutron separation energy using nuclear resonance fluorescence (NRF). Recent measurements of a pygmy-like concentration of J=1 states in ^{142}Nd also gives strong motivation to attempt to determine the parity of these states using NRF. The results of these experiments will contribute to the understanding of the systematics of the properties of pygmy resonances. In addition, the measurements on ^{150}Nd are relevant in order to evaluate the background for potential $0\nu2\beta$ decay experiments.

The *p*-process is the stellar mechanism for producing certain proton-rich nuclei that are not produced in other neucleosynthesis processes. The primary reaction mechanism of the *p*-process is the photodisintegration of heavy seed nuclei, moving nuclei toward the proton-rich side of the valley of β-stability. This process has received renewed attention recently while the tools needed to study it have improved to a sufficient point to allow considerable progress to be made. However, it is still not well understood [Arn03], with critical data needed, much of which depends on the availability of monoenergetic γ-ray facilities.

Though simulating the *p*-process is a daunting task, involving more than 20,000 reactions

linking 2,000 nuclei, significant progress can be made by performing key measurements which constrain the models used to calculate the unknown reaction rates. In particular, the reaction rates are highly sensitive to the low-energy tail of the γSF. If the nucleus is thermally excited, the photodisintegration can proceed from an excited state, and the reaction rate for the excited state needs to be calculated. The reaction rate on excited states is connected to the γSF below the neutron separation energy via the Brink-Axel hypothesis [Moh03], which follows from the giant resonance being built on top of each excited state [Axe62]. This implies that the probability of absorption of a γ-ray depends only on the energy of the γ-ray. Since the *p*-process takes place in a high-T environment, on the order of 10^9 K, photodisintegration on excited states can potentially increase the reaction rate by a factor of 100 to 10000 [Moh07]. The γSF model typically used in calculations is a Lorentzian extrapolation from the peak of the giant resonance. However, the shape of the experimental low-energy γSF can depart significantly from that of a simple Lorentzian. Direct measurements of the low-energy γSF are therefore needed.

Measurements of any sub-threshold γSF enhancements, such as the pygmy dipole resonance (PDR) are of particular importance. Since the reaction can proceed from an excited state any sub-threshold enhancement in the γSF can have a drastic effect on the reaction rate, and therefore on the dynamics of the *p*-process. Additionally, a pygmy resonance in ^{150}Nd, if observed, will contribute greatly to understanding how the behavior of the pygmy resonance changes as the nucleus becomes deformed.

There is another interest in investigating the γSF in the Nd isotopes. ^{150}Nd is an ideal candidate for $0\nu2\beta$-decay experiments. Its high Q-value (3.37 MeV) places the $0\nu2\beta$-decay peak above natural background radiation in the detector, while, more importantly, the favorable nuclear matrix element and phase space factor results in the highest decay rate per value of effective neutrino mass [Che05]. There is a proposal to add Nd to the liquid scintillator in the next phase of the SNO experiment, called SNO++. If the proposal for SNO++ is approved, there will be a need for any cross-section data on ^{150}Nd. Given the low count rates of

$0\nu 2\beta$-decay experiments, many processes, even the most exotic ones, could contribute to the background, and they need to be known. Currently, there is no information on the low-energy γSF of ^{150}Nd.

The γSF above the neutron separation energy can be directly determined from the (γ, n) cross section. In addition, measuring the cross section close to threshold constrains the extrapolation of the γSF below the neutron separation energy. There have been recent attempts to measure the (γ, n) cross section close to the neutron separation energy on ^{142,150}Nd using activation with a bremsstrahlung beam, but the (γ, n) cross section could not be extracted in a model independent way with such a technique [Has08]. Using a mono-energetic γ-ray beam, the cross section can be obtained directly, and in a model independent way. Monoenergetic beams in the energy range of interest are now available at two facilities. One facility is the laser inverse-Compton scattering source at the National Institute of Advanced Industrial Science and Technology (AIST-LCS) in Tsukuba, Japan [Ohg91]. The other facility is the High Intensity γ-ray Source (HIγS) at Duke University in Durham, NC, USA [Lit97]. The (γ, n) cross section on ^{142}Nd and ^{150}Nd were measured at the AIST facility in collaboration with a group from Konan University lead by Dr. Hiroaki Utsunomiya. The cross sections were measured close to the neutron separation energy in both nuclei, from 9.8 to 13.3 MeV in ^{142}Nd, and from 7.4 to 11.3 MeV for ^{150}Nd in January, 2007. The measurements improve the precision of the known cross section for ^{142}Nd, and are the first direct measurement of the (γ, n) cross section for ^{150}Nd in the region from 9.5 MeV to the neutron separation energy.

The γSF below the neuron separation energy can be measured using the NRF technique. Traditional NRF experiments measure the resonant elastic scattering of γ-rays. The experiments measure the energy, spin, parity, and width of discrete states. Identifying the parity of the levels is important to determining the characteristics of the observed resonant states. The mono-energetic nature of the beam enables the measurement of any branching to the low-lying excited states. The branching from the initial state to the first excited state can be measured, as well as the depopulation of the first excited state. Understanding the branching pattern is an

important step in understanding the decay modes of high excited states. In addition, measuring the depopulation of the first excited state will give a signature of the total strength of states which are initially excited, yet have widths which are too small to directly measure with NRF. Individually they can not be observed, but collectively they can have a potentially large effect on the total photoabsorption cross section. NRF measurements on ^{142}Nd and ^{150}Nd were made at HIγS in December, 2007, and January, 2008. They comprise the first NRF measurements of ^{142}Nd and ^{150}Nd near the neutron separation energy, and the first attempt to determine the γSF below the neutron separation energy in both nuclei.

In summary, measuring the γSF in ^{142}Nd and ^{150}Nd will be valuable in a number of ways. First, the nuclear structure of the pygmy resonance can be studied. Second, the γSF will provide a direct input into in the *p*-process modeling. Third, it will test and constrain a critical part of the input into the statistical model used to calculate *p*-process reaction rates. And finally, it will provide cross-sections important for understanding the background of $0\nu2\beta$-decay experiments involving ^{150}Nd. The theoretical motivation and calculations for the experiments will be discussed in detail in Chapter 3. The experimental techniques for measuring the γSF above and below the neutron separation energy will be explained in Chapters 4 and 5, respectively. The results will be presented, and shown how the two different measurement techniques combine to create a consistent set of data in Chapter 6. Finally, implications for the *p*-process discussed in Chapter 7.

Chapter 2

p-process

2.1 Introduction

The process of producing the elements during the Big-Bang and in stellar interiors is referred to as nucleosynthesis. The elements up to Fe can be produced through a process of burning successively heavier elements to produe energy which occurs in various stages of stellar evolution. The primary methods of nucleosynthesis for the elements beyond Fe are the rapid-neutron capture and slow-neutron capture processes, called the *r*-process and the *s*-process, respectively. In the *r*-process, neutrons are captured on seed nuclei, and a series of β^--decays carries the neutron-rich nuclides back to the valley of stable isotopes observed in Nature. The rate of neutron capture greatly exceeds the rate of β^--decay. In the *s*-process, the rate of neutron capture is small compared to that of β^--decay, and the production of isotopes moves along the bottom of the valley of β-stability. The seed nuclei for those processes are isotopes pre-existing in the stellar environment either from a previous generation of stars, or possibly, for the lighter elements, isotopes generated in a previous stage of the star's life.

There are however 35 nuclei in the region between Fe and Pb which cannot be created via either the *s*- or *r*- processes. They are known collectively as the *p*-nuclides, with the common characteristic of being on the proton-rich side of the valley of β-stability, i.e. having a relatively large ratio of protons to neutrons. They can only be produced either by rapid

proton capture or by photodisintegration reactions from existing heavy seed nuclei generated earlier via the *s*- or *r*- process. These two processes are referred to as the *rp*-process, and the *p*-process, respectively. They are competing models of *p*-nuclide production. In type I x-ray burst models, the *rp*-process can account for the production of some of the light *p*-nuclides. This leaves only the process of photodisintegration to produce the heavier *p*-nuclides. The requirement of using heavy seed nuclei is supported by the observation that the *p*-nuclides abundances make up a relatively small (typically $\leq 1\%$) part of the total nuclide abundances [Arn03].

The conditions required for this process are three-fold. First, abundance of heavy seed nuclei in the region between Fe and Pb is needed. Second, the stellar environment must be hot enough to produce the required high-energy photons, but not so hot as to significantly photo-erode the heavy nuclei. This comes to a temperature range of about $1.5 \leq T_9 \leq 3.5$ where $T_9 = T/10^9$ K. Third, the process must be relatively short lived as to not photo-erode the entire population of heavy nuclei to lighter elements, which is about a time interval of 1 s. These conditions are met primarily in the O/Ne layers of type II supernovae [Arn03].

2.2 Reaction Rates

The photodisintegrations involved in the *p*-process consist of (γ, n), (γ, p), and (γ, α) reactions on heavy seed nuclei (see Fig. 2.1). The reaction rate for the (γ, j) reaction, where j is the emitted particle, is given by

$$\lambda_{(\gamma,j)}(T) = \int_0^\infty c\, n_\gamma(E,T)\, \sigma_{(\gamma,j)}\, dE, \tag{2.1}$$

where c is the speed of light, $\sigma_{(\gamma,j)}$ is the photo reaction cross-section, and $n_\gamma(E,T)$ is the thermal photon density. The thermal photon density is simply the Planck distribution, which

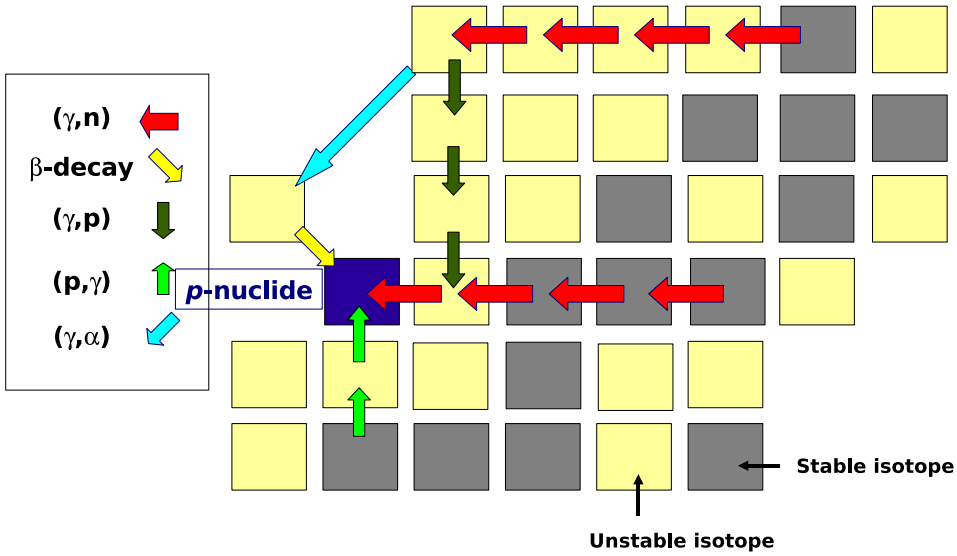

Figure 2.1: Possible reaction fbw to produce a *p*-nuclide. Many different paths can lead to the same *p*-nuclide, which necessitates knowing the reaction rates for all possible paths. This example shows four particular paths. To calculate the production of the *p*-nuclide from these four paths, 14 reaction rates and one β-decay rate need to be known.

is described by

$$n_\gamma(E,T) = \left(\frac{1}{\pi}\right)^2 \left(\frac{1}{\hbar c}\right)^3 \frac{E^2}{exp(E/kT)-1}, \tag{2.2}$$

where $n_\gamma(E,T)$ is the number of γ-rays per unit volume per unit energy. The pertinent nuclear physics component required is the reaction cross section in the energy range where the product of $n_\gamma(E,T)$ and $\sigma_{\gamma,x}(E)$ varies significantly from zero. This region is known as the astrophysical energy window of interest. This window for (γ,n) reactions varies little with temperature, and lies just above the neutron separation energy [Moh03]. The cross section for neutron photodisintegration must therefore be known near the neutron separation energy.

2.2.1 Thermal Excitation

Eq. 2.2 is valid only for reactions involving a single state of the target nucleus. In the high-T environment of a stellar explosion, the nucleus can be thermally excited, potentially populating many different levels distributed according to Boltzmann statistics [Moh04], and

Eq. 2.2 must be modified to take this into account. The average reaction rate weighted by the thermal excitation is given by

$$\lambda^{*}_{(\gamma,j)}(T) = \frac{\sum_{\mu}(2J^{\mu})\ \lambda^{\mu}_{(\gamma,j)}(T)\ exp(-\epsilon^{\mu}/kT)}{\sum_{\mu}(2J^{\mu}+1)\ exp(-\epsilon^{\mu}/kT)}, \tag{2.3}$$

where $\lambda^{\mu}_{(\gamma,j)}$ is the stellar reaction rate on the state μ with an excitation energy of ϵ^{μ}, and spin J^{μ} [Arn03]. The cross section for photodisintegration on the ground state of stable nuclei can be measured in the lab, but the cross sections on excited states needed to determine the stellar reaction rate cannot. They must be calculated using the statistical model (Hauser-Feshbach), and using the Brink-Axel hypothesis for the γSF (see Section 3.1.2). The γSF is the largest source of uncertainty for calculations of the (γ, n) cross sections on excited states [Moh03]. For reactions proceding on excited states, the thermal photon flux is much larger which greatly enhances the reaction rate. The thermally weighted reaction rate will be much higher than the reaction rate on the ground state by a factor of 100 to 10000 [Moh07].

Chapter 3

γ-ray Strength Function

3.1 Introduction

The γSF was introduced as a measure of the average reduced radiative width in analogy to the neutron strength function. The average decay widths obtained from very different experimental techniques can be compared using the γSF. The γSF is also useful as a direct input into reaction rate calculations, and to bridge the gap between experimental measurements and theoretical calculations.

In the early days of photodisintegration experiments, the photon excitation and decay widths were thought to come mainly from single particle transitions [Bri57]. The first experiments quickly established that the photoabsorption cross section was dominated by a single resonance excited by an E1 transition, termed the giant dipole resonance (GDR). It occurs in all nuclei with $A \geq 4$, and its excitation energy and strength vary smoothly across the chart of nuclides. Theoretical work showed that a collective dipole oscillation of the neutrons versus the protons in the excited nucleus could explain the observed properties of the GDR [Gol48, Ste50, Mye77].

The radiative widths below the peak of the GDR were first studied with neutron capture experiments, and very limited photon scattering experiments. However limited the early data were, it was seen that single particle estimates for low energies ($\leq$ 10 MeV) overpredicted the

observed strengths [Axe62]. With the data then available, Axel showed that radiative width data at excitation energy around 7 MeV were consistent with an extrapolation of the GDR to low energies assuming a Lorentzian shape of the GDR [Axe62]. The hypothesis that the GDR is described by a Lorentzian peak, and that the low-energy γSF is determined by an extrapolation of the Lorentzian tail is known as the Brink-Axel hypothesis. This hypothesis has several other useful implications which will be discussed in Sec. 3.1.2.

3.1.1 γ-ray Strength Function

The γSF is split into the upward strength function, $\overrightarrow{f}$, and the downward strength function, $\overleftarrow{f}$ [Rus08a]. The upward strength function is the reduced radiative width for populating excited states from the ground state. It is directly related to the photoabsorption cross section by the following expression:

$$\overrightarrow{f} \equiv \frac{\langle \Gamma_0 \rangle}{D \cdot \mathrm{E}_\gamma^{2L+1}} = \frac{3 \cdot \sigma_\gamma}{(\pi\hbar c)\mathrm{E}_\gamma^{2\mathrm{L}-1}}, \tag{3.1}$$

where $\langle \Gamma_0 \rangle$ is the average width of states in a region excited by a transition from the ground state, D is the average level spacing which is the inverse of the level density, E_γ is the energy, and L is the multipolarity of the transition. The upward γSF can be directly extracted from the photoabsorption cross section, σ_γ.

The downward strength function is the average reduced radiative width for decay to intermediate states:

$$\overleftarrow{f} \equiv \frac{\langle \Gamma_i \rangle}{D \cdot \mathrm{E}_\gamma^{2\mathrm{L}+1}}. \tag{3.2}$$

All symbols have the same meaning as in Eq. 3.1, except now $\langle \Gamma_i \rangle$ is the average width for decaying to state i, and E_γ is the transition energy to state i. The downward strength function is measured by observing the γ-ray cascade from an excited state, and is used in photodisintegration cross section calculations to obtain the branching ratios close to the neutron separation energy. Since the photoabsorption cross section is the observable needed for *p*-

process calculations, the upward strength function is the primary quantity considered in this project. Throughout this text, the terms γSF and photoabsorption cross section will be used interchangably, as they are directly related by Eq. 3.1.

3.1.2 The Brink-Axel Hypothesis

The Brink-Axel hypothesis centers around three key ideas, two of which were mentioned earlier: (1) that the GDR can be described by a Lorentzian curve, (2) that the low-energy γSF is determined from the extrapolation of the tail of the Lorentzian curve, and, finally, (3) that the radiation width should be the same regardless of the spin of the state for a given energy (as reported in [Kin57]). The last component of the hypothesis is essential for using the γSF to calculate the photodisintegration cross section on excited states, and comes from assuming that the GDR is built on each excited state. This assumption plays a very important role in *p*-process calculations. An important corollary follows that the upward and downward strength functions are equal. This leads to the conclusion that the average radiative width for absorbing and for emitting a γ-ray depends only on the γ-ray energy, and not on the initial or final state of the nucleus. The photoabsorption cross section for a nucleus in an excited state will then be the same as that for the ground state, with corrections for spin statistics. This leads to the reaction threshold being effectively lowered. Using this corollary of the Brink-Axel hypothesis in the *p*-process greatly simplifies the calculations (see Sec. 2.2.1).

Brink-Axel Hypothesis and Pygmy Resonances

The low-energy tail of the γSF can be modified by the presence of pygmy resonances (PR), so called because their strength is much smaller than that of the GDR. Traditionally, any enhancement above the Lorentzian extrapolation of the tail of the GDR has been called a pygmy resonance, but the mechanisms which produce those enhancements can differ for different nuclei [Gut05]. PR's have been observed in a broad range of nuclei, and the primary mechanism of the PR origin is thought to be collective excitations. Collective excitations

proposed to explain the pygmy resonance include oscillations of the neutron skin against an isospin symmetric core [Tso04, Pie06, van92], and has been termed the pygmy dipole resonance. A scissors mode where the neutrons and protons in a deformed nucleus vibrate by against each other in a scissors-like manner has also been proposed [Beu98]. Single particle states could play a role as well [Bos08]. Of concern to the *p*-process are pygmy resonances near the neutron separation energy which can increase the reaction rate on thermally excited states. The contributions of single particle states to the photoabsorption cross section do not follow the Brink-Axel hypothesis, and therefore should not be included in the γSF. However, the γSF should include PRs which are collective in nature, and can be built on excited states, like the GDR.

3.1.3 Models for the γSF

Formulae for Determining the γSF

While many forms of the γSF have been proposed, only the two main ones are considered here [Plu07]. The standard Lorentzian (SLO) was the first form proposed, and has been widely successful. It is given as

$$\sigma_{SLO} = \sum_i \frac{\sigma_i E_\gamma^2 \Gamma_i^2}{\left(E_\gamma^2 - E_i^2\right) + \Gamma_i^2 E_\gamma^2}, \tag{3.3}$$

where σ_i is the peak cross section of the i^{th} resonance, Γ_i the width, and E_i the energy, with the sum over the number of resonances needed to describe the total γSF. It reproduces very well the observed (γ, n) cross section data for the GDR over a large range of nuclei. Observations that the SLO overpredicts the low energy tail of the GDR in neutron capture experiments [Kop90] prompted modifications to the SLO. The most popular (and successful) of these is the Enhanced Generalized Lorentzian (EGLO) model. It introduces an energy dependent width which reduces the γSF in the region of the neutron separation energy, and then an extra phenomenological term to enhance the low energy tail of the GDR below 2 MeV to give the γSF

a non-zero value at $E_\gamma = 0$ MeV. It is given as [Plu07]:

$$\sigma_{EGLO} = \sum_i \sigma_i E_\gamma \Gamma_i \left[\frac{E_\gamma \Gamma_{k_i}(E_\gamma)}{\left(E_\gamma^2 - E_i^2\right) + E_\gamma^2 \Gamma_{k_i}^2(E_\gamma)} + \frac{0.7\Gamma_{k_i}(E_\gamma = 0)}{E_i^3} \right] \tag{3.4}$$

with the energy-dependent width given as

$$\Gamma_{k_i}(E_\gamma) = \left(\frac{\Gamma_i}{E_i^2} \right) \chi(E_\gamma) \left(E_\gamma^2 + 4\pi T_f^2 \right), \tag{3.5}$$

and

$$\chi(E_\gamma) = k + (1 - k) \frac{E_\gamma - \varepsilon_0}{E_i - \varepsilon_0}. \tag{3.6}$$

$\chi(E_\gamma)$ is obtained from an experimental fit to the data. The parameter k is scaled to give an agreement to the data at the reference energy of $\varepsilon_0 = 4.5$ MeV. The value of k depends on the choice of model for the nuclear level density, and for the Fermi gas model [Plu07], $k = 1$ for A < 148. For A ≥ 148,

$$k = 1 + 0.09(A - 148)^2 e^{-0.18(A-148)}. \tag{3.7}$$

The temperature used in Eq.3.5 is given as

$$T_f = \sqrt{\frac{B_n - E_\gamma - \delta}{a}}, \tag{3.8}$$

where δ and a are the level density parameters in the Back-Shifted Fermi gas model [vE05].

Phenomenological vs. microscopic models

If a Lorentzian shape is assumed, the γSF is determined by the parameters of the Lorentzian curve consisting of the maximum cross section, σ_r, the width, Γ_r, and the peak energy, E_r. Phenomenological models can be used to describe the properties of GDR over large mass regions with a minimal number of model parameters [Mye77]. The parameters are determined from global fits to the available data on GDR [Ber75]. This accurately determines the

properties of the GDR in regions where there have been measurements to constrain the model.

For astrophysical calculations models are needed which can calculate the properties of the GDR in nuclei far from β stability. In addition the models need to be able to accurately calculate the properties of pygmy resonances in a wide range of nuclei. Models with a microscopic basis can potentially be useful, but they needed to be tested and constrained. Much like a global fit to available data constrains phenomenological models, key measurements on significant predictions of microscopic models help to constrain and validate them.

The QRPA is one of such models which has had some some success in calculating the modifications in the tail of the GDR [Uts03]. The QRPA is a microscopic model which can calculate collective 1p-1h and 2p-2h excitations in a mean field approximation [Gor02]. Recent QRPA calculations predict an order of magnitude increase in the ratio of the low-energy γSF to the total γSF from the lightest to the heaviest stable Nd isotope [Gor07]. If observed this would be the largest relative increase in the low-energy γSF for any isotopic chain, and would constitute a key test of the QRPA.

3.2 Formalism of the γSF

The γSF is an expression of the average radiative width at a given energy. The upward γSF was defined in Eq. 3.1, being directly related to the photoabsorption cross section. For experiments measuring the total photoabsorption cross section below the neutron separation energy, a bridge must be made between the concept of individual resonances and that of the γSF, which is an average quantity. For experiments at HIγS, the beam has a finite width, and all states within that finite region will be excited, weighted by the beam profile. Using the formalism from [Ala87], the total photoabsorption cross section can be written as

$$\sigma_{\gamma T} = K \left\langle \Gamma_{\gamma 0} \right\rangle \tag{3.9}$$

where

$$K = g\left(\frac{10\text{MeV}}{E_\gamma}\right)^2 \frac{3.83\times10^4\text{mb}}{D}, \tag{3.10}$$

and E_γ is the incident γ-ray energy in MeV, D is the average level spacing in eV, $\left\langle\Gamma_{\gamma 0}\right\rangle$ is the average ground state radiative width, and $g = (2J_f + 1)/(2J_0 + 1)$ is the statistical spin factor with J_0 being the spin of the ground state, and J_f is the spin of the excited state. The formula for decay to the ground state is written as

$$\sigma_{\gamma\gamma} = K\left\langle\frac{\Gamma_{\gamma 0}^2}{\Gamma_T}\right\rangle, \tag{3.11}$$

where Γ_T is the total radiative width of the excited state. Similarly, the formula for branching to excited states is written as

$$\sigma_{\gamma\gamma i} = K\left\langle\frac{\Gamma_{\gamma 0}\Gamma_{\gamma i}}{\Gamma_T}\right\rangle, \tag{3.12}$$

where $\Gamma_{\gamma i}$ is the width for decay to excited state i.

The branching ratio for the ground state to the total photoabsorption cross section is given by

$$\langle b_0\rangle = \frac{\sigma_{\gamma\gamma}}{\sigma_{\gamma T}} = \frac{\left\langle\Gamma_{\gamma 0}^2/\Gamma_T\right\rangle}{\left\langle\Gamma_{\gamma 0}\right\rangle} = E\frac{<\Gamma_{\gamma 0}>}{<\Gamma_T>} \tag{3.13}$$

This is the same as is given as Eq. 3 in [Sch07]. On the right hand side, E is the enhancement factor for decay back to the ground state. It is defined as

$$E \equiv \frac{\left\langle\frac{\Gamma_{\gamma 0}^2}{\Gamma_T}\right\rangle}{\frac{\left\langle\Gamma_{\gamma 0}\right\rangle^2}{\langle\Gamma_T\rangle}}. \tag{3.14}$$

To calculate E, additional steps are needed, and assumptions must be made about the distribution of widths. As will be seen, E is related to the sum of the decay widths to excited states.

First, the total width can be written as a sum of the ground state and exciteted state widths,

$$< \Gamma_T >=< \Gamma_{\gamma 0} > + < \Gamma_c >, \tag{3.15}$$

where $\langle \Gamma_c \rangle$ is the average of the sum of radiative widths to all excited states. Defining $c \equiv \langle \Gamma_c \rangle / \left\langle \Gamma_{\gamma 0} \right\rangle$, the denominator of the right side of Eq. 3.13 can be re-written as

$$\frac{\left\langle \Gamma_{\gamma 0} \right\rangle}{\langle \Gamma_T \rangle} = \frac{1}{1+c}. \tag{3.16}$$

The ground state partial cross section can be re-written by using Eq. 3.13, 3.16:

$$\sigma_{\gamma\gamma} = \sigma_{\gamma T} \frac{E}{1+c} \tag{3.17}$$

The quantity c represents the ratio of the excited state decay widths to the ground state decay width. This separation is adopted because average quantities are being dealt with. An enhancement is expected for the entrance channel as states with a larger ground state width, and hence smaller width for decay to the excited states, will be preferentially excited. This is accounted for in Eq. 3.20 below. When the reaction is proceding from a state other than the ground state, the term “ground state” should be substituted for “initial state”. The formalism will be exactly the same as it is for the excitation of the ground state.

To obtain the average branching ratio in a small energy window ΔE, $\Gamma_{\gamma 0}^2 / \Gamma_T$ must be weighted by a probability distribution. Within the energy range ΔE, many states contribute to the reaction. For any one state, using Eq. 3.15 to rewrite Eq. 3.13, the branching ratio to the ground state is given by

$$b_0 = \frac{1}{\langle \Gamma_0 \rangle} \frac{\Gamma_{\gamma 0}^2}{\Gamma_{\gamma 0} + \Gamma_{\gamma c}}. \tag{3.18}$$

By letting $x = \Gamma_{\gamma 0} / \left\langle \Gamma_{\gamma 0} \right\rangle$. Eq. 3.18 then reduces to

$$b_0 = \frac{x^2}{x + c}. \tag{3.19}$$

The average branching ratio is then given by

$$\langle b_0 \rangle = \int_0^\infty \frac{x^2}{x + c} P(x) dx, \tag{3.20}$$

where $P(x)$ is the probability distribution of partial widths. A distribution used for partial widths that has been experimentally verified to be consistent with the distribution of neutron resonance widths, among other things, is the Porter-Thomas distribution [Por56]. The Porter-Thomas distribution is a χ^2 distribution with one degree of freedom. The χ^2 distribution, with $\rho = \nu/2$, where ν is the number of degrees of freedom, is given as

$$P(x;\rho)dx = \Gamma(\rho)^{-1} (\rho x)^{\rho - 1} e^{-\rho x} dx, \tag{3.21}$$

where $\Gamma(\rho)$ is the Gamma function which normalizes the distribution. Using the Porter-Thomas distribution, Eq. 3.20 reduces to [Axe70]:

$$\langle b_0 \rangle = \int_0^\infty \frac{3 e^{-\alpha\, c}}{(1 + 2\alpha)^{5/2}} d\alpha. \tag{3.22}$$

Once the ratio of width, c, is known (see Eq. 3.17), $\langle b_0 \rangle$ can be obtained from Eq. 3.22, and in turn E can be calculated as $E = (1 + c)\langle b_0 \rangle$. To obtain c, the partial cross sections to the excited states must be known.

Just as the entrance channel is enhanced by a factor E, the other channels leading to excited states must be reduced by a corresponding factor to keep the following identity true:

$$\left\langle \frac{\Gamma_{\gamma 0}^2}{\Gamma_T} \right\rangle + \sum_i \left\langle \frac{\Gamma_{\gamma 0} \Gamma_{\gamma i}}{\Gamma_T} \right\rangle \equiv \left\langle \Gamma_{\gamma 0} \right\rangle. \tag{3.23}$$

Using Eq. 3.14, and the following relation

$$\left\langle \frac{\Gamma_{\gamma 0}\Gamma_{\gamma i}}{\Gamma_T} \right\rangle = R\frac{\left\langle \Gamma_{\gamma 0} \right\rangle \left\langle \Gamma_{\gamma i} \right\rangle}{\langle \Gamma_T \rangle}, \tag{3.24}$$

where R is the reduction factor, Eq. 3.23 can be rewritten as

$$E\frac{< \Gamma_{\gamma 0} >}{< \Gamma_T >} + R\frac{\langle \Gamma_c \rangle}{\langle \Gamma_T \rangle} = 1. \tag{3.25}$$

This equation assumes that all inelastic widths are reduced by the same amount. Using Eqs. 3.15, 3.16, and 3.25, R can be written in terms of E and c:

$$R = \frac{1 + c - E}{c}. \tag{3.26}$$

The inelastic cross sections need to be rewritten in terms of R and $\sigma_{\gamma T}$. Following the definition for the ground state branching ratio, given in Eq. 3.13, the branching ratio for decay to state i can be written as:

$$\langle b_i \rangle = \frac{\sigma_{\gamma\gamma i}}{\sigma_{\gamma T}} = \left\langle \frac{\Gamma_{\gamma 0}\Gamma_{\gamma i}}{\Gamma_T} \right\rangle / \left\langle \Gamma_{\gamma 0} \right\rangle. \tag{3.27}$$

Using Eq. 3.24 and definition for c, this can be rewritten as

$$\sigma_{\gamma\gamma i} = \sigma_{\gamma T}\frac{R}{1 + c}\frac{\left\langle \Gamma_{\gamma i} \right\rangle}{\left\langle \Gamma_{\gamma 0} \right\rangle}. \tag{3.28}$$

The formalism developed here is needed to include the effect of the distribution of the partial widths on calculated partial cross sections. No assumptions have been made up to this point about the relationship of the partial widths to the γSF, but they have to be made to calculate c.

The Brink-Axel hypothesis (see Sec. 3.1.2) greatly simplifies the task of calculating the partial widths. Using this hypothesis, Eq. 3.9 is used to determine the partial width connecting

two states. The partial width from state i to state j is given as

$$\Gamma_{ij} \propto \left(E_i - E_j\right)^2 \sigma_{\gamma T}\left(E_i - E_j\right), \tag{3.29}$$

with the remaining portions of K dropped for clarity. Similarly, the partial ground state width of a state at E_γ is given as

$$\Gamma_{\gamma 0} \propto \left(E_\gamma\right)^2 \sigma_{\gamma T}\left(E_\gamma\right),$$

and the inelastic decay width is

$$\Gamma_{\gamma i} \propto \left(E_\gamma - E_i\right)^2 \sigma_{\gamma T}\left(E_\gamma - E_i\right).$$

Using Eq. 3.29, and defining $f_i = (E_\gamma - E_i)/E_\gamma$, the inelastic partial cross section, Eq. 3.28 can be re-written as:

$$\sigma_{\gamma\gamma i} = \sigma_{\gamma T}(E_\gamma - E_i)\frac{R}{1+c} f_i^2. \tag{3.30}$$

The parameter c can be obtained as follows:

$$(1+c) \equiv \frac{\langle \Gamma_T \rangle}{\left\langle \Gamma_{\gamma 0} \right\rangle} = \frac{\sum_i \sigma_{\gamma T}(E_\gamma - E_i) f_i^2}{\sigma_{\gamma T}(E_\gamma)}. \tag{3.31}$$

Because not all the levels are known experimentally, the sum in Eq. 3.31 needs to be replaced with an integral over the level density above some cut off energy, E_{cut}:

$$(1+c) = \frac{1}{\sigma_{\gamma T}(E_\gamma)} \left\{ \sum_i \sigma_{\gamma T}(E_\gamma - E_i) f_i^2 + \sum_{J^\pi} \int_{E_{cut}}^{E_\gamma} \sigma_{\gamma T}(E_\gamma - E_i) \left(\frac{E_\gamma - E'}{E_\gamma}\right)^2 \rho(E', J^\pi) dE', \right\} \tag{3.32}$$

where $\rho(E', J^\pi)$ is the spin and parity dependent level density. Only levels with certain values of J^π will be branched to, and a sum over states with those values of J^π is included in the equation. For the case of even-even nuclei and considering only states reached via E1 transitions, only $J^\pi = 0^+, 1^+$, and 2^+ were included.

The spin dependent level density can be written as

$$\rho\,(U, J, \pi) = \frac{1}{2}\rho(U) f(J), \tag{3.33}$$

where $\rho(U)$ is the total level density, and $f(J)$ is the spin-dependent component. Parity dependence is neglected, and it asssumed there is the same density of + and − parity states. The Back-Shifted Fermi Gas (BSFG) model [vE05] was used to calculate the level density in the present calculations. It is given as

$$\rho\,(U) = \frac{\mathrm{e}xp\left[2\sqrt{a\,(U - E_1)}\right]}{12\sqrt{2}\sigma a^{1/4}\,(U - E_1)^{5/4}} \tag{3.34}$$

where a is the level density parameter, E_1 is the energy backshift parameter, and σ is the spin-cutoff parameter, and is given by

$$\sigma^2 = 0.0146A^{5/3}\frac{1 + \sqrt{1 + 4a\,(U - E_1)}}{2a} \tag{3.35}$$

where A is the mass number. The spin dependent component depends on the spin-cutoff parameter,σ, and is written as

$$f(J) = e^{-J^2/2\sigma^2} - e^{-(J+1)^2/2\sigma^2}. \tag{3.36}$$

The constant temperature model was not used as its term for the distribution of J^π is constant with excitation energy, and gives unreasonably large values of c. The calculation of partial cross sections for ^{142,150}Nd using the formalism developed here will be discussed in Ch. 6.

3.3 Pygmy Resonances

To include the pygmy dipole resonance (or the scissors mode resonance) in the *p*-process nucleosynthesis calculations theoretical predictions of the strength are needed for a wide range

of nuclei. This is much like the case discussed above for the GDR, but the situation is complicated by a lack of knowledge of the precise mechanism producing pygmy resonances. To provide useful constraints for relevant microscopic models, a signature of the underlying structure is needed. In particular for the above mentioned resonances, a neutron skin oscillation would be excited via E1 transitions, and a scissors mode would proceed via M1 transitions. The difference in multipolarity of the transitions gives one signature of the underlying mechanism of the PR.

3.3.1 Systematics of Pygmy Resonances

Understanding the systematics of the PR can help guide theory, and enable preliminary tests of theoretical predictions, thereby discerning between different models. One example is the theory of a neutron skin oscillation. If the PR arises from the excitation of the neutron skin, then the properties of the PR should depend on the neutron skin thickness. The neutron skin thickness is roughly related to the ratio of N/Z. By looking at the PR parameters vs. N/Z an understanding for the role of the neutron skin in the PR could be obtained. If the PR parameters do correlate with N/Z, it will then stand as one piece of support for the theory of the neutron skin oscillation, and estimates for the strength of the PR can be made from the obtained systematics.

PR Excitation Energy Systematics

All available data as of December, 2006, were gathered to study the systematics of the PR (see Appendix 7). The data was taken from a number of different types of experiments including (γ,γ') [Vol06], (n,γ) [Iga86], inelastic scattering with ^{3,4}He beams [Sch00a], and Coulomb excitation [Adr05]. The parameters of the PR were plotted vs. the N/Z ratio. The excitation energy vs. N/Z can be seen in Fig. 3.1. The data is clearly separated into two groups. One trend, that is followed by the NRF data [Vol06], shows a slow change in mean PR energy with N/Z. The NRF data set consists only of even-even N=82 isotones, and comes from the

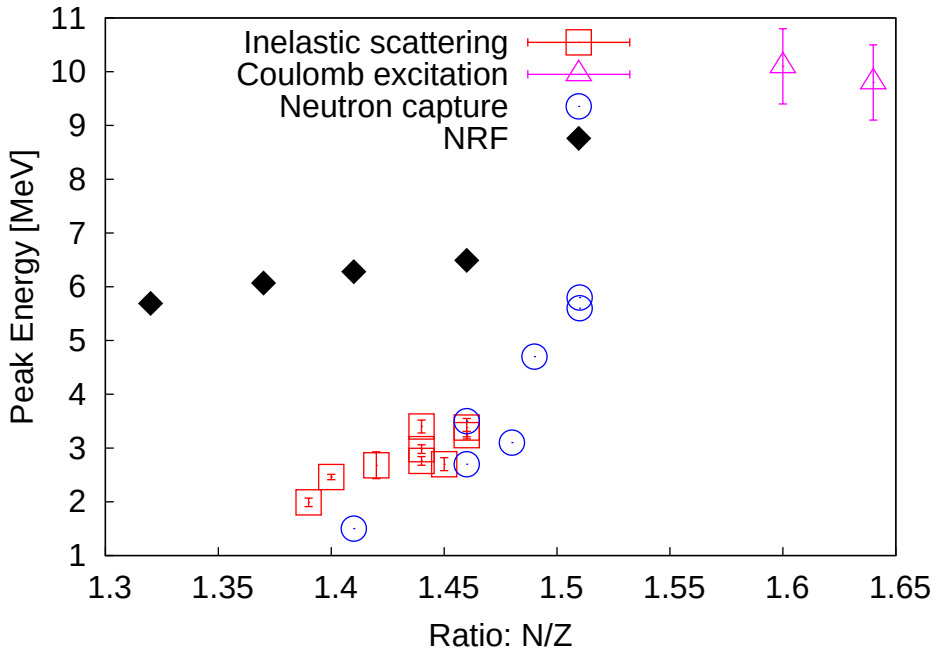

Figure 3.1: The PR excitation energy vs. N/Z. The data separates into two groups, one consisting of NRF data, the other non-NRF data. The x-intercept for the best-fit line in the non-NRF data is $N/Z \approx 1.35$. See Appendix 7 for tables of the parameters and references.

centroid of a clustering of observed individual states in the (γ, γ') process. The results of the second set of measurements which includes neutron capture and ^{3,4}He induced reactions, shows a stronger dependance of PR energy on N/Z. These sets encompass nuclei from ^{143}Sm to ^{198}Au, and includes even-even, even-odd, and odd-odd nuclei. The fit to this non-NRF set yields the following relation:

$$E_{PR} = 29 \left(\frac{N}{Z}\right) - 39 \text{ (MeV)}. \tag{3.37}$$

The straight line fit through this group includes the Coulomb dissociation data of ^{130,132}Sn [Adr05]. However, caution should be taken before classifying the two Sn isotopes with this group. Leaving the Sn isotopes out of consideration, there is still a strong correlation of the mean excitation energy of the PR and N/Z.

Several conclusions are possible. The NRF results are distinctly separate, and observed

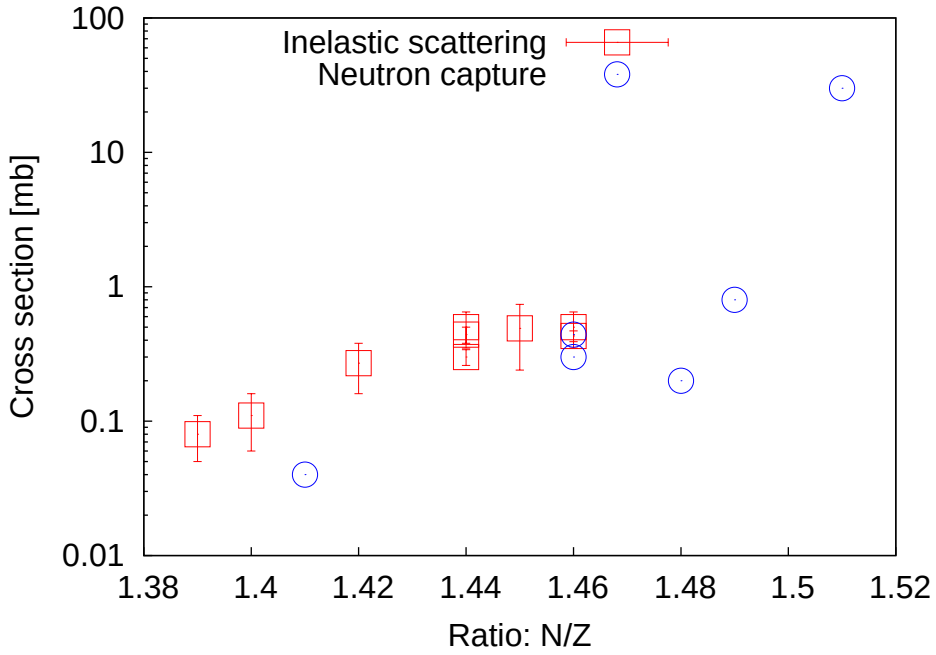

Figure 3.2: The PR cross section vs. N/Z. The total cross section for the pygmy resonance appears to be correlated with an increase in N/Z.

enhancement of strength may be primarily resulting from single particle excitations, with the clustering of levels following from the shell structure, probably being transitions to the $h_{9/2}$ neutron shell. If Eq. 3.37 is used to extrapolate to $E_{PR} = 0$, it occurs at $N/Z \approx 1.35$. This corresponds to the region of the Mo isotopes. A strong increase in the γSF as $E_\gamma \rightarrow 0$ has been measured in the Mo isotopes using ^{3,4}He scattering [Gut05]. In view of the emerging pattern, one can speculate that a resonance at very low energies in Mo could have the same origin as the PR in the heavier nuclei.

PR Cross Section and Width Systematics

The PR peak cross sections taken from a Lorentzian fit to the resonance is plotted vs. N/Z in Fig. 3.2 for a subset of the data shown in Fig. 3.1. As can be seen in the figure, there is a strong dependence of the PR cross section on the excitation energy. The point with the largest cross section at $\sigma_{max} \approx 30$ mb corresponds to ^{198}Au taken from Igashira *et al.* [Iga86]. A fit to

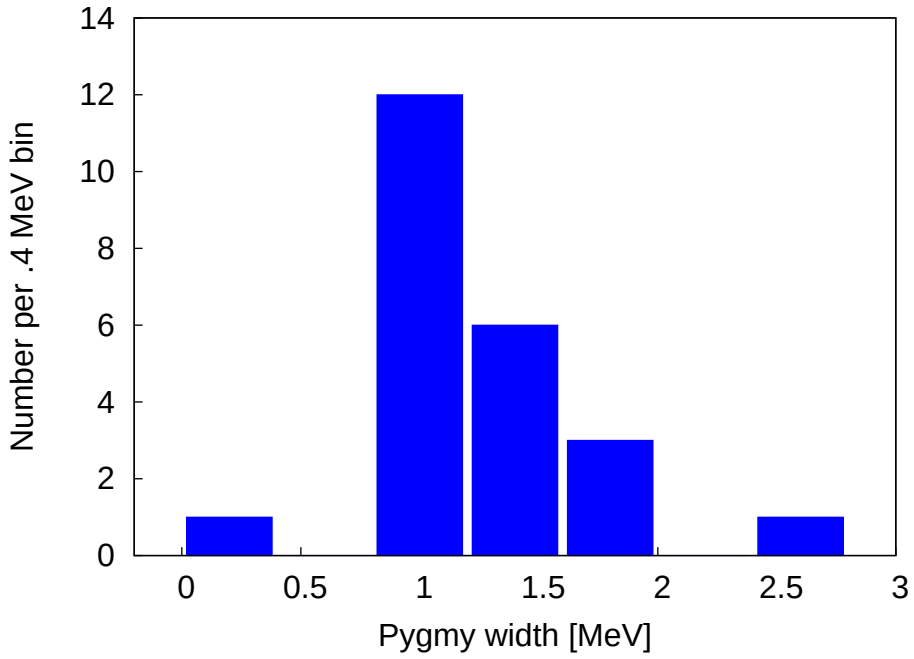

Figure 3.3: The PR width appears to cluster around 1 MeV.

the data excluding the ^{198}Au point yields the following relationship:

$$\sigma_{PR}^{max} = 5.2\left(\frac{N}{Z}\right) - 7.1 \text{ mb}. \tag{3.38}$$

The increase of the cross section with N/Z may point to the pygmy strength increasing as the neutron skin becomes thicker. A histogram of the observed PR widths is shown in Fig. 3.3. The widths cluster around 1 MeV. The pygmy dipole widths don't show a strong correlation with N/Z. This is consistent with what is known about the GDR as its width doesn't vary smoothly with A, but varies sporadically yet clustering around a single value.

Predictions for ^{142,150}Nd

Predictions can be made for ^{142,150}Nd using Eqs. 3.37 and 3.38. The results are summarized in Table 3.1. The predicted properties of the PR in ^{142}Nd place it in a region which can not be determined directly from photoabsorption data, and can only be measured in experiments

Table 3.1: Predictions for PR properties of ^{142,150}Nd.

Nucleus	N/Z	E_{PDR} [MeV]	σ_{PDR}^{max} [mb]
^{142}Nd	1.37	0.9	.02
^{150}Nd	1.50	4.6	.70

that probe the downward strength function. Any resonance seen in ^{142}Nd in the current NRF experiments would have to result from an underlying mechanism different than that which would explain the PR seen in the neutron capture and inelastic scattering experiments. The predictions for ^{150}Nd would place it below the region searched in the current experiments, but doesn't preclude the possibility of observing it.

Chapter 4

Experiments - (γ, n) Cross Sections

4.1 Introduction

The measurements of (γ, n) cross sections are essential to the understanding of the γSF, and contribute most to the γSF determination. The experimental technique used was developed in the 60's and 70's using in flight positron annihilation in a radiator as a quasi-monoenergetic γ-ray source. The experiments have been simplified since the 1970's by advancements in γ-ray production methods [Ber75]. The advent of monoenergetic inverse-Compton backscattering γ-ray sources has recently enabled the precision measurements of the (γ, n) cross-section near threshold. A compact 4π neutron detector, using the design developed in the 60's, was used to count neutrons from photodisintegration due to its high efficiency. All these developments contribute to the significant progress in precision photodisintegration measurements.

This experiments described in this chapter were performed at the AIST facility at Tsukuba, Japan [Mak08]. The beam was produced from a laser inverse-Compton backscattering with an external laser. Highly enriched targets of ^{142}Nd and ^{150}Nd were used. Neutron counting was done with a 4π composite neutron detector, consisting of rings of ^{3}He proportional counters embedded in a polyethylene block. The flux was measured with a large volume NaI scintillation detector. The beam profile was measured using a HPGe detector. In this section, the equipment used for the measurements at the AIST TERAS facility will be described in full,

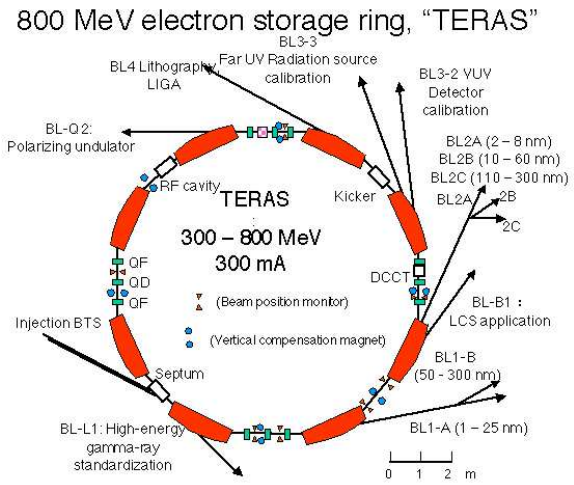

Figure 4.1: A schematic diagram of the TERAS storage ring. The laser inverse-Compton scatter (LCS) beam line is indicated by BL-B1 on the right side of the fi gure.

highlighting all of their unique advantages.

4.2 Experimental Setup

4.2.1 Facility

The laser inverse-Compton scatter (LCS) γ-ray source is located on the TERAS storage ring, used primarily as a synchrotron light source. It stores electrons with energy from 300 to 700 MeV, and beam currents up to 100 mA. The γ-ray beam is produced by inverse Compton backscattering. In the inverse kinematics, a high-energy electron collides head on with a low energy photon (visible to infra-red). The photon can then backscatter off of the relativistic electron, and is boosted to energies in the MeV range. For a more detailed discussion see [Bos08] and [Sch00b]. At TERAS an external Nd:YAG Q-switch laser with a frequency of 2 kHz is used [Shi05]. It produces a maximum 40 W of power at 1024 nm, or 10 W of power at 512 nm by tuning to the second harmonic of the laser. The beam is collimated by a 2 mm collimator before entering the experimental area [Uts03]. The general layout is shown in

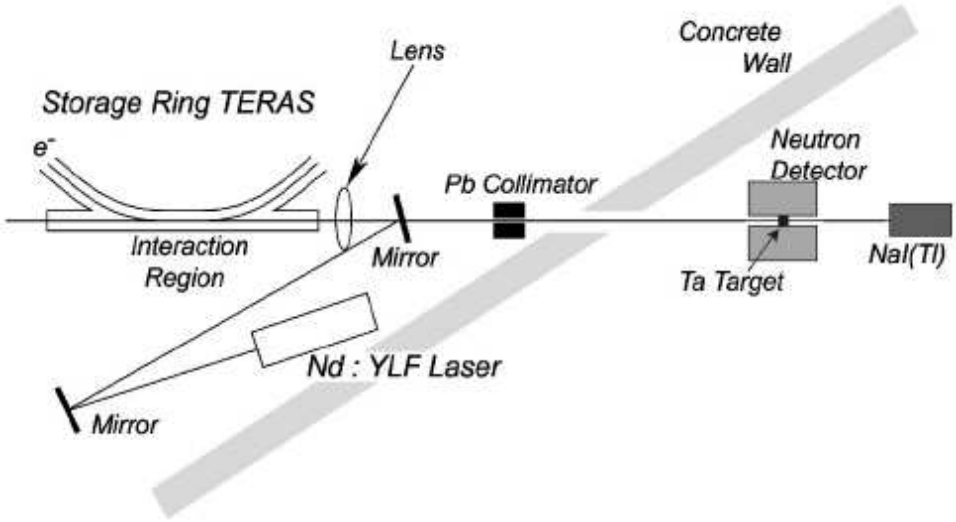

Figure 4.2: The layout of the LCS beam line.

Figs. 4.1 and 4.2.

4.2.2 Neutron Detector

A 4π neutron detector was used, which has a peak detection efficiency of 73% around 1 keV neutron energy. The detector consists of 20 ^{3}He proportional counters embedded in a polyethylene moderator in 3 concentric rings. There are 4 detectors in the first ring, and 8 detectors in each of the two outer rings (see Fig. 4.3). There is a hole running through the middle of the detector to insert the target, and for the beam to pass through. A high voltage of 1450 V is applied to the tubes. The ^{3}He proportional counters have a maximum efficiency at thermal neutron energies. The polyethylene thermalizes the neutrons to increase the total detection efficiency once they enter a ^{3}He detector. The distance a neutron can travel in the polyethylene is proportional to the energy of the neutron. The more energetic the neutrons are the more likely they are to be counted in the outer rings, and conversely less likely to be counted in the inner rings. The average energy of the photodisintegration neutrons can be determined by the ring ratio, the ratio of counts between the inner and outer rings.

During an experiment, the counts for all detectors in a single ring are summed together

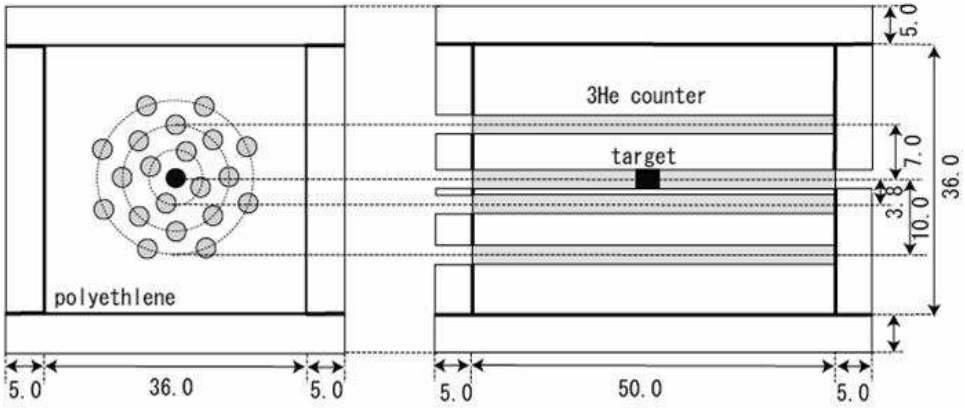

Figure 4.3: A schematic of the neutron detector used.

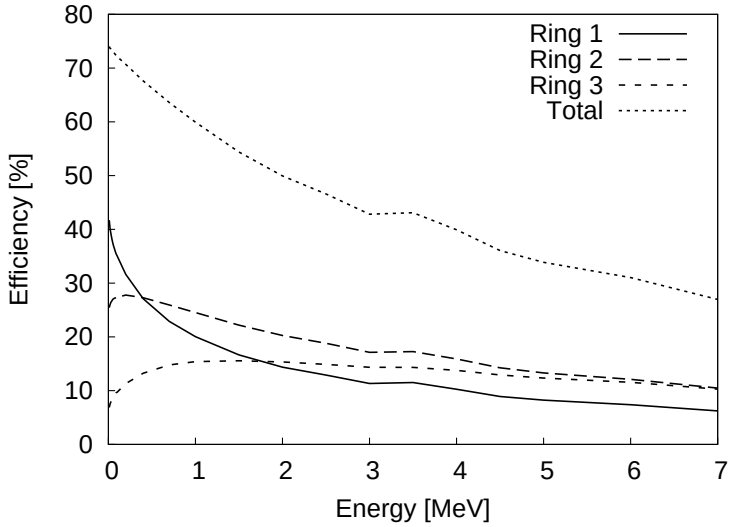

Figure 4.4: The neutron detector efficiency for each ring individually, and for all rings together.

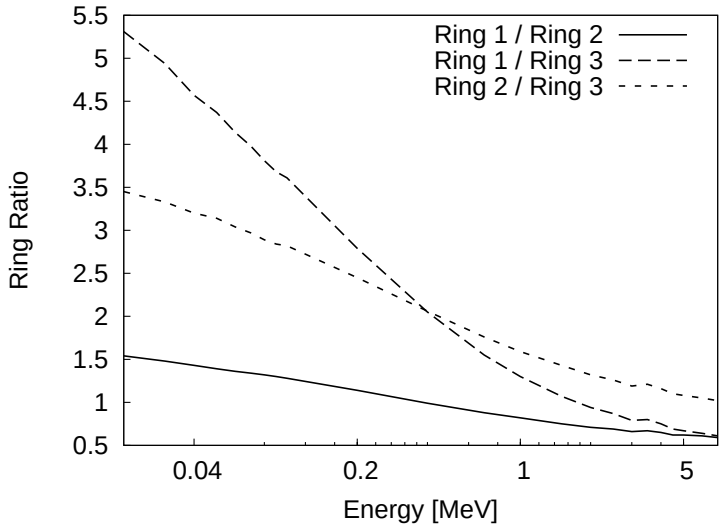

Figure 4.5: The ring ratios as a function of energy. Ring 1 is the inner most ring, and Ring 3 is the outer most ring. The x axis is log scale.

into one signal. To determine the room background counting rate, the laser is on for 80 ms, and then off for 20 ms. Turning off the laser turns off γ-ray production in the ring. The neutron counting rate for each ring is gated by this signal into two scalers, one for beam on, one for beam off. The background rate is then directly subtracted. The detector efficiency (Fig. 4.4) and ring ratio (Fig. 4.5) as a function of energy has been calculated previously using the Monte Carlo code EGS4 [Uts03]. The average neutron energy is obtained from the ring ratio. From the three rings, three different ratios are obtained. The spread in the three ratios gives an error of 1.6% for obtaining the average neutron energy. For the given average neutron energy, the detector efficiency is known, and is used to normalize the neutron counts. The efficiency simulation was verified using calibrated Am-Be and ^{252}Cf sources [Uts03].

A hardware threshold on each of the ^{3}He tubes is set to be above the γ-ray background from the beam. The tube has no energy resolution of the incident neutrons. The spectrum from the tube is characteristic of the $^{3}\mathrm{He}(n,p)^{3}\mathrm{H}$ reaction, which has a Q value or 764 keV. Looking at the spectrum in 4.6, a peak can be seen at high energy that corresponds to the total energy of the reaction been absorped in the tube. If the reaction happens near the outer edge of

the detector, one of the particles could potentially escape. The recoiling proton energy is 573 keV, and the triton energy 191 keV. The bump in the left hand side of the peak corresponds to the recoiling triton escaping the tube, and only the energy of the proton being absorped. The long low energy tail comes from the triton energy being fully absorbed, and only part of the proton energy absorbed. The spectrum stops at 191 keV. The γ-ray's scattering in a ^{3}He tube produce a very low pulse height (see Fig. 4.6), below that of the neutron peak. However, during the experiment the γ-ray background becomes much larger, and can extend to higher energy. Applying a threshold eliminates counts from γ-rays, but cuts some neutrons counts as well. To calibrate the efficiency of the threshold, a ^{252}Cf source is used. A spectrum is recorded from each tube, with both no threshold, and threshold applied. The ratio of the two rates is taken as the efficiency of the threshold. The average of the ratio was 83%. If the HV changes by ± 15 V this ratio will change linearly up to 5%. To take this into account, the spectra were taken at three different values of applied HV (1435 V, 1450 V, 1465 V) and the ratio found for each case (see Fig. 4.7). The position of the peak is directly related to the applied HV. The applied HV is monitored during the experiment by recording the spectrum of a ^{3}He tube.

4.2.3 Flux Measurements

Flux measurements at TERAS were made using a large single crystal NaI detector (12" diameter x 8" long) with 5 PMTs attached to the back (see Fig. 4.8). The γ-ray beam is directly incident on the center of the crystal, perpendicular to the detector face. The γ-ray beam occurs in pulses. In a single beam pulse multiple γ-rays can hit the detector. For the NaI crystal, the output signal is linearly proportional to the total energy deposited in the crystal. The total γ-ray flux can be obtained by determining the detector response to a single γ-ray, and then using this to normalize the flux for a spectrum when many γ-rays hit the detector simultaneously. The detector response is the average channel number in the energy spectrum.

For each energy, a spectrum is measured concurrently with the neutron counts to determine

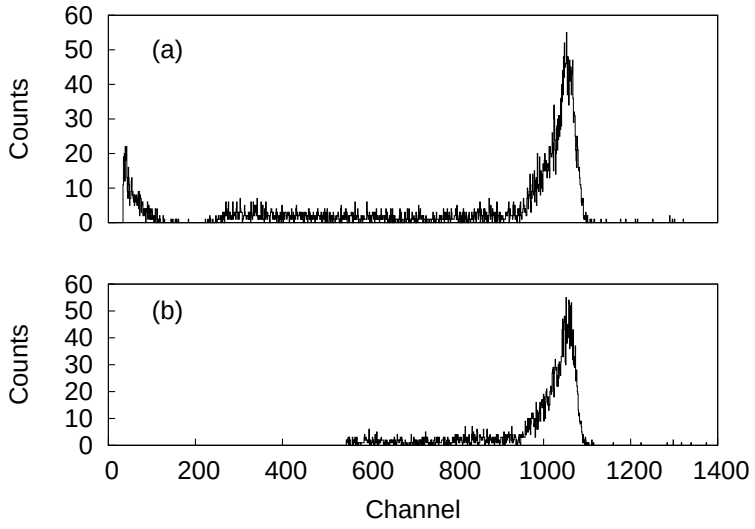

Figure 4.6: The ^{3}He calibration spectrum without (a), and with (b) a discriminator applied at channel 520. The background from γ-rays can be seen at low energies in (a), along with the tail of the neutron peak with a small separation between the two. During the experiment, the γ-ray background is much larger, making it necessary to place the discriminator in the region of the neutron peak. By applying the discriminator, the γ-ray background is elimimnated, but so are some of the counts from the neutron peak.

the total flux passing through the target. This spectrum is referred to as the "pileup" spectrum (Fig. 4.14). To determine the detector response for the beam profile, a low-flux, "singles" spectrum is measured before the data run (Fig. 4.13). The single photon peak is the largest, and is clearly separated from the two photon peak. For both of these cases, the background must be subtracted. A third spectrum, with the laser off, is used to measure the background that comes from the storage ring.

Detector Response

The large volume of the NaI detector simplifies determining the detector response and efficiency of the detector. Every γ-ray from the beam which enters the detector will interact in the detector, and leave most of its energy, as shown in Fig. 4.13. The total efficiency of the detector is approximately 100%. If multiple γ-rays from the same beam pulse enter the detector, they interact separately, each leaving an amount of energy characteristic to a single

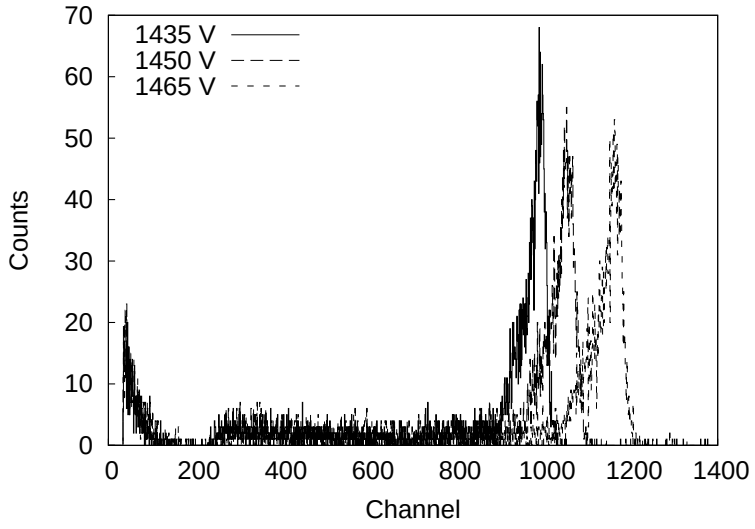

Figure 4.7: The uncut ^{3}He calibration spectra for the three different high voltages of 1435 V, 1450 V, and 1465 V are shown. The peak channel increases linearly with applied voltage.

γ-ray. The separate energy signals are summed linearly by the PMT's of the detector. There is a low pulse height cut off, but this has a negligible effect when determining the flux. This characteristic is used to extract the total flux from a spectrum which can contain counts which may come from many γ-rays hitting the detector simultaneously. At high fluxes, the average number of γ-rays hitting the detector can be as high as 15 (see Fig. 4.14). By deducing the response function of the detector to a single γ-ray, the flux can be determined from a pileup

Figure 4.8: The NaI detector and neutron detector from the back.

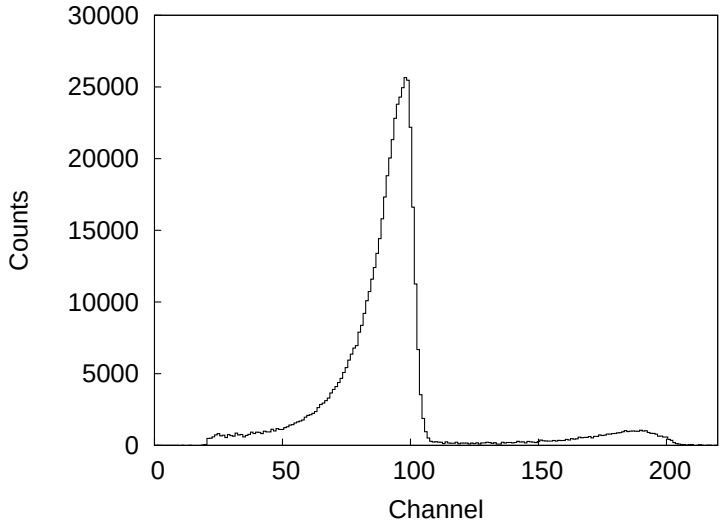

Figure 4.9: The singles spectrum after background subtraction for peak beam energy of $E_\gamma = 7.6$ MeV. The beam width is roughly 1.5 MeV.

spectrum. Once background subtraction has been done, the response function N^k, which is the average channel number for the spectrum, is given by

$$N^k = \frac{\sum x_i n_i}{\sum n_i} \tag{4.1}$$

where x_i is the channel number, and n_i is the number of counts in that channel, k stands in for either s for the "singles" spectrum, or p for the "pileup" spectrum. For the singles spectrum, the average channel number is found for only the first peak in order to get the average channel for a single γ-ray. The ratio of the average channel of the "pileup" spectrum to the average channel for a single γ-ray is the average number of γ-rays per event in the pileup spectrum. This ratio multiplied by the total number of counts in the "pileup" spectrum is the beam flux. This reduces to

$$N_\gamma = \frac{\sum n_i^s \sum x_i^p n_i^p}{\sum x_i^s n_i^s}. \tag{4.2}$$

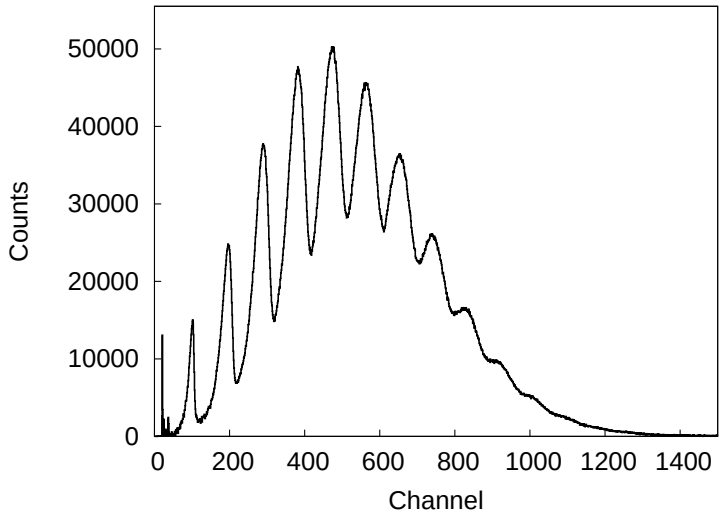

Figure 4.10: The pileup spectrum after background subtraction for for peak beam energy of E_γ = 7.6 MeV. The artifact at low energy is non-physical and comes from background subtraction.

Background Subtraction

There are two sources of background. One is the room background, which is generally constant with time, and concentrated at low energies, and easily subtracted. The room background contributes very little to the total background of the detector. The other source of background is bremsstrahlung caused by the high energy electrons in the storage ring. This includes γ-rays generated from collisions of electrons with the residual gas in the storage ring, and for electrons that fall out of orbit, collisions with the beam pipe. To measure the background from the ring, the laser is turned off, which stops γ-ray production, and the background is simply measured (see Fig. 4.15).

A complication arises during lasing. Background increases when the laser is turned on, and an additional low energy component appears. It increases the low energy background by about 30%. While the exact origin of the additional component is not known, it is thought to come from an increase in the number of electrons that leave orbit due to inverse-Compton scattering and collide with walls. When an electron and a laser photon Compton scatter, the electron loses enough energy that it can no longer be brought back up to storage ring energy

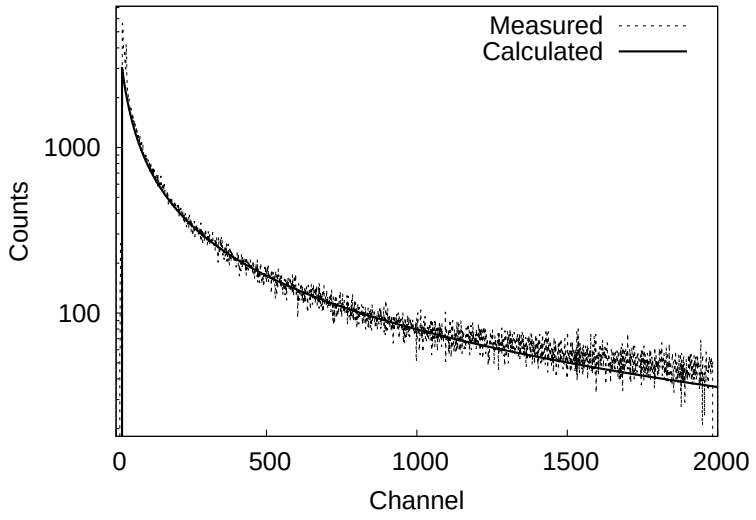

Figure 4.11: The background from the ring measured with the NaI detector. It is dominated by bremsstrahlung of the electrons on the residual gas in the storage ring. The Schiff formula was used for the calculated curve for comparison, and was normalized to the measured spectrum.

by the RF cavity.

Two procedures were adopted to subtract the background: a manual adjustment method and a method based on fitting the leading edge of the spectrum. For the manual method, the total scale of the measured background is manually adjusted to approximately account for the additional background, while maintaining a balance of not subtracting too much at high energies. The fitting approach was explored as a more scientific method of subtracting the additional background leaving less room for personal bias. It is based on the assumption that all of the additional background at low energy is below the peak energy of the beam. The peak shape is also assumed to have an exponential left tail. The measured background is first fit to the high energy part of the spectrum as in Fig. 4.15. Then an exponential is fitted to the left side of the first peak. This exponential is used as the shape of the peak below some cut off energy. These two steps will result in a spectrum that has the background removed, and can then be used to extract the flux. Both techniques were used for all runs. The fluxes obtained using the manual method and the fitting method for subtracting the additional background agreed to within 3%.

4.2.4 Beam Profile

Knowing the beam profile is important for three reasons. First, it allows one to determine the average energy of the beam. Second, it is needed to determine the ratio of counts above the reaction threshold energy to total counts. The beam has roughly 10% energy spread. At energies near S_n, a portion of the beam will be below S_n. The beam profile can be used to determine what percentage of the beam is below S_n so a correction can be made in the final cross section. And, third, the profile is used to calculate the moments when doing a Taylor expansion to correct for the width of the beam in determining the cross section (see Sec. 4.4.2). A HPGe detector is used to measure the beam profile. The detector is placed with the crystal perpendicular to the beam. The beam spot hits slightly above the center of the detector to maximize the amount of detector material the beam passes through. To avoid damaging the detector, the laser is operated in a low power mode to reduce the flux. The beam spectrum is measured for about 3 m. The measured spectrum represents the beam profile convoluted with the detector response. To extract the beam profile a Monte Carlo simulation must be made. This process is time consuming, and is done offline. The procedure used will be covered in Sec. 4.3.

4.2.5 Procedure

There are many steps involved for measurement of (γ, n) cross sections for every beam energy used. In a given experiment up to 30 different energies may be covered for all targets. At each energy several things must occur. First is alignment, then measuring the beam profile spectrum. The "singles" spectrum is measured, and then background runs are taken with both the NaI detector and the HPGe detector. Finally, the production run can be made at full γ-ray flux.

To maximize the γ-ray flux, the system must be aligned. First the laser is aligned with the electron orbit in the ring. When the energy of the electrons stored in the ring changes, the orbit

can change slightly. Once the laser has been aligned, the laser is turned off, and the neutron detector is aligned with the beam using the synchrotron light. The synchrotron light and the γ-ray beam are along the same axis.

Once everything is aligned, the beam profile spectrum using the HPGe detector must be measured. After this, the "singles" spectrum is measured using the NaI detector. For both of these cases, the laser is operated in low power mode, with an average of one γ-ray per beam pulse. In addition, a background run for the NaI is taken with the laser turned off. This is to measure the component of the background that comes from the ring. These two measurement are necessary at each beam energy.

4.3 Determining Beam Profile

Extracting the true beam profile from the measured spectrum requires using Monte Carlo simulations. A search for the correct beam profile can be done by doing a least squares search. The beam profile which best reproduces the experimental spectrum is used to extract such quantities as average beam energy and percentage of beam above S_n. During the (γ, n) experiments, several parameters of the geometry changed moderately from run to run, and had to be taken into account. Those were the distance from the collision point where γ-rays are generated to the detector, and the detector orientation with respect to the beam. If the geometry can change then the geometry parameters must be included in the least squares search. This section will cover the method of Markov chain Monte Carlo (MCMC) to perform a least squares fit search, obtaining both the optimal values of the parameters needed to determine the beam profile and their variance. The conditions of the search will be laid out, as well as what parameters in the simulation are used. The technique of MCMC will be introduced, including the optimal search algorithm and the nested sampling algorithm used to obtain the variances.

4.3.1 The Monte Carlo Simulation

A Monte Carlo code which simulates both the γ-ray production mechanism, and the detector geometry was previously written using EGS4 [Uts03]. Key parameters of the simulation are left as inputs to eliminate the necessity of modifying the Monte Carlo program to account for different situations. The following parameters are fixed for a given run:

- Collimator diameter. A 2 mm size was used for all simulations.
- Electron energy. This is changed to match the end point of the beam energy spectrum.
- Laser wavelength. Either 1024 or 512 nm.

Several other parameters are not known before hand, and are varied in order to find the best match to the experimental spectrum. They are:

- Distance between collimator and collision point. This parameter will vary for different energies while the beam orbit can change. This is usually about 550 cm.
- Effective length of Ge crystal. For different measurements the positioning of the detector can change relative to the beam. To account for this phenomenologically this parameter and the following one are varied.
- Effective radius of Ge crystal.
- Electron beam energy spread. This varies from run to run. Entered as a percentage.
- Electron beam size. The physical size of the electron beam in mm.

These parameters are ones that cannot be measured, and appropriate values can only be found by doing a parameter search. For each simulation, several minutes are required to run it. An efficient algorithm is essential to be able to find the best fit parameters in a reasonable time.

4.3.2 Markov Chain Monte Carlo

The use of MCMC has recently become a common tool in science for sampling the posterior probability distribution. The original algorithm was developed by Metropolis for finding the minimum energy of statistical ensembles in numerical simulations [Met53]. Since then, it has been developed beyond the initial algorithm and adopted into a rigorous field of Bayesian statistics which is used as widely as finding optimal cosmological parameters [Lid06] to modeling water catchment [Kuc98]. The technique is general and can be applied to problems in almost every field.

A Markov chain is a chain of data points that have the property that given an item in the chain, the probability of generating the next item is only governed by the state of the current item, and not by the history of the chain. The Metropolis algorithm is a method for generating a Markov chain that has an additional property. That the next state in the chain is randomly generated according to probability distribution dependent only on the present state, and is accepted based on its relative likelihood. The likelihood function contains the information on what is being maximized. The search algorithm is trying to find the states with the highest likelihood. For χ^2 fitting, the likelihood is $L = e^{-\chi^2/2}$. Maximizing the likelihood is the same as minimizing the χ^2. Because of this, this technique can be used for least squares fitting.

General Algorithm

The general algorithm is as follows.

1. Given a state, x_i with likelihood $L(x_i)$.

2. Randomly generate next state, x_{i+1} according to a probability distribution dependent only on current state, $Pr(x_i)$.

3. If $L(x_{i+1}) > L(x_i)$, accept the new state. Otherwise, accept the new state with probability $p = \frac{L(x_{i+1})}{L(x_i)}$. Sample a random number with a uniform distribution $\alpha \exists [0, 1)$. If $\alpha < p$, accept the new state. Otherwise, keep the current state.

4. Repeat N times.

Because each step can be accepted based on the relative likelihood of the two states, the algorithm will preferentially sample high density areas of the posterior distribution. The ability to conditionally accept states with a lower likelihood gives the algorithm the ability to escape local minima. The acceptance criterion used will properly construct the Markov chain so that the correct variance can be determined. Other acceptance criterions will give the same behavior of escaping local minima, sampling high density areas, and converging on the maximum, but will give the wrong variance for the parameters.

Generating the χ^2

The likelihood function is dependent on the χ^2. To calculate the χ^2 difference between the measured and simulated spectra, the hypothesis of homogeneity is used [Cra46, Gag06]. This is based on the idea that the histograms for both measured and simulated spectra are sampled from the same probability distribution. The χ^2 is given by

$$A = \sum a_i \,,\; B = \sum b_i$$

$$\chi^2 = \frac{\sum \frac{(a_i \cdot B - b_i \cdot A)^2}{a_i + b_i}}{A \cdot B}, \tag{4.3}$$

where a_i and b_i are the counts in channel i for the experimental spectrum and the spectrum generated by the simulation, respectively.

This will give the χ^2 independent of the number of samples in either the experimental or simulated spectrum. In practice, only the region above 3 MeV was used to determine the χ^2.

Random Walk

While generating a Markov chain with the correct properties depends on the acceptance criterion, the efficiency of the algorithm largely depends on the method used to choose the

next point. The next step is chosen randomly, but the properties of the probability distribution used will largely influence the convergence rate. Choosing an inappropriate walk algorithm can also give incorrect results. Three different walk algorithms were explored. One is based on a discrete walk, and the two others are modifications of a continuous distribution. The methods discussed vary only one parameter at a time.

For the discrete walk, only neighboring points on a grid are chosen. The direction to go is randomly chosen with equal probability. Randomness is ensured while the 4 other parameters will be varied in turn before the next step is determined for the initial parameter. By the time the first parameter is being varied again, the walk will likely be in a different region of the parameter space. The grid step size chosen will determine how fine grain the search is. Too large of a grid size, and the minima will likely be missed. Too small of a grid size, and the search will take too long to converge. The discrete walk can be modified to be continuous. The probability distribution is changed to a continuous distribution. For these simulations, a Gaussian distribution with zero mean was used. The variance was modified to optimize the convergance of the algorithm.

Procedure

Now that the general algorithm, and the method for generating the χ^2 value has been given, the specific algorithm used to find the best fit values can be discussed. Before the search is done, the known quantities are entered. The precise value for electron beam energy is not known before hand, but can be determined independent of any other parameters. The shape of the spectrum is affected by all parameters. However, the end point channel of the spectrum is determined solely by the electron beam energy. To find the correct parameters, random values are entered for the unknown quantities, and the approximate value of the electron beam energy which is recorded during the experiment is put in. A spectrum is simulated. If the end point is too high, or too low, it is adjusted accordingly. The end point energy is linearly dependent on the electron beam energy. Once the beam energy has been determined, the following algorithm

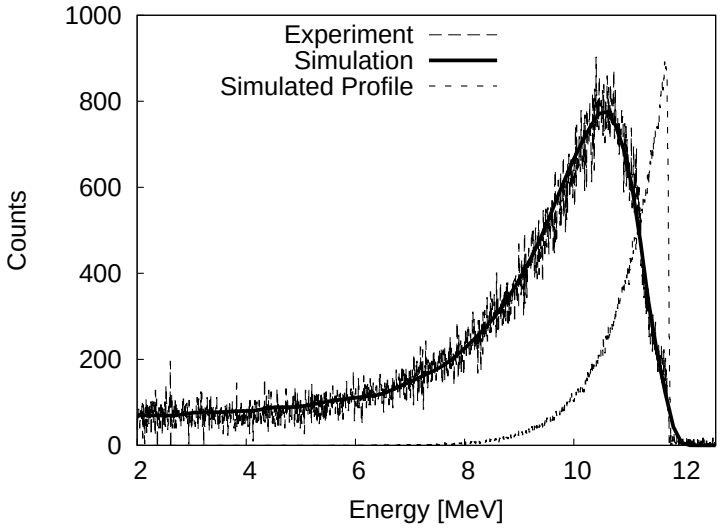

Figure 4.12: The MCMC method can find the parameter values that best match the experimental spectrum. Shown here is the experimental spectrum, with the results of simulation overlayed. The simulation was smoothed in order to distinguish between the two. Normally, it has the same statistical fluctuations as the experimental spectrum. Also shown is the resulting beam profile that produces the simulated spectrum.

is used to generate the Markov chain:

1. Randomly generate an initial set of parameters.
2. Simulate the spectrum for the initial parameters and obtain χ^2 difference.
3. Choose a parameter to be varied, x.
4. Obtain the next value using a random walk.
5. Simulate and obtain χ^2 difference.
6. Based on the likelihood, either accept or reject.
7. Repeat N times steps 3 through 6

4.3.3 Results

Using the technique outlined in this section, the beam profile was determined for over 50 runs. If the sole objective is to obtain the best fit values, then N, the number of iterations, can be relatively small. Test have been done with $N = 400$. The best fit values were found in an average of roughly 300 iterations (see Fig. 4.12). For a few cases, over 1000 iterations were needed. The beam profile is used to determine average energy, which is given by

$$E_{avg} = \frac{\sum_{i=i(S_n)} E_i n_i}{\sum_{i=i(S_n)} n_i}, \tag{4.4}$$

where S_n is the neutron separation energy, E_i and n_i is the energy and counts of the i^{th} channel, respectively. The sum is from the neutron separation energy to the end of the energy profile. The q factor, the ratio of beam flux above the neutron separation energy to the total flux, is determined by

$$q = \frac{\sum_{i=i(S_n)} n_i}{\sum_{i=0} n_i}. \tag{4.5}$$

The profile is also used in determining various moments for the Taylor expansion used in data reduction (see Sec. 4.4.2).

For determining the variance, a large sampling is needed to adequately probe the configuration space. Tests were done using an algorithm known as nested sampling [Ski06]. Numerical results were inconclusive, but qualitative understanding of the dependency of E_{avg} and q on the beam profile was obtained. As derived quantities of the beam profile, they turn out to be relatively insenstive to changes in the beam profile. Small changes to the beam profile which significantly altered the χ^2 only modestly changed E_{avg} and q. In runs where the end point energy of the beam profile is very close to the neutron separation energy, the values of E_{avg} and q changed significantly in select cases with a change in the beam profile. More work is needed to explore the feasibility of applying it to determining the variance of Monte Carlo simulations, and in obtaining quantitative rather than just qualitative results.

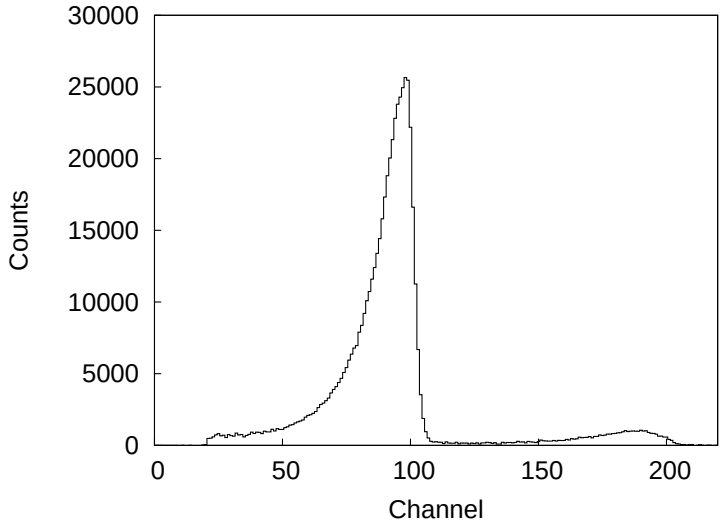

Figure 4.13: The singles spectrum after background subtraction for peak beam energy of E_γ = 7.6 MeV. The beam width is roughly 1.5 MeV.

4.4 Data Analysis

The data analysis for the (γ, n) experiments consists of obtaining the flux, correcting the neutron counts, determining the beam profile, and then doing a Taylor expansion to account for the beam width. The determination of the beam profile entailed developing a Markov-chain Monte Carlo (MCMC) algorithm to obtain the correct profile, as described in Sec. 4.3. The calibration of the neutron detector was already discussed in Sec. 4.2.2. All other aspects of the data analysis will be discussed in this section.

Detector Response

The large volume of the NaI detector simplifies determining the detector response and efficiency of the detector. Every γ-ray from the beam which enters the detector will interact in the detector, and leave most of its energy, as shown in Fig. 4.13. The total efficiency of the detector is approximately 100%. If multiple γ-rays from the same beam pulse enter the detector, they interact separately, each leaving an amount of energy characteristic to a single γ-ray. The separate energy signals are summed linearly by the PMT's of the detector. There

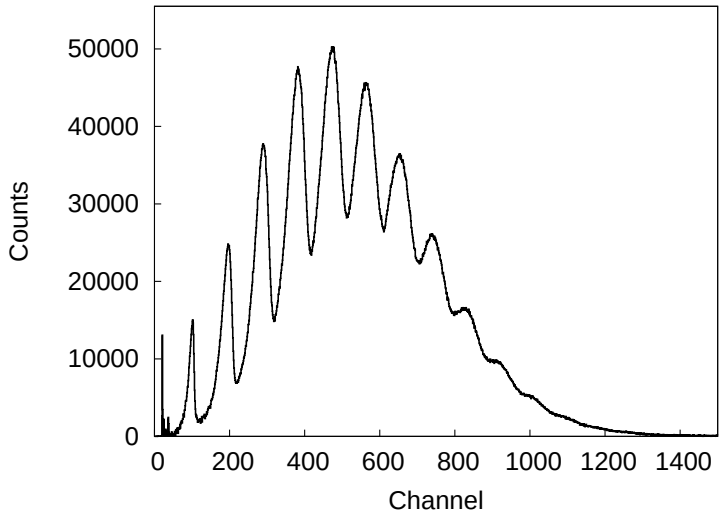

Figure 4.14: The pileup spectrum after background subtraction for for peak beam energy of E_γ = 7.6 MeV. The artifact at low energy is non-physical and comes from background subtraction.

is a low pulse height cut off, but this has a negligible effect when determining the flux. This characteristic is used to extract the total flux from a spectrum which can contain counts which may come from many γ-rays hitting the detector simultaneously. At high fluxes, the average number of γ-rays hitting the detector can be as high as 15 (see Fig. 4.14). By deducing the response function of the detector to a single γ-ray, the flux can be determined from a pileup spectrum. Once background subtraction has been done, the response function N^k, which is the average channel number for the spectrum, is given by

$$N^k = \frac{\sum x_i n_i}{\sum n_i} \tag{4.6}$$

where x_i is the channel number, and n_i is the number of counts in that channel, k stands in for either s for the "singles" spectrum, or p for the "pileup" spectrum. For the singles spectrum, the average channel number is found for only the first peak in order to get the average channel for a single γ-ray. The ratio of the average channel of the "pileup" spectrum to the average channel for a single γ-ray is the average number of γ-rays per event in the pileup spectrum.

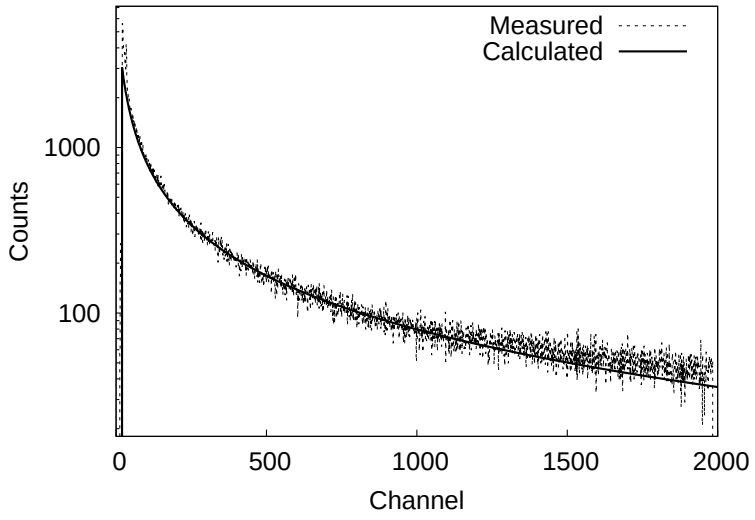

Figure 4.15: The background from the ring measured with the NaI detector. It is dominated by bremsstrahlung of the electrons on the residual gas in the storage ring. The Schiff formula was used for the calculated curve for comparison, and was normalized to the measured spectrum.

This ratio multiplied by the total number of counts in the "pileup" spectrum is the beam flux. This reduces to

$$N_\gamma = \frac{\sum n_i^s \sum x_i^p n_i^p}{\sum x_i^s n_i^s}. \tag{4.7}$$

Background Subtraction

There are two sources of background. One is the room background, which is generally constant with time, and concentrated at low energies, and easily subtracted. The room background contributes very little to the total background of the detector. The other source of background is bremsstrahlung caused by the high energy electrons in the storage ring. This includes γ-rays generated from collisions of electrons with the residual gas in the storage ring, and for electrons that fall out of orbit, collisions with the beam pipe. To measure the background from the ring, the laser is turned off, which stops γ-ray production, and the background is simply measured (see Fig. 4.15).

A complication arises during lasing. Background increases when the laser is turned on, and an additional low energy component appears. It increases the low energy background by

about 30%. While the exact origin of the additional component is not known, it is thought to come from an increase in the number of electrons that leave orbit due to inverse-Compton scattering and collide with walls. When an electron and a laser photon Compton scatter, the electron loses enough energy that it can no longer be brought back up to storage ring energy by the RF cavity.

Two procedures were adopted to subtract the background: a manual adjustment method and a method based on fitting the leading edge of the spectrum. For the manual method, the total scale of the measured background is manually adjusted to approximately account for the additional background, while maintaining a balance of not subtracting too much at high energies. The fitting approach was explored as a more scientific method of subtracting the additional background leaving less room for personal bias. It is based on the assumption that all of the additional background at low energy is below the peak energy of the beam. The peak shape is also assumed to have an exponential left tail. The measured background is first fit to the high energy part of the spectrum as in Fig. 4.15. Then an exponential is fitted to the left side of the first peak. This exponential is used as the shape of the peak below some cut off energy. These two steps will result in a spectrum that has the background removed, and can then be used to extract the flux. Both techniques were used for all runs. The fluxes obtained using the manual method and the fitting method for subtracting the additional background agreed to within 3%.

4.4.1 Attenuation Coefficients

The measured γ-ray flux is that which is directly incident on the NaI detector. The target attenuates the beam to an appreciable degree, so a correction must be made in order to account for this effect. The attenuation coefficient is relatively straight forward to obtain. The fraction of absorbed γ-rays, f, is given by $f = e^{-\mu\rho t}$ where μ is is the linearly attenuation coefficient, given in cm^2/g, ρ is the density of the target, and t is the thickness of the target. The linear attenuation coefficient, μ, is obtained from the NIST XCOM database [Ber]. The

linear attenuation formula must be modified to account for not just the attenuation in the flux, but also that the measured count rate depends on the intensity of the beam at each point in the target. The attenuation coefficient must be integrated over the length of the the target. The value must be multiplied by the attenuation, $e^{\mu\rho t}$, of the whole target to get the original flux from the measured flux. Finally this gives

$$f = e^{\mu\rho t}\left(\frac{1 - e^{-\mu\rho t}}{\mu\rho t}\right). \tag{4.8}$$

4.4.2 Cross Section

The cross section for (γ, n) is given by

$$\sigma_{(\gamma,n)} = \frac{N_n}{N_t N_\gamma f \epsilon_n q} \tag{4.9}$$

where N_n is the number of neutrons counted, N_t the areal density of the target, $N_\gamma(E_\gamma)$ is the flux as a function of energy, ϵ_n is the efficiency of the neutron detector, f is the attenuation coefficient for the target, and q is the percentage of the beam above the neutron separation energy, as determined from the beam profile. During an experiment these quantities are measured separately with two different detectors, the NaI for total flux (Sec. 4.4), and the HPGe detector (Sec. 4.3).

Uncertainties

The statistical uncertainty for the neutron counts, N_n, is on the order of 1% for all energies and targets measured. A second source of statistical uncertainty arises in determining the neutron energy from the ring ratios. There are three rings, giving three ratios, with the standard error of the neutron energy being on average 1.6%. This translates to a 1.6% uncertainty for ϵ_n. The largest source of systematic uncertainty comes from the background subtraction method used for determining the beam flux. By comparing the two methods used, it was

determined that the systematic uncertainty is 3%. The uncertainty associated with the beam profile remains unassessed, largely due to the difficulty in determining the variance of Monte Carlo simulations (see Sec. 4.3.3).

Taylor Expansion

A correction needs to be made for the width of the beam [Uts06]. The beam has an energy width of about 10%, with significant left tailing. The measured cross section is an average of the photodisintegration cross section weighted by the beam profile. To correct for this weighting, a data reduction algorithm must be used. The algorithm used is an iterative process involving a Taylor expansion of the beam profile convoluted with the cross section. The method employed was taken directly from [Uts06]. The cross section formula, Eq. 4.9, is modified as

$$\int n_\gamma(E_\gamma)\sigma_{(\gamma,n)}(E_\gamma)dE_\gamma = \frac{N_n}{N_t\ f\ \epsilon_n} \tag{4.10}$$

where $n_\gamma(E_\gamma)$ is the flux per keV. The quantity g has been neglected because it is now contained directly in the integral of n_γ. To solve for the equation, a Taylor expansion is done on $\sigma_{(\gamma,n)}(E_\gamma)$, giving

$$\sigma(E_{av}) + s_2(E_{av}) + s_3(E_a v) + \cdots = \frac{N_n}{N_t N_\gamma f \epsilon_n\ g}, \tag{4.11}$$

where

$$s_i(E_{av}) = \frac{1}{2}\frac{d^i\sigma(E_{av})}{dE}\int n_\gamma(E_\gamma - E_{av})^i dE_\gamma/(N_\gamma\ g). \tag{4.12}$$

s_1, the moment for the average energy is not included because it reduces to zero since the expansion is taken about the average energy. To obtain the cross section an iterative process is used. The cross section is computed with no corrections for all points. The plot is then fit using the following function

$$\sigma(E_\gamma) = \sigma_0\left(\frac{E_\gamma - S_n}{S_n}\right)^p + A\left(E_\gamma - B\right)^3 \tag{4.13}$$

giving four fit parameters, γ_0, p, A, and B. This accounts for the behavior near threshold, and the rise of the cross section at higher energies. The moments, s_i, are then computed, and $\sigma(E_{av})$ is computed using the moments. The process is done once again using the new values of $\sigma(E_{av})$, being repeated until the process converges $\sigma(E_{av})$ which normally takes 4 to 5 steps. In practice only moments s_2 and s_3 are used, because the fitted function includes only a third order polynomial. This process introduces about a 3.5% correction at low energies, and upto 10% at the highest energies.

4.5 Results

The cross sections measured for ^{142}Nd agrees with the previously measured values[Car71], but has improved the precision, especially close to threshold (see Table 4.1). The measurements here represent the first direct cross section measurements below 9.5 MeV for ^{150}Nd (see Table 4.2). These uncertainties for the cross sections include all statistical uncertainties, but does not include the estimated systematic uncertainty from the flux determination method. These results will be discussed in the context of theoretical predictions in Ch. 6.

Table 4.1: Measured (γ, n) cross sections for ^{142}Nd. Only statistical uncertainties are included.

Energy [MeV]	$\sigma_{(\gamma,n)}$ [mb]	$\Delta\sigma$ [mb]
9.86	22.3	1.5
9.9	36.1	0.9
9.95	32.2	1.0
10.12	37.8	1.1
10.28	42.6	1.0
10.46	46.5	1.9
10.74	54.9	5.0
11.09	58.5	1.9
11.4	70.1	1.9
11.73	85.5	2.0
12.16	100.1	2.8
12.3	116.2	4.5
12.76	152.3	5.8
13	178.6	3.2
13.26	198.7	4.8

Table 4.2: Measured (γ, n) cross sections for ^{150}Nd. Only statistical uncertainties are included.

Energy [MeV]	$\sigma_{(\gamma,n)}$ [mb]	$\Delta\sigma$ [mb]
7.56	11.35	0.39
7.57	13.75	0.54
7.77	20.51	0.60
7.94	18.02	0.32
8.16	23.14	0.33
8.37	24.49	0.39
8.68	30.04	0.52
8.75	30.42	0.31
8.78	32.14	0.54
8.93	30.23	0.46
8.94	34.42	0.58
9.01	37.14	0.86
9.24	42.20	2.07
9.43	47.87	0.95
9.71	54.12	2.59
9.92	58.31	1.42
10.33	79.75	5.91
10.91	110.81	2.40
11.26	135.90	3.38

Chapter 5

Experiments - Nuclear Resonance Flourescence

5.1 Introduction

To include thermal excitation into the realistic reaction rate calculations for the *p*-process requires inclusion of thermal excitations, and a knowledge of the γSF below the neutron separation energy, S_n. In addition, pygmy resonances below the neutron separation energy could potentially enhance the reaction rate on excited states. Measurements of the γSF below S_n are needed in order to constrain the low energy tail of the GDR, and determine the properties of pygmy resonances if there are any. NRF measurements have traditionally been interested only in measuring the properties of single states, and have overlooked the large contribution to the γSF from the many weak states that cannot be individually resolved. Recently, there has been other experimental efforts to extract the total γSF from NRF measurements [Rus06a]. Several approaches are possible for extracting the total γSF from NRF measurements [Bos08, Rus06b]. The technique presented here relies on the monoenergetic nature of the beam produced at HIγS. Nuclear resonance fluorescence measurements were performed on both ^{142}Nd and ^{150}Nd at the HIγS facility. While previous NRF measurements have succesfully been done at HIγS [Pie02, Ton05, Li06], this is the first time that the total photoabsorption

cross section has been obtained from the data in a model independent way.

Two important pieces of information are expected to come from the experiment: the total photoabsorption cross section, and the partial decay widths for specific states excited in the NRF process. The total photoabsorption cross section cannot be directly obtained, but it can be reconstructed from measured partial cross sections in the present work. Two types of partial cross sections were measured. The partial cross section for the decay from the initially excited state, and the partial cross section for depopulation of lower excited states fed by branchings from the initially excited states. For ^{142}Nd the elastic scattering cross section was measured as well as the partial cross sections for the decay of several low-lying states (see Fig. 5.1). In ^{150}Nd, the decay from the initially excited states to four low-lying states were observed (see Fig. 5.2). The partial cross sections of the low lying excited states cannot be used to directly infer the branchings from the initially excited state while they may also be fed by multi-step transitions. However, the HIγS mono-energetic γ-ray beam allows them to be unambiguously identified within the excitation and decay of a small energy window. By summing them with the elastic cross section, the total photoabsorption cross section can be obtained, as was the case for ^{142}Nd. If not all partial cross sections can be obtained, as it is for ^{150}Nd, the total photoabsorption cross section can be obtained by constraining statistical model calculations of the measured partial cross sections.

In the present experiment, measurements were made on ^{142}Nd at 19 energies from 3.4 MeV to 9.7 MeV. For ^{150}Nd, 5 measurements were made in .4 MeV steps from 5.6 MeV to 7.2 MeV. Highly enriched targets were used for both ^{142,150}Nd. The mass for the ^{142}Nd target is 28.79 g, and for ^{150}Nd, 0.96 g. Both quantities are for the masses of the specific isotope. The data for ^{142}Nd from 3.4 MeV to 5.4 MeV were taken in December, 2007. The remaining energies for ^{142}Nd and all energies for ^{150}Nd were taken in January, 2008. Calibration measurements on ^{11}B were also taken at energies of 4.44, 5.09, and 8.91 MeV. This chapter will outline the experimental techniques used, and the analysis procedure chosen to extract the total γSF. The procedure for obtaining the widths of individual states will also be discussed.

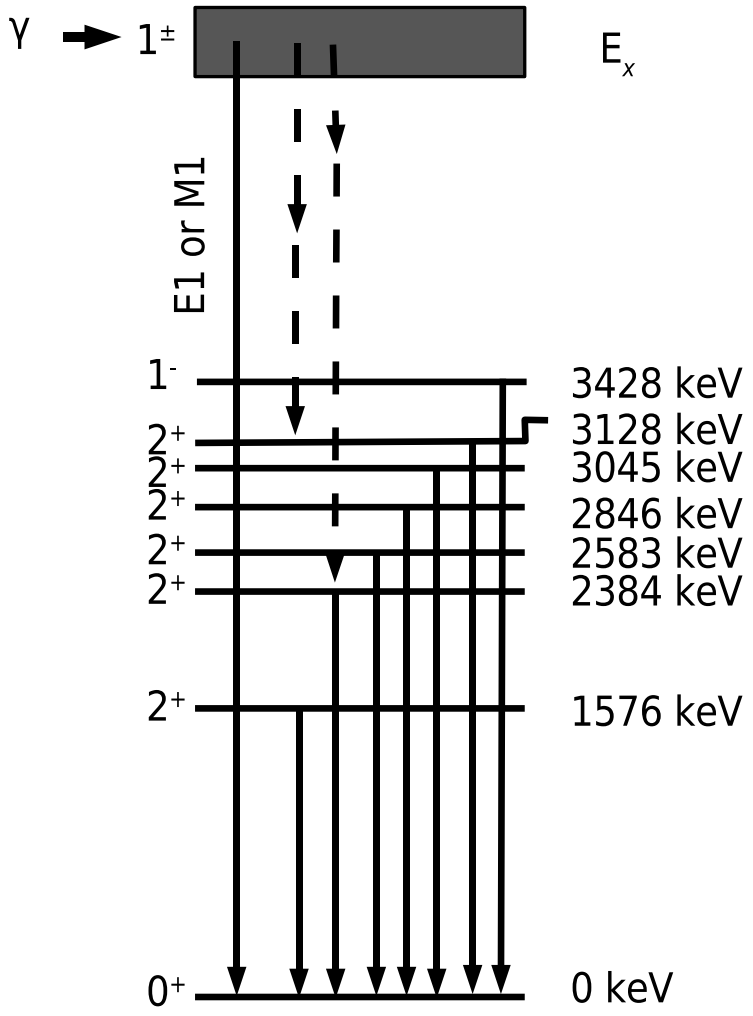

Figure 5.1: The level scheme for ^{142}Nd. The solid lines are transitions for which partial cross sections were determined. The dashed lines represent possible ways the low-lying states can be populated. There are many ways for the nucleus to decay to the low-lying states.

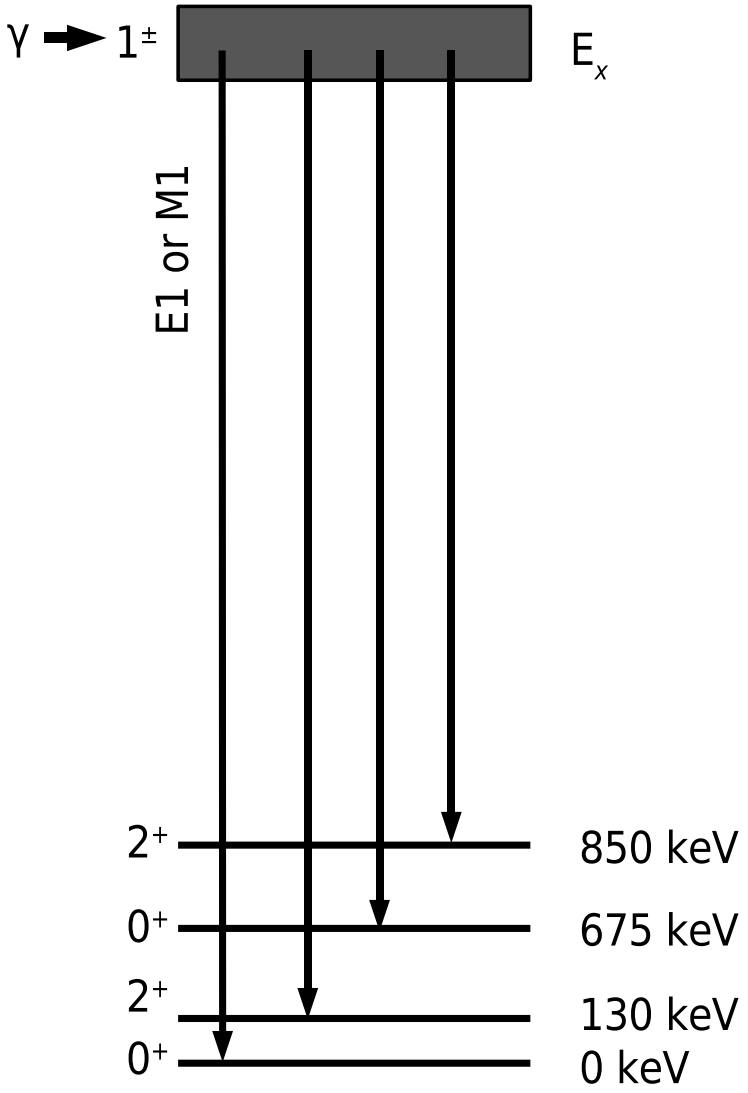

Figure 5.2: The de-excitation scheme for ^{150}Nd. The solid lines are transitions for which partial cross sections were determined. The de-population of low-lying states was not observed as the transition energies were below the threshold set on the detectors.

5.2 Experimental Technique

The γ-ray beam at the HIγS facility was used for the NRF measurements. Four HPGe Clover detectors were used in a polarimeter configuration as the detector array. A HPGe detector mounted on a curved track was used to both measure the beam profile and to monitor the flux. Each component will be described with the focus on the Clover detector array, and the 0° detector.

5.2.1 HIγS Facility

The Duke FEL provides a pulsed, mono-energetic γ-ray beam ($\Delta E/E \approx 3\%$), which can be 100% linearly polarized [Lit97]. The energy is tunable from 1.5 MeV to 60 MeV. The flux of the beam is energy dependent ranging from 10^4 to 10^7 γ/s. The beam occurs in pulses, corresponding to when the electron bunch passes through the wigglers. The beam has a duty cycle of 172 ns off, and 2 ns on. When the beam passes through a beam pick-off, a pulse is generated which is sent to the data acquisition electronics. This pulse is referred to as the RF signal. Using this RF signal, a time-of-flight measurement can be made.

The operation of an FEL as a γ-ray source requires three elements: an electron source, wigglers, and an optical cavity. The Duke FEL uses a 270 MeV linac as the electron source. The facility was recently upgraded to add a booster ring with an RF cavity. The electrons are injected into the booster ring, and, using the RF cavity, are ramped up to the desired energy, up to 1.5 GeV, and then injected into the storage ring. Using the booster, the bunches in the storage ring are topped off continuously, providing an uninterrupted beam of almost constant intensity. Once the electrons are in the storage ring, lasing is produced by the electrons going through the wiggler (see Fig. 5.3). The wiggler consists of a series of opposing magnets with the north pole facing the south pole, and the beam going through the middle. The poles of the magnets alternate (N-S then S-N), with the net effect of the electron “wiggling” back and forth in the changing magnetic field. This acceleration of the relativistic electrons causes them to

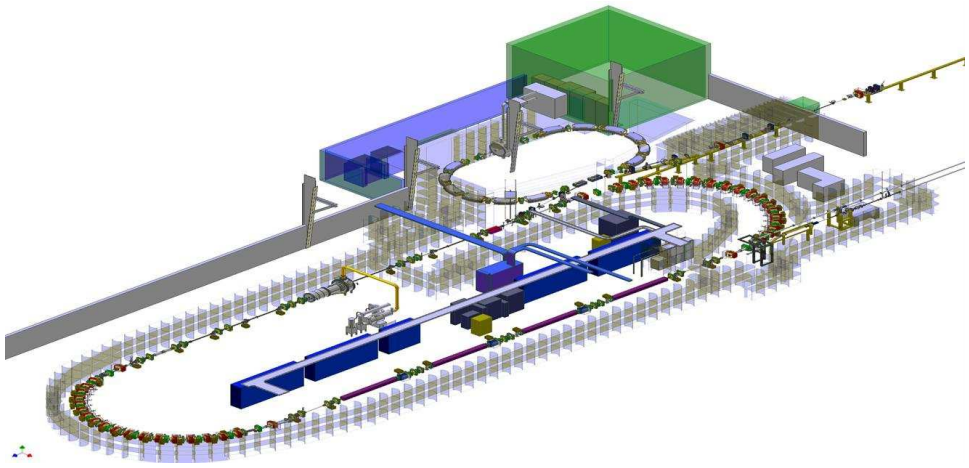

Figure 5.3: The FEL at Duke uses an OK-4 wiggler to produce lasing. γ production is done by operating in two bunch mode, each bunch is 180^o out of phase with each other. The length of the optical cavity is one-half the circumference of the storage ring. This causes the emitted light from one bunch to Compton back-scatter off of the second bunch, boosting it into MeV range energies. The optical cavity is in the bottom straight leg of the storage ring.

emit low-energy photons, whose energy can be selected by varying the electron energy, and the parameters of the wiggler. To produce coherent light, the wiggler is placed in the middle of an optical cavity half the length of the storage ring, so that when the electrons pass through the wigglers each time, the light previously produced will constructively interfere, inducing coherent emission of photons. Another property of FEL's is that the emitted light will be 100% polarized in the direction perpendicular to the direction of the magnetic field, which, in the case of the Duke FEL, results in horizontal polarization.

FEL produces light in the wavelength region from infrared to ultra-violet. To produce γ-rays, a second step of Compton back-scattering is needed. By having a second electron bunch 180° out of phase with the first electron bunch, the photons emitted by the second bunch will then collide head on with the electrons in the second bunch as it passes through the wigglers, and will then Compton back-scatter off of them boosting the low-energy photon up into the MeV range. The energy of the scattered photons vary as a function of the angle from the maximum energy determined by the energy of the initial photon and electron which occurs at a scattering angle of 180°, decreasing continuously as the angle decreases [Sch00b].

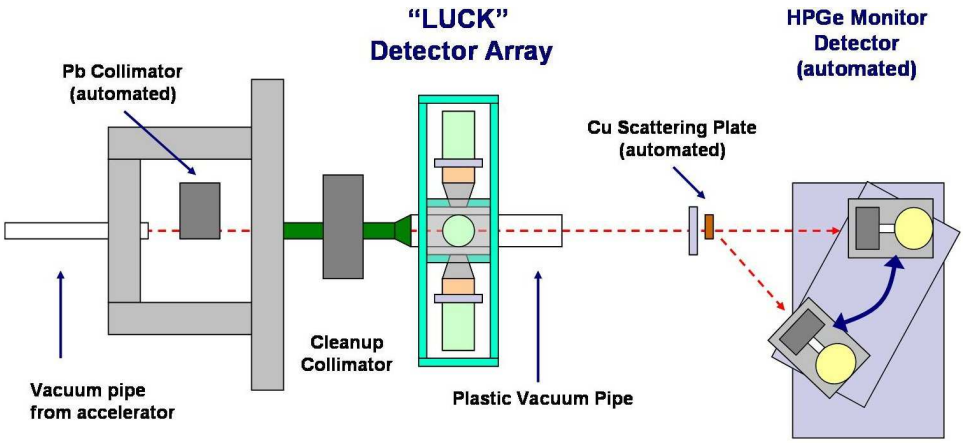

Figure 5.4: A diagram of the beam line including the collimator hut and vault. The γ-ray beam goes from left to right. Not pictured is a 60% HPGe polarimeter immediately following LUCK, which was not used in the present experiment, and the scintillator paddle which is in the collimator hut, following the collimator.

5.2.2 Beam Line

The experimental setup used at HIγS consists of the collimator located in the collimator hut, the LUCK detector array, a plastic vacuum pipe, and the monitor detector with accompanying Cu plate, all of which are in the vault (see Fig. 5.4). The scintillator paddle is a secondary system used to monitor the flux. The beam line was aligned to a laser that ran down the beam line in the vault area. A plastic vacuum pipe was added to eliminate background that's generated from Compton scattering of the beam on air. It runs from the point when the beam enters the vault to about 2 m after the target.

Beam Collimation

When the beam enters the collimator hut, it has an angular spread and needs to be collimated. Since the energy of the Compton back-scattered photons is dependent on the angle of collision, according to the Klein-Nishina formula, the angular spread corresponds to a spread in energy. By collimating the beam, the energy spread is reduced, but at the same time the flux decreases. When choosing a collimator, a trade off in energy resolution and flux must be

made. It is sometimes necessary to have several different collimator sizes of collimator available during an experiment. A system was built to automate the selection of the collimator size. The collimator block has six holes in it with different diameters (.50, 1.27, 1.90, 2.54, 3.18, and 3.81 cm) in a block of Pb that is 30.5 cm x 30.5 cm x 20.3 cm. The block is mounted on a platform on rails, and a linear actuator is used to move the platform. It is remotely controlled via a LabVIEW interface so that the collimator can be changed without having to interrupt the beam to access the collimator hut. For the present experiment, a collimator of 1.27 cm diameter was chosen for ^{142}Nd and of 1.90 cm for ^{150}Nd. Even with collimation there remains a small angular spread in the beam, which results in a slight low-energy tail in the beam spectrum. For the collimator sizes chosen it is hardly noticeable, but for the larger sizes it can become a significant factor.

Aligning the Beam

The γ-ray beam at HIγS needs to be aligned to the beam line in the vault. The operators can change the position of the γ-ray beam by changing the orbit of the electrons in the storage ring. To align the beam several beam energy spectra were taken with the operator changing the position of the beam. The beam position that minimized the width was taken as the position that best aligned the beam. After the experiment was completed, scientists at the FEL developed a beam imager that can directly image the beam. The result can be seen clearly in Fig. 5.5, showing how a beam can be misaligned, and corrected to be aligned with the vault beam line axis [Sun08].

5.2.3 LUCK - Clover HPGe detector array

The LUCK detector array was constructed for the present experiment using four HPGe Clover detectors as seen in Fig. 5.6. A polarimeter consists of four detectors placed perpendicular to the beam – two horizontal, and two vertical, and is the optimal design for observing the parity of $J = 1$ states in NRF experiments. However, LUCK is not only a polarimeter.

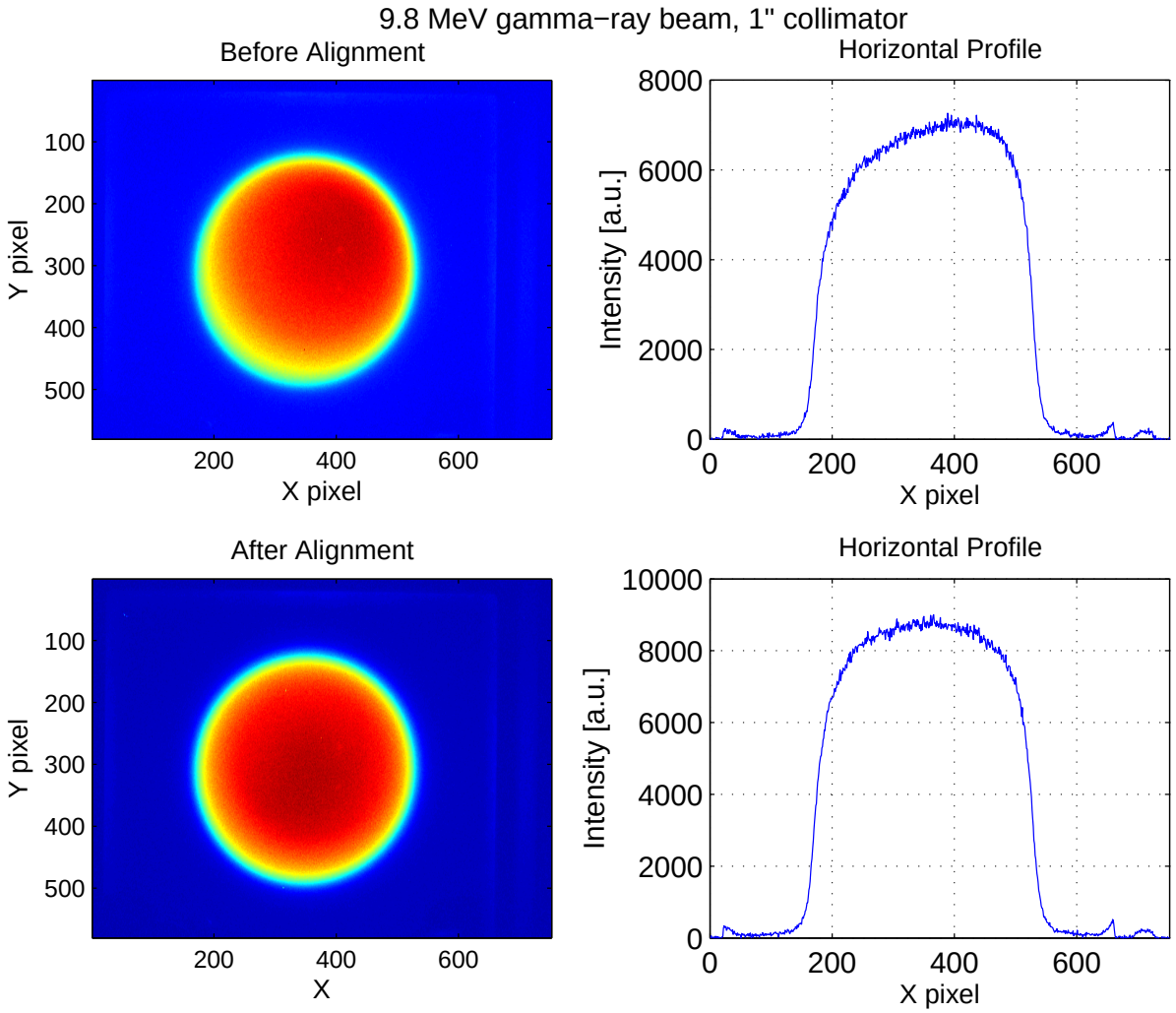

Figure 5.5: A spatial image of the beam showing both an unaligned, and an aligned beam. The sharp circular shape is from the collimator. The center of the collimator is aligned to the beam line axis. Used with permission from [Sun08]

.

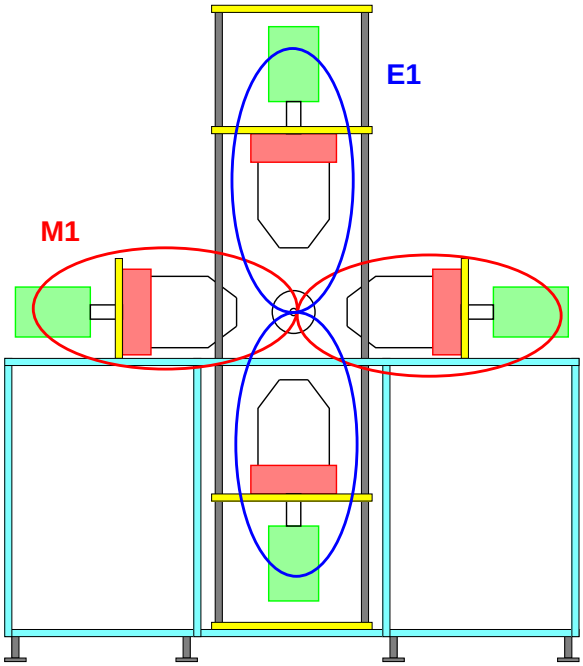

Figure 5.6: A diagram of the LUCK detector array. The detectors are placed to be able to determine the parity of the γSF.

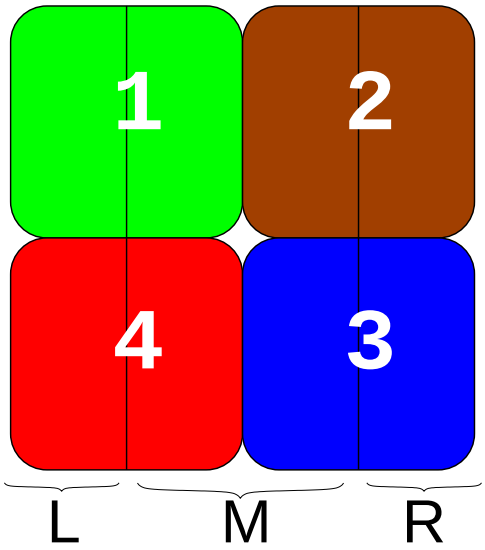

Figure 5.7: The HPGe Clover detector has eight fold segmentation. There are four physically separate crystals, each with its own energy signal, and three position signals, left (L), middle (M), and right (R).

The use of the high efficiency Clover detectors make it ideal for (γ, γ') partial cross section measurements. The Clovers were numbered 1 through 4, starting with right detector (looking down the beam line), going counter-clockwise. The Clover detectors are composite HPGe detectors with eight fold segmentation. It has four separate rectangular crystals, each providing a γ-ray energy signal, and then three position signals consisting of left, middle, and right, giving effectively eight separate segments (see Fig. 5.7). For this experiment, the position signals were not used, only the energy signal from each crystal. The physical segmentation of the detector into separate crystals is to create a large volume detector while also getting around the additional problems introduced by a large volume crystal, particularly large count rate, and degradation from radiation damage. To obtain the full efficiency of the detector, the separate energy signals from each crystal are added back together. Having separate crystals can also be used to reduce background by allowing separate TOF cuts on each crystal. Only signals from crystals whose peaks lie within the TOF gate will be added back together. The Clover detectors also have an active BGO veto shield for Compton suppression. This feature was only used to improve the signal to background ratio for full energy peaks that happened to lie below the beam energy, i.e. branchings to excited states and their decay. During the experiment, Pb attenuators were placed in front of the four Clover detectors to reduce the count rate from low-energy γ-rays, especially annihilation γ-rays from positrons from pair creation in the target. For runs with ^{142}Nd below 5.6 MeV a thickness of .32 cm was used, between 5.6 and 8.7 MeV .64 cm was used, and above 8.7 MeV .96 cm was used. For ^{150}Nd, all runs used .64 cm of Pb.

Detector Efficiency

The efficiency of the detectors was determined using both ^{56}Co and ^{60}Co radioactive sources. An efficiency curve for the Clovers with add back mode was calculated using MCNP for single crystal summing mode [Hut08a, Hut07]. The calculated efficiency curve, normalized to the data, matches the measured efficiency over a wide range of energies from 1.4 to 3.5

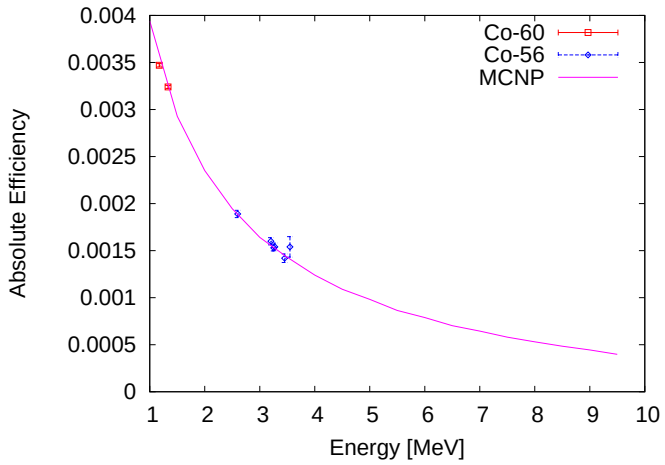

Figure 5.8: The absolute efficiency for the single crystals summed together measured with ^{56,60}Co for Clover 1. The low energy ^{56}Co points have been excluded because of threshold effects which gives a lower effective efficiency. The ^{60}Co points were acquired by lowering the detector threshold to 250 keV. The solid line is the calculated efficiency from MCNP normalized to the data.

MeV. In order to prevent the annihilation γ-rays from triggering the electronics, the threshold was set at 650 keV for two detectors and 900 keV for the other two. However, for the CFD (constant fraction discriminator) used for the Clover detectors, the effect of the threshold can be seen as a reduction in measured efficiency up to 2.5 MeV for the detectors with the threshold at 900 keV. The measured efficiency using ^{56,60}Co and the calculated curve is shown in Fig. 5.8, with the threshold reduced to 250 keV to eliminate threshold effects in the region of the calibration line. The effect of the threshold was included for the ^{142}Nd transitions at low energies by using the measured efficiency.

Detector Resolution

The detector resolution was determined as a function of incident γ-ray energy from known lines in ^{56}Co and ^{11}B for single crystal summing mode, as can be seen in Fig. 5.9. The resolution will be a function of the detector, the electronics, and the energy calibration because four spectra from different crystals are being added together. The full-width half max (FWHM) of the lines in the summed spectra approaches 5 keV at low energies, and is measured as high

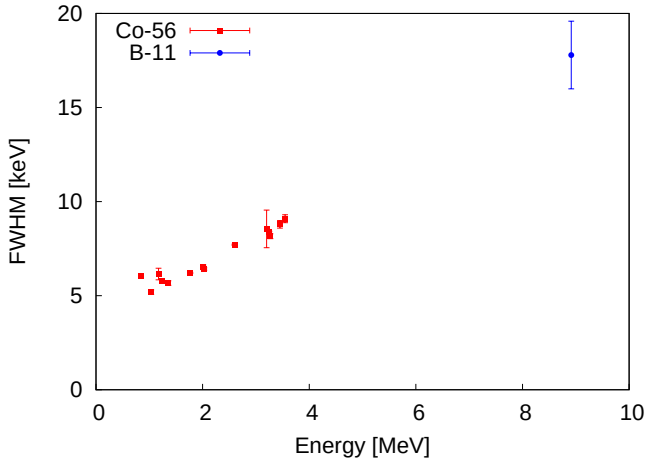

Figure 5.9: The detector resolution of a Clover detector in single crystal summing mode. The FWHM was determined from ^{56}Co and ^{11}B.

as 18 keV for the ^{11}B line at 8.9 MeV. The increasing FWHM of peaks in the spectrum make it difficult to resolve individual states at high energies. The FWHM was calibrated using the known lines in ^{56}Co and ^{11}B, and was used to fit the peaks in the experimental spectra for ^{142}Nd.

Shield Veto

The Clover detectors were operated at all times with the BGO shields. The signals from the shields were amplified using a timing filter amplifier, and then a CFD generated a trigger. The trigger was sent through some delay to the time-to-digital converter (TDC) to obtain the relative timing information. The energy signal of the shields was not digitized. The threshold was set at approximately 200 keV. A TOF gate placed on the shield timing events is used as veto on beam events. By using a gate on the shield timing, only shield events from the same beam pulse as the triggering event in the Clover will be used as a veto on the events. The shield veto was only used for certain cases where it was necessary to improve the signal to background ratio in order to obtain a good peak fit. By looking at the ratio of counts of no shield veto to shield veto of strong transitions, it was determined that the shield veto cuts about

6% of counts in a peak. For the cases where the shield veto was used, a correction of 6% was applied to correct for the over-cutting of the shield.

5.2.4 Monitor Detector

The monitor HPGe detector (see Fig. 5.4) is used for two purposes. The first is to measure the beam profile, and the second is to monitor the flux during an experiment. To measure the beam profile, the beam is first attenuated by the use of Cu blocks which are upstream of the collimator hut. There are six Cu blocks, each 8 cm long. Each block approximately attenuates the beam intensity by one order of magnitude. Typically three or four blocks are used for the beam profile measurements. The detector is positioned so that the center of the beam is approximately 2 cm above the center of the detector. For the E_γ = 9.2 MeV run on ^{142}Nd, the beam energy was measured both before and after the run. The flux dropped during the run which noticeably changed the beam shape, making it narrower.

To measure the flux during an experiment the detector is moved to either 11° or 18° out of the beam. The 11° position was used for ^{142}Nd at E_γ = 3.4, 4.2, and 4.6 MeV. All other runs used the 18° position. The detector moves on a curved track so it is pointing at all times at a Cu plate placed in the beam 165 cm from the front of the detector. The Compton scattering of the γ-ray beam was measured continuously during the experiment. Extracting the flux from the Compton scattering spectrum can be done by either normalizing the count rate using ^{11}B, or using Monte Carlo to simulate a spectrum, and using it to normalize the measured spectrum. Both techniques will be discussed in Sec. 5.3.

5.2.5 Electronics

The basic electronics framework for this experiment was taken from the experiments performed on the tandem for NNSA measurements which typically used 2 Clovers and 2 planars [Hut08a]. In the present setup the two planar detectors were replaced by two more Clovers.

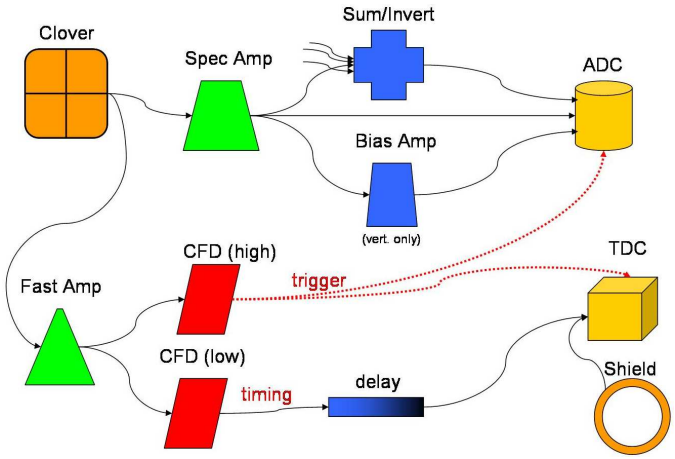

Figure 5.10: A very simplified drawing of the electronics. It shows how the signal for one crystal in a Clover detector progresses, and where the trigger, timing, and energy signals go.

Additional electronics were added for add back mode and to improve the separation of γ-ray peaks. The electronics added were an additional CFD (Constant Fraction Discriminator – model Caen V812) with a very low threshold for timing, Sum/Invert modules for hardware add back, and bias amplifiers to expand the top portion of the spectrum.

Electronics for Add Back

The ADC (Analog to Digital Converter – model Caen V785) works in common gate mode. When it receives a gate, peaks in all channels are digitized simultaneously irrespective of which channel actually generated the trigger. The threshold set for the CFD that generates the trigger is set high so that the annihilation line will not trigger the ADC making the dead time very large. However, if a pulse below the threshold arrives in coincidence with the pulse that generated the trigger, it will also be digitized and read by the computer. The software add back mode takes advantage of this. The various pulses that are digitized in one Clover in one event will then be added together in replay even though only one of the pulses may have triggered the system. The timing information for the pulses below the trigger CFD threshold need to be known in order to determine if the peaks come in coincidence with the triggering event. To

get the timing information a second CFD is used with a threshold set at about 120 keV. The output from the fast amplifier is split into the two CFDs. The output for the high threshold goes into the triggering logic, and the output for the low threshold goes to the TDC (Time to Digital Converter – model Caen V775).

Sum/Invert modules (Ortec 533) for hardware add back were also used. The bipolar output from the amplifier for all four signals from the Clover are sent into the four inputs of a Sum/Invert module. The signals from four detectors were gain matched by adjusting the gains on the amplifiers. Nominally, the Sum/Invert module has a unity gain, but in practice it can vary appreciably from this making it difficult to gain match the signals. The signals were gain matched by looking at the sum signal using an MCA. Only a resolution of 60 keV was achieved for the hardware add back signal because the detectors couldn't be properly gain matched with the available equipment. For software add back, a resolution of 10-15 keV was obtained around 5 MeV.

In the end, add-back mode was not used. The resolution using single crystals was higher, and the add back mode remains insuficiently characterised. MCNP calculations of the efficiency in add back mode were done [Hut08b], but there were large discrepancies between the measured and experimental add back efficiencies. The discrepancies could not be resolved. The problem likely lies in a combination of insufficient Monte Carlo calculation, and issues in how add-back was implemented in the electronics.

Data Acquisition

The data were acquired using the data acquisition system, Spectrodaq [Fox08], developed at the National Superconducting Cyclotron Laboratory. The SpecTcl data analysis program that is included with Spectrodaq was used to monitor the data online. SpecTcl is a complete data replay and analysis program. A scripted version was used in which all hardware definitions, gates, and spectra are generated using the Tcl/Tk programming language. A program was used to convert the Spectrodaq event files into ROOT Tree files offline. Scripted SpecTcl

does have the ability to do event-by-event add back of the data, but it is very slow. A ROOT program was written which replays the data, and generates histograms with cuts applied, with the addition of event-by-event add back. Even with the addition event-by-event add back, ROOT replays data 30–50% faster then scripted SpecTcl without add back.

5.3 Monitor Detector: Beam Profile and Flux

5.3.1 Intro

The monitor detector provides two key quantities: the beam profile, and the flux. The beam profile is needed in order to determine the widths of individual states. In this experiment, the beam profile was obtained from de-convolving the measured beam profile spectrum. Flux is a key quantity to obtaining cross-sections. However, online measurement of the flux is difficult for neutral particle beams, especially γ-rays. For high intensities, no known detector can withstand the intensity of the γ-ray beam, and a HPGe would quickly be damaged. In the present experiment the flux is monitored by measuring the Compton scattering at 18° of the γ-ray beam off of a Cu plate. At HIγS, to simplify the setup, the same detector is used to measure the beam profile and to monitor the flux. The HPGe monitor detector is mounted on a curved rail, and a linear actuator is used to move it.

5.3.2 De-Convolving Beam Profile Spectrum

The beam profile spectrum is measured with a HPGe detector placed directly in the beam, with the beam attenuated by several Cu blocks. The measured spectrum is the true beam profile convoluted with the detector response. Two approaches to deconvolving the spectrum using Monte Carlo are possible. The first approach was covered in a previous section for the (γ, n) experiment (see Sec. 4.3). This section will focus on the second of the two approaches: de-convolution of the measured spectrum [Rus08b].

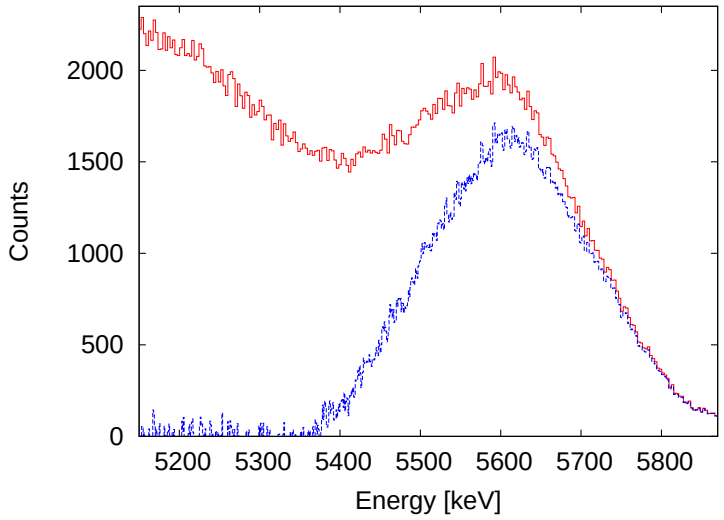

Figure 5.11: The original beam profile spectrum shown with the de-convolved spectrum at E_γ = 5.6 MeV.

By simulating the detector response for a wide range of energies, a complete knowledge of the response function can be obtained over the region of interest. A matrix of the detector response as a function of energy up to 10 MeV is created with Geant3 [Rus08b]. Starting at the last energy bin, the detector response to a single γ-ray is obtained for that energy from the detector response matrix. The detector response is scaled for the number of counts in that bin, and subtracted from the total spectrum. This is repeated for every bin in the spectrum decreasing one-by-one from the last bin. The result is the original beam shape with the detector response removed (see Fig. 5.11).

5.3.3 Flux Normalization from Known Widths in ^{11}B and ^{142}Nd

The (γ, γ') reactions on ^{11}B [AS90] and ^{142}Nd [Vol06], which have peaks with previously measured widths, can be used for absolute normalization of the monitor rate. The analysis procedure laid out in Sec. 5.4 can be also used to obtain the incident flux if the width of the state is already known. This normalization was done for the three ^{11}B calibration runs to obtain the flux at E_γ = 4.4, 5.1, and 8.9 MeV, and for the ^{142}Nd runs at E_γ = 5.4, 5.6, 5.8, 6.0, and

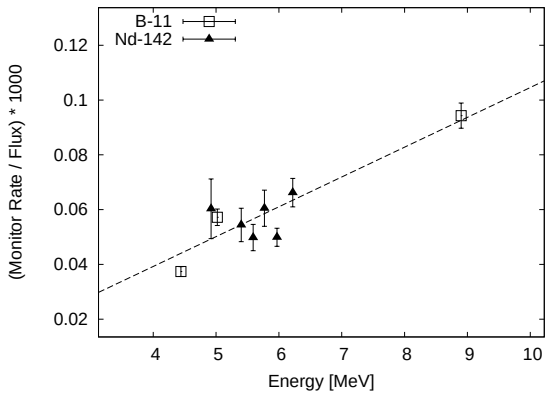

Figure 5.12: The ratio of the flux over the monitor rate times 1000 for $\theta = 18\,^{\circ}$. The monitor spectrum was integrated from 1.8 MeV to the end of the spectrum. The data were fit with a straight line.

6.3. For each of the energies in ^{142}Nd, several states were excited. The γ-ray flux was taken as the weighted mean of the fluxes determined for each of the lines. The calculated flux was used to normalize the count rate in the monitor detector above 1.8 MeV,

$$Q = \frac{N_{mon}}{\phi_{\Gamma}} 10^3 \tag{5.1}$$

where N_{mon} is the number of counts in the monitor detector above 1.8 MeV, and ϕ_{Γ} is the flux determined using the known widths of a level. A straight line was fit to the combined data as seen in Fig. 5.12. The values of the fit are $f(x) = 0.0109 \cdot x - 0.0043$. The data points above 6.3 MeV in ^{142}Nd were not used in this fit. With an increase in excitation energy, more peaks are resonantly excited by the beam, including many peaks which cannot be individually resolved, but their combined effect can be seen. The strong individual states which can be resolved sit on the top of the increasing combined strength of these weaker states, making it difficult to appropriately subtract the background from under the peak. Using a simple locally linear background subtraction for each peak above 6.3 MeV in ^{142}Nd yielded systematically larger than expected peak widths, as comparing to the previous measurements [Vol06]. The ^{11}B points, which do not have background subtraction problems, are consistent with the points from ^{142}Nd below 6.3 MeV as can be seen in Fig. 5.12. Including the points in ^{142}Nd above 6.3

MeV would decrease the ratio by a maximum of 10%. On this basis, the systematic uncertainty of 10% for the procedure was adopted. The normalization using the known widths of states in ^{11}B and ^{142}Nd was used to determine the flux for all runs.

5.4 Analysis

Two different analysis procedures were used for ^{142}Nd and ^{150}Nd targets. For the ^{142}Nd target, the width and parity of the individual states directly excited with NRF were measured. The de-excitation of up to seven low-lying levels, primarily 2^+ states, was also measured (see Fig. 5.1). These states are populated via branching from the initially excited levels, and the observed de-excitation patterns are a signature of the average properties of the those levels. Transitions from the initially excited levels to a level other than the ground state was not directly observed. The E1 and M1 partial cross sections to the ground state were obtained from the intensity of the primary peak. This includes not only the counts from the strong individual peaks, but also the contribution from the many weak states which cannot be individually resolved. The total cross section is obtained from adding the ground state partial cross section and all of the partial cross sections for the transitions from low-lying states.

For the ^{150}Nd target, the transition partial cross sections from the initially excited levels to the ground state were extracted similarly to ^{142}Nd. No individual states were observed in ^{150}Nd, but the total response of many states was measured. The de-excitation of low-lying levels was not observed as the transition energies were below the detection threshold. However, the partial cross sections of transitions from the initially excited levels to three of the low-lying states was measured (see Fig. 5.2).

The data is analyzed as follows. The data is first replayed by converting the event file to a ROOT Tree, and then running a replay program in ROOT. The beam profile is obtained by de-convolving the beam energy measurements taken with the HPGe monitor detector (see Sec. 5.2.4). The observed number of counts is corrected for detector efficiencies, the angular

distribution of the emitted γ-rays from the excited state, the attenuation of the scattered γ-rays in the target and in the Pb attenuators placed in front of the Clover detectors. To obtain partial cross sections in ^{150}Nd, the atomic background was subtracted, and then the detector response to higher energy transitions were subtracted using the ^{142}Nd data. The atomic background is generated by Compton scattering of beam γ-rays, or pair creation. For ^{142}Nd, the pileup of the atomic background extended into the region of the elastic transitions, and had to be subtracted. This section will cover all of these aspects, and describe how the widths and total cross sections are extracted from the data.

5.4.1 Replaying Data

The analysis starts by first replaying the calibration runs using SpecTcl into raw histograms. The spectra are fitted, and the energy calibration for the monitor detector, and all four crystals of each of the four clover detectors is obtained. The calibrations runs used for energy calibration came from measurements using ^{56}Co, ^{60}Co, and ^{11}B. Gates for timing are also determined, as well as for the shield timing. The information for the energy calibration and gates is then put into the ROOT replay program. All runs are replayed using ROOT to obtain energy calibrated spectra for both add-back and single crystal data, with the cuts applied. A binning of 1 keV/bin and 3 keV/bin were used for the December and January runs, respectively.

5.4.2 Dead Time

Determining the dead time correction is usually necessary for absolute cross-section measurements. In this case, the flux is determined from the monitor detector, which uses the same trigger as the clover detectors. The dead time that comes from electronics will then be the same. The major factor that contributes to a dead time comes from acquisition system. In the present setup, all incoming signals, even from different detectors, will have roughly the

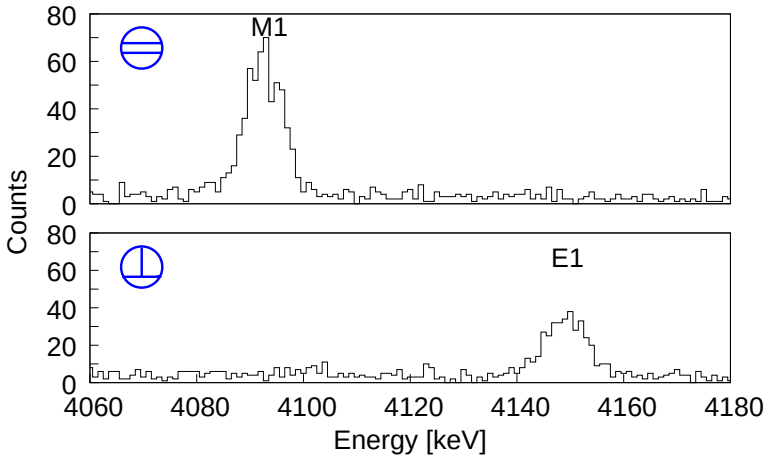

Figure 5.13: ^{142}Nd spectrum at E_γ = 4.12 MeV. Data was taken at during the same run. The top spectrum is from the detectors parallel (horizontal) to the direction of beam polarization. The bottom spectrum is for the perpendicular (vertical) detectors. The separation of E1 and M1 transitions can be clearly seen.

same dead time. The same dead time correction that is used to determine the flux, is used to determine the cross-section. The dead time was monitored by using natural background lines of ^{40}K and Tl.

5.4.3 Angular Distribution

The angular distribution of γ-rays depends on the polarization vector of the incident γ-ray, the J^π of the initial, excited, and final state, and the multipolarity of the transitions. In NRF on even-even nuclei, the excitation and decay of excited states back to the ground state follows the path of $0^+ \rightarrow 1^\pm \rightarrow 0^+$. The excitation of 2^+ states are rarely seen as E2 transitions have a much lower magnitude then E1 or even M1. If the parity of the excited state is positive, the transitions are M1 in nature. If the parity is negative, the transitions are E1. The E1 transition strength is usually much larger than the M1 strength. For 1^- states, the γ-rays will scatter primarily into the vertical detectors, and for 1^+ states, the γ-rays will scatter primarily into the horizontal detectors. These transitions can be clearly distinguished as can be seen in Fig. 5.13. For the given detector geometry, there is no way to distinguish between 1^+ or 2^+ states since

they both predominantly scatter in to the horizontal plane.

To make corrections for the angular distribution for the total counts in the detectors, the percentage increase of counts over spherically symmetric distribution is calculated using a Mathematica program [Wer06]. The formalism for angular distributions in NRF experiments follows directly from that of $\gamma - \gamma$ angular correlations [Kne96]. The correction factor for E1 and M1 transitions is approximately 1.4 enhancement of scattering amplitude over that of a spherically symmetric distribution.

5.4.4 Integrating Peaks

Two methods of peak integrations were used. Discrete lines can be fit directly with a Gaussian profile. This was done with the spectroscopy analysis software Tv [The00]. They come from either the fluorescence of an individual state, or the decay of a low-lying state to which the nucleus has cascaded to. Discrete lines of these types were only seen in ^{142}Nd (see Figs. 5.14 and 5.15). No discrete lines were seen in ^{150}Nd. In each target, the collective response of the decay of many states excited in the nucleus in the region of the beam energy to the ground state was seen. A different method has to be used to extract the total counts for the determining the partial ground state cross section for each target. By extracting the total counts, the many states which do not strongly resonantly fluoresce can be included in determining the total photo absorption cross section.

A general method was adopted for determining the total counts from states excited directly by the beam and decaying to the ground state. This was done at all energies for both targets. First the data is rebinned to 120 keV per channel. The spectrum is integrated from the middle of the peak to the high energy side. The beam profile determined from de-convolution is also rebinned to 120 keV per channel. The beam profile is integrated over the same region as the experimental spectrum. The beam profile ratio of integrated counts to total counts is used to normalize the integrated counts from the experimental spectrum. Different types of background subtraction have to be done for ^{142}Nd and for ^{150}Nd.

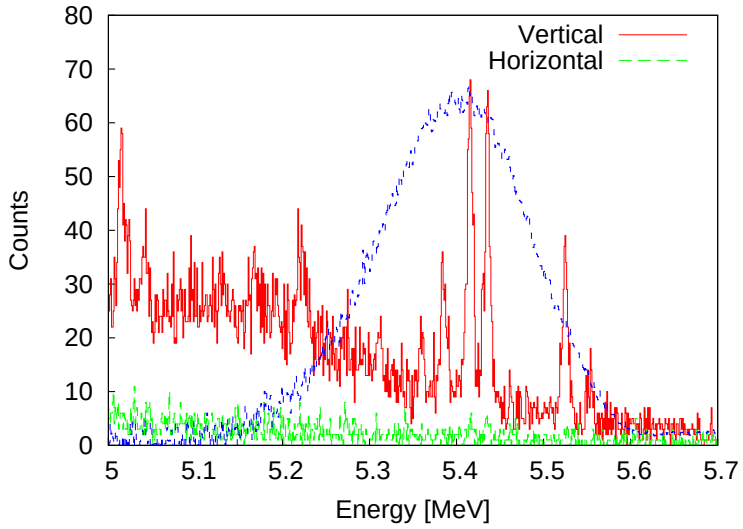

Figure 5.14: Experimental spectrum of ^{142}Nd at E_γ = 5.4 MeV. The spectra for both horizontal detectors and vertical detectors are shown. The decay of several states to the ground state are clearly seen. At this energy, no peaks were seen in the horizontal detectors. The beam profile is overlayed.

^{142}Nd

In the spectra for ^{142}Nd, due to the large mass of the target ($\approx$ 30 g), pileup from the atomic background was present. The background events would pileup extending the background spectrum up to the region of the beam energy and higher, and need to be subtracted from the integrated counts. Two approaches were taken. The first assumed a flat background. The second assumed an exponential tail for the background. The normalized integrated counts from assuming the two different types of background were averaged together. The average difference of the integrated counts between the two methods is 5%. For each of the E1 and M1 components, there were two opposing detectors, giving four points which were averaged together. The uncertainty is taken as the standard error of the four points.

^{150}Nd

In the case for the ^{150}Nd subtraction of the detector response to the scattered γ-rays from higher energy transitions was needed to extract two of the partial cross sections. For ^{150}Nd, the

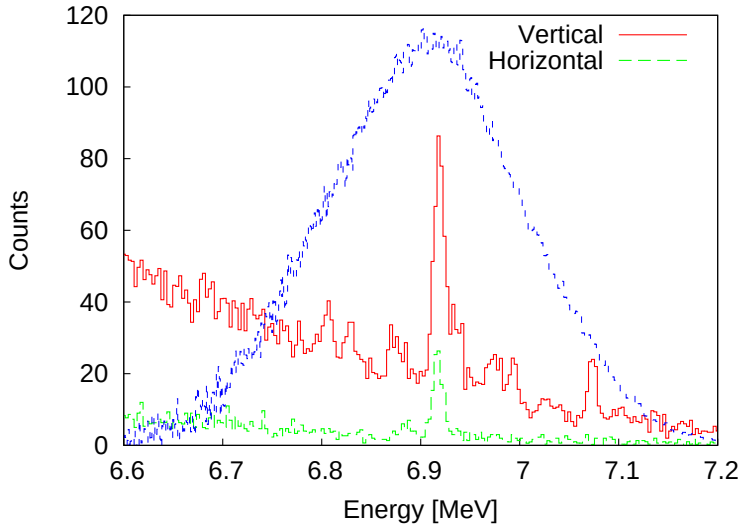

Figure 5.15: Experimental spectrum of ^{142}Nd at E_γ = 6.9 MeV. The spectra for both horizontal detectors and vertical detectors are shown. The background line from ^{16}O is clearly seen in horizontal spectrum at 6.9 MeV. The decay of several states to the ground state are clearly seen, as well as counts which appear to be from unresolved states. The position and strength of the many unresolved states is unknown making it difficult to appropriately subtract background to determine to counts of the resolved peaks. The beam profile is overlayed.

lowest excited states (the first and second 2^+ states at 130 keV and 851 keV, respectively, and the first 0^+ state, at 675 keV) have a relatively low excitation energy (see Fig. 5.2). Transitions to these states will have an energy that is relatively close to the beam energy. To extract these counts, the detector response to the scattered γ-rays from transitions to the ground state and the 130 keV state must be removed. Because of the angular distribution of the γ-rays, transitions to 0^+ states, which follow $0^+ \rightarrow 1^- \rightarrow 0^+$ pattern, will appear primarily in the vertical detectors. Transitions to 2^+ states, which follow $0^+ \rightarrow 1^- \rightarrow 2^+$ pattern, have an angular distribution that is close to isotropic, with a small enhancement in the vertical detectors compared to horizontal detectors ($\approx$ 20%) as determined by calculations (see Sec. 5.4.3). The counts in the horizontal detector will come from transitions to the 2^+ states, as well as M1 transitions to the ground state. The primary peak in the vertical detector will give the partial cross section to the ground state. The primary peak in the horizontal detector corresponds to the transition to the $J^\pi = 2^+$ state at 130 keV as well as M1 transitions to the ground state, and the two cross section can be

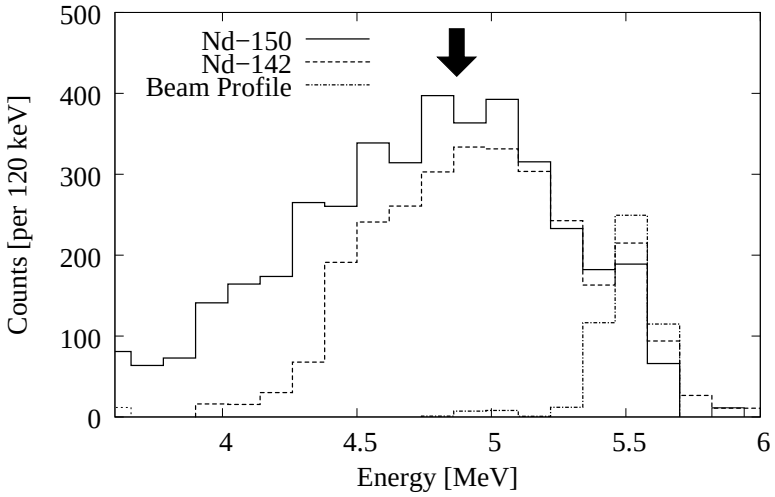

Figure 5.16: The detector response to the transitions to the ground state in ^{150}Nd can be subtracted using the spectrum acquired at the same beam energy for ^{142}Nd. For E_γ = 5.6 MeV, the solid line is the ^{150}Nd spectrum, the dashed line is ^{142}Nd spectrum, and the dot-dashed line is the beam profile. The contributions from the 2^+ transitions has been subtracted from the ^{150}Nd spectrum, and the ^{142}Nd spectrum has been rescaled to that of the ^{150}Nd. There is a clear enhancement above what is expected for the detector response to just γ-rays of the beam energy in ^{150}Nd. The arrow indicates the mean transition energy for branching to the 0^+ state at 675 keV.

obtained because of the 130 keV energy separation between the two.

The transitions to the higher excited states can be extracted by subtracting the detector response to the primary peak (see Fig. 5.16). The next 0^+ state is at 675 keV, and the next 2^+ state is at 851 keV. The detector response to γ-rays of the beam energy can be obtained from the ^{142}Nd data. For each of the five runs taken for ^{150}Nd, there is a run at a similar energy taken for ^{142}Nd. The first excited state in ^{142}Nd is at 1575 keV, so any contribution to the spectrum from branching to the first excited state will be at a lower energy than the transitions of interest in ^{150}Nd. The counts in the region of interest in the ^{142}Nd spectrum will be the detector response to γ-rays resonantly scattered at the energy of the incident beam. As much as possible, spectra from the same detector were matched up for subtracting detector response. For those cases where this was not possible, detectors 1 and 2, and detectors 3 and 4, were paired up, and the necessary spectra were taken from the corresponding detector in the pair.

The procedure adopted is as follows. First, all spectra are rebinned to 120 keV per bin for

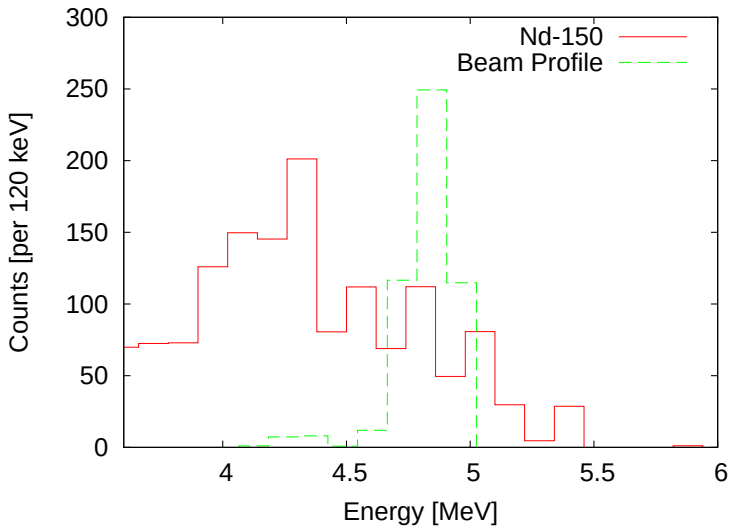

Figure 5.17: The result of subtracting the detector response at E_γ=5.6 that was shown in Fig. 5.16. The beam profi le has been shifted down 675 keV to the energy of γ-rays transitioning to to 0^+ excited state at 675 keV.

both ^{142,150}Nd. Next, the atomic background is subtracted from both the ^{142}Nd spectra, and the ^{150}Nd spectra for all four detectors (see Fig. 5.18). To obtain the yield for the next 0^+ state, the contribution of the 2^+ state is subtracted by scaling the horizontal spectrum by the ratio of the calculated angular distribution, and subtracting it from the vertical detectors. Then the ^{142}Nd spectra, taken at roughly the same beam energy are scaled to the high energy portion of the spectrum, and subtracted. The peak intensities were then obtained in the same way as listed above for the primary peaks, shifting the beam spectrum down the necessary number of bins. For obtaining the next 2^+ state, the ^{142}Nd spectra are shifted down one bin (120 keV), and then the same procedure for rescaling and obtaining counts is used as for the 0^+ case.

Uncertainties

The number of counts were obtained from two detectors in the case of transitions from the initially excited region to ground state or low-lying excited states, or for the case of the decay of low-lying states in ^{142}Nd. The average of the two numbers was used, and the uncertainty comes from the standard deviation of two points. In the case of the counts for the partial cross

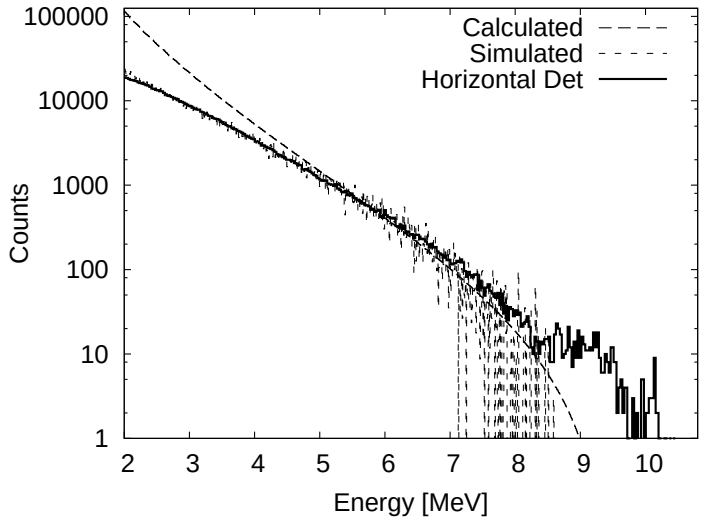

Figure 5.18: The atomic background generated from both a calculation and a Monte Carlo simulation compared to background measured in the horizontal detector at 9.7 MeV. The bump at the end of the spectrum is a small contribution from the E1 strength due to the finite solid angle of the detector.

sections of the decay of low lying excited states in ^{142}Nd, four cross sections were obtained, one from each detector. The weighted mean was calculated from the four points, as well as the uncertainty.

5.4.5 Correcting for E1 and M1 overlap

Due to the finite solid angle of the detectors, a small portion of the M1 strength will be observed in the vertical detectors, and a small portion of the E1 strength will be observed in the horizontal detectors. The contribution needs to be corrected simultaneously in both vertical and horizontal detectors. The overlap, δ, is calculated from the angular distribution for the given solid angle of the detectors (see Sec. 5.4.3). For the geometry used for ^{150}Nd, $\delta \approx .06$, and for ^{142}Nd with the detectors further away, $\delta \approx .04$. The true counts are given by

$$\bar{N_1} = \frac{N_1 - \delta \cdot N_2}{1 - \delta^2} \tag{5.2}$$

where $\bar{N}$ is the true number of counts, and N are the measured counts. Subscripts 1 and 2 stand for either horizontal or vertical counts. Using this correction reduces the M1 cross-section typically by 20-50% and the E1 cross-section by 1-5%.

5.4.6 Cross Sections

With all correction factors in place, the widths and parities of the states can be derived. The parity of the state is determined by the angular distribution of the γ-rays. The width of the states is obtained from the formula for the total intensity of scattering [Kne06]

$$I_{s,f} = g\left(\pi\frac{\hbar c}{E_x}\right)^2 \frac{\Gamma_0\Gamma_f}{\Gamma} \tag{5.3}$$

where g is the statistical spin factor, E_x is the excitation energy of the state, Γ_0 is the decay width to the ground state, Γ_f is the decay width to the final state, and Γ is the total width of the state. The units for intensity are eV·mb. The statistical spin factor is determined from the spins of the initial and intermediate state, $g = (2J + 1)/(2J_0 + 1)$. The intensity is determined from the total counts in the detector from

$$I_{s,f} = \frac{N_p}{N_\gamma\phi(E_\gamma)N_t f\epsilon(E_\gamma)W(\theta)} \tag{5.4}$$

where N_p is the number of full energy peak counts, N_γ is the fluence, $\phi(E_\gamma)$ is the fraction of γ-rays per eV at E_γ, N_t is the aerial density of the target, f is the attenuation coefficient for γ-rays scattered out of the target, $\epsilon(E_\gamma)$ is the efficiency of the detector for the full-energy peak at E_γ, and $W(\theta)$ is the correction for the angular distribution of the γ-rays. Given these two equations, the widths can be extracted. For most cases, the total width, Γ, for a state is not known, so the quantity $\Gamma_0\Gamma_i/\Gamma$ is reported.

To obtain the total (γ,γ') cross-section, Eq. 5.4 is modified slightly. The factor for the beam profile, $\phi(E_\gamma)$, is removed. This gives:

$$\sigma_{(\gamma,\gamma')} = \frac{N_{sum}}{N_\gamma N_t f \epsilon(E_\gamma) W(\theta)}. \quad (5.5)$$

5.5 Experimental Results

Using the techniques laid out in this chapter the following results were obtained. It has been organized into three sections. First the discrete levels seen in ^{142}Nd will be presented and discussed. Following that, the partial cross sections measured will be presented and briefly discussed for ^{142}Nd and ^{150}Nd. The theoretical interpretation for these results will be laid out in Ch. 6.

5.5.1 Discrete Levels in ^{142}Nd

For the ^{142}Nd target the energy, width and parity for 74 states were measured, of which 35 states are observed for the first time. This is the first time that the parity of all of the 74 states has been measured. Only one state was observed to have a $J^\pi = 1^+$ at $E_x = 4094.1$ keV. All other states have $J^\pi = 1^-$. Only one state at $E_x = 4625.5$ keV was seen to directly branch to the first excited state at 1575 keV. Three of the states from previous measurements using a bremsstrahlung beam [Vol06] at $E_x = 5713.8$, 6555.1, and 6586.7 keV, were not observed in this experiment. Given the experimental sensitivity, they should have been observed. Flux normalization were not available for the 3426, 4094, 4145, and 4625 keV states because the monitor spectrum was taken at 11°, and the flux normalization was done for 18° only. The branching to the first 2^+ state of the 4625 keV state was normalized using the previously measured ground state width. The stated widths for observed levels are calculated under the assumption that the integrated peak corresponds to only a single level being excited. Given the relatively poor resolution of the detector at high energies, and the high level density this assumption may not be valid for some of the peaks observed at higher energies, say above 7 MeV. It will also be noted that many of the peak widths do not match the previous experimental

results above 6.5 MeV; they are systematically too large. At higher energies, it becomes noticeable that weak, unresolved states are being excited. The strongly excited peaks will then sit on top of the counts from many weak states. A locally flat background was assumed for all peaks, but this assumption may not hold true, especially if there are many weak peaks of roughly the same energy that are being excited. See App. 7 for the experimental widths.

5.5.2 Partial Cross Sections for ^{142}Nd

The partial cross sections for the elastic transitions, and the decay of states that are populated via branching and cascade, were measured, and are shown in Table 5.1. For the elastic transitions, the E1 and M1 cross sections were determined. No partial cross sections for branching directly from the initially excited states was measured. However, the decay to the ground state of up to seven intermediate states, being primarily low lying 2^+ states, was observed, so branching from the initially excited states can be inferred. The M1 transition observed at 6.89 MeV has been excluded because of contamination from a background line in ^{16}O. The stated uncertainties include statistical uncertainties and the systematic uncertainty of determining the flux. The cross sections of transitions at E = 9.18, 9.45, and 9.68 MeV are scaled down by a factor of 2. The total cross section without the factor would show a large enhancement over the Lorentzian tail of the GDR, but neither the branching ratios nor the shape is consistent with an enhancement. The factor of two brings the total cross section in line with the prediction for the total cross section for the given branching ratios. The origin of the arbitrary enhancement probably lies in the several changes that occurred in the experiment before these runs. Immediately preceding these three runs, the detectors were moved back, more Pb attenuators were placed in front of the detectors, and the beam intensity was reduced. In spite of checking each of these changes, the exact origin of the enhancement remains unknown.

Table 5.1: Measured (γ, γ') cross sections for ^{142}Nd. The partial cross sections are for the E1 and M1 elastic scattering, and for the decay of the listed excited state to the ground state. The cross sections above 9 MeV have been scaled down by a factor of two to be in line with branching ratios and (γ, n) cross sections (see Sec. 6.2). All units, unless otherwise noted, are in mb.

Energy [MeV]	E1	M1	1576 keV	2384 keV	2583 keV	2846 keV	3045 keV	3128 keV	3424 keV	Total
5.59(11)	3.7(4)	0.39(11)	0.57(13)							4.7(5)
5.77(11)	4.8(5)	0.75(17)	0.36(17)							5.9(6)
5.97(11)	10.9(12)	0.81(14)	1.33(18)							13.0(14)
6.22(11)	15.0(16)	0.66(15)	1.10(18)							16.7(17)
6.60(11)	17.1(17)	0.53(13)	3.36(37)	0.51(10)	0.40(9)	0.26(7)				22.0(22)
6.89(11)	17.4(18)		4.01(44)	0.67(11)	0.56(11)	0.48(9)				24.0(24)
7.19(11)	13.4(15)	0.44(13)	4.82(53)	0.66(13)	0.48(12)	0.45(11)				20.3(21)
7.66(14)	27.4(31)	0.56(29)	8.07(85)	1.02(18)	0.95(17)	0.72(15)				38.7(41)
8.17(12)	19.1(22)	0.97(28)	9.02(95)	1.53(22)	0.91(18)	0.91(17)				32.5(35)
8.71(12)	13.3(17)	0.40(15)	11.35(116)	1.70(22)	1.45(19)	0.97(15)	0.29(14)		0.43(14)	30.1(32)
9.18(10)	10.6(12)	0.22(31)	13.78(144)	2.28(25)	1.74(21)	1.67(20)	0.51(21)	0.51(26)	0.59(20)	32.0(33)
9.45(10)	12.9(13)	-0.08(22)	17.97(184)	2.40(24)	2.13(22)	1.36(19)	0.64(29)	0.58(19)	0.60(20)	38.7(39)
9.68(10)	10.0(10)	0.02(42)	18.10(185)	2.27(21)	1.92(19)	1.82(18)	0.58(24)	0.30(18)	0.45(17)	35.3(36)

Table 5.2: Measured (γ, γ') cross sections for ^{150}Nd. The partial cross sections are for the E1 and M1 elastic scattering, and for inelastic scattering to excited states. All units are in mb unless otherwise noted.

Energy [MeV]	E1	M1	$E_x \rightarrow 130$ keV	$E_x \rightarrow 675$ keV	$E_x \rightarrow 851$ keV
5.57(09)	2.91(10)	0.02(8)	0.86(13)	0.73(43)	0.66(10)
5.97(11)	2.49(07)	0.06(5)	0.99(12)	0.83(37)	0.48(11)
6.36(11)	2.09(09)	0.30(12)	0.54(12)	1.05(33)	0.58(22)
6.74(12)	1.87(10)	0.53(21)	0.39(15)		
7.20(14)	1.90(08)	0.33(4)	0.81(13)	1.18(30)	1.17(35)

5.5.3 Partial Cross Sections for ^{150}Nd

The partial cross sections for ^{150}Nd are shown in Table 5.2. The M1 and E1 elastic scattering cross sections were extracted. In addition, the inelastic scattering to three excited states at 130, 675, and 851 keV with J^π of 2^+, 0^+, and 2^+, respectively, was also observed. The depopulation of low lying states branched to was not seen because the transition energies were below that of the detection threshold set at ≈ 1 MeV. No individual states were observed, but the partial cross sections with contributions from many states was observed.

Chapter 6

Results

6.1 Introduction

The data on excitation and de-excitation mechanisms of ^{142,150}Nd has been obtained separately in (γ, n) and (γ, γ') experiments for a wide range of excitation energies. When combined it can bring new insight into nuclear response to radiation. It may lead to new constraints on the tail of the GDR, determine the properties of PRs, and test the statistical model and Brink-Axel hypothesis. First, it will be seen for ^{142}Nd that the total cross section and branching ratios can be used together to constrain the properties of the PR and test the assumptions of the statistical model. Next, using the partial cross sections in ^{150}Nd it will be shown that the data is consistent with calculations using the statistical model including a pygmy resonance at low energies in the γSF. In addition, the data clearly show that the Brink-Axel hypothesis is applicable to a resonance other than the GDR. This is the first time that the statistical model has been tested on this level of sophistication. Finally, the parameters of the PRs determined from the present data will be compared with QRPA calculations to see if they are consistent with the theory of a neutron skin oscillation.

6.2 ^{142}Nd

6.2.1 Total Photo-absorption Cross Section

The ^{142}Nd(γ, n) cross sections and the E1 photoabsorption cross sections are shown in Fig. 6.1. As can be seen on the plot, the best fit to the data is with a standard Lorentzian (SLO) GDR tail augmented with a pygmy resonance (PR) at E_γ = 7.8 MeV. Including a second PR at E_γ = 6.5 MeV appears to fit the data. The enhanced generalized Lorentzian (EGLO – see Eq. 3.4) fit to the (γ, n) cross section around the peak of the GDR doesn't agree with the cross section near threshold. The data at higher E_γ is from the previous measurements by Carlos *et al.* [Car71]. The QRPA calculations done by Goriely [Gor08] are close to the fit using the EGLO model, and is also excluded by the data. Several interesting features arise. First and foremost is the large PR at 7.8 MeV. The second enhancement observed between 6.0 to 6.8 MeV corresponds to the clustering of strong discrete states seen previously in an NRF experiment [Vol06]. By looking at the branching ratios, it can be determined whether or not this enhancement, and the above mentioned PR, should be included in the γSF.

γSF is related to the total photoabsorption cross section by Eq. 3.1, which is:

$$\overrightarrow{f} \equiv \frac{\langle \Gamma_0 \rangle}{D \cdot \mathrm{E}_\gamma^{2L+1}} = \frac{3 \cdot \sigma_\gamma}{(\pi\hbar c)\mathrm{E}_\gamma^{2\mathrm{L}-1}}.$$

According to the Brink-Axel hypothesis, the upward and downward γSF should be equal. Including a resonance observed in the photoabsorption cross section in the γSF means that the effect of the same resonance must be seen in the measurements which probe the downward γSF. The primary example of this is the GDR, which motivated the original Brink-Axel hypothesis [Axe62] (see Sec 3.1.2). A counter example is that of the extreme single particle picture where a single nucleon is excited to a higher shell orbital. Such an excitation should not be included in the γSF as the transition strength between initial and final states will be largely dependent on the unique nuclear wave functions of the two states. Distinguishing

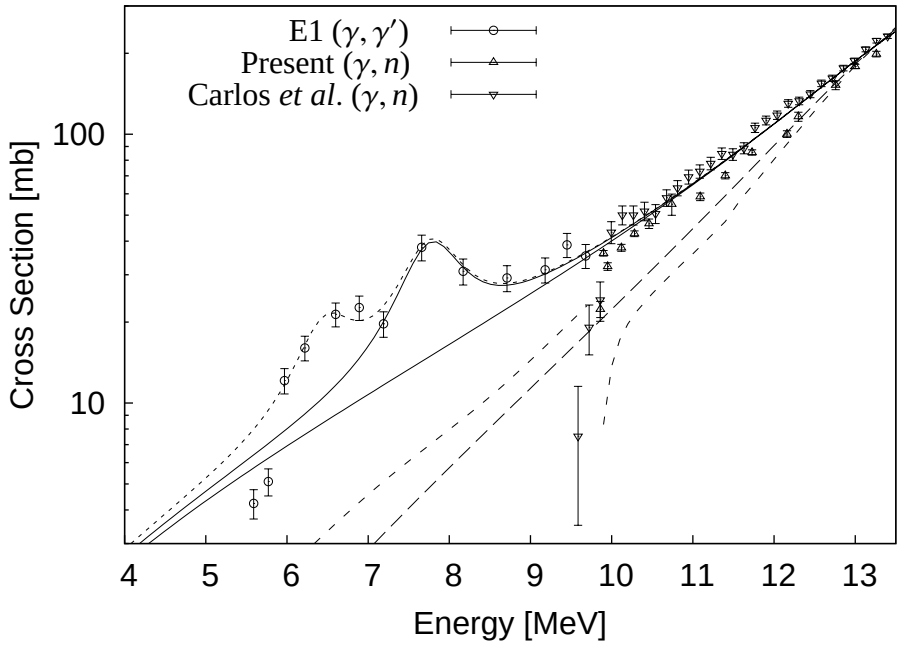

Figure 6.1: The (γ, n) cross section, and the E1 photo-absorption cross section below S_n for ^{142}Nd. The solid lines shows a Lorentzian fit the peak of the GDR, with and without a pygmy resonance. The dotted line shows the same as the solid lines, with the addition of a second pygmy resonance (PR). The long dashed line is a fit to the GDR of a Lorentzian with a temperature dependent width. The short dashed line shows calculations done for ^{142}Nd with the QRPA [Gor08]. Above S_n at 9.8 MeV are calculations for the (γ, n) cross section. Below S_n are calculations for the total photo absorption cross section.

whether or not a particular resonance or enhancement observed in the photoabsorption cross section should be included in the γSF is crucial because any additional resonances can have a strong impact on astrophysical calculations [Rau08].

6.2.2 Branching Ratio

Comparing the measured branching to the ground state, b_0, to calculation can give insight into the nature of the PR. Fig. 6.2 shows the experimental and calculated branching ratios. The branching ratios were calculated using the γSF fitted to the experimental data for a Lorentzian fitted to the giant dipole resonance and for one and two pygmy resonances, using Eq. 3.22 to

calculate to branching ratio, which is

$$\langle b_0 \rangle = \int_0^\infty \frac{3e^{-\alpha\, c}}{(1+2\alpha)^{5/2}} d\alpha, \tag{6.1}$$

and Eq. 3.32 to calculate the quantity c, which is

$$(1+c) = \frac{1}{\sigma_{\gamma T}(E_\gamma)} \left\{ \sum_i \sigma_{\gamma T}(E_\gamma - E_i) f_i^2 + \sum_{J^\pi} \int_{E_{cut}}^{E_\gamma} \sigma_{\gamma T}(E_\gamma - E_i) \left(\frac{E_\gamma - E'}{E_\gamma} \right)^2 \rho(E', J^\pi) dE'. \right\} \tag{6.2}$$

For Eq. 6.2, the known levels with $J^\pi = 0^+$, 1^+, and 2^+ up to the cutoff energy, E_{cut}, are used in the sum. Above E_{cut}, the back-shifted Fermi gas (BSFG) level density formula is used in the integral. First c is calculated using Eq. 6.2, then using c, b_0 is calculated using Eq. 6.1. The level density parameters were fit to the experimental b_0 values by means of Eqs. 6.2 and 6.1. In calculating the b_0 values, it was discovered that the BSFG parameters, a and $E1$, are very strongly correlated. In practice, one of the parameters must be kept fixed in order to do the fit.

For the calculations of b_0 for ^{142}Nd, a cutoff energy of E_{cut} = 2.65 MeV was used, and the BSFG level density parameter a was fit to the experimental b_0 values with and with out the second PR in the γSF. The nearby nucleus, ^{138}Ba has experimentally determined level density parameters. It's low-energy cumulative level density is very similar to that of ^{142}Nd, and has $E1 = 1.12$. For the fit, the $E1$ value for ^{142}Nd was kept fixed at 1.12. The fit for a used the present data above 7 MeV. The calculation including a single PR in the γSF at 7.8 MeV shows agreement with the experimental values over a 3 MeV interval from 7 MeV to 10 MeV. The fit gives a value of $a = 11.4 \pm 0.1$, with $\chi^2/N = 2.0$, where $N = 6$ degrees-of-freedom. For two PRs, the fit was done using the data above 6.5 MeV. A fit value of $a = 10.9 \pm 0.1$ was obtained, with a $\chi^2/N = 5.6$, with $N = 8$ degrees-of-freedom.

The single PR scenario matches the experimental b_0 values remarkably well above 7 MeV. This is the first direct experimental confirmation that the statistical model, and the assumptions associated with the use of a γSF are valid for photon scattering experiments. The situation below 7 MeV is not as clear. The branching ratios below 6.6 MeV clearly do not follow what

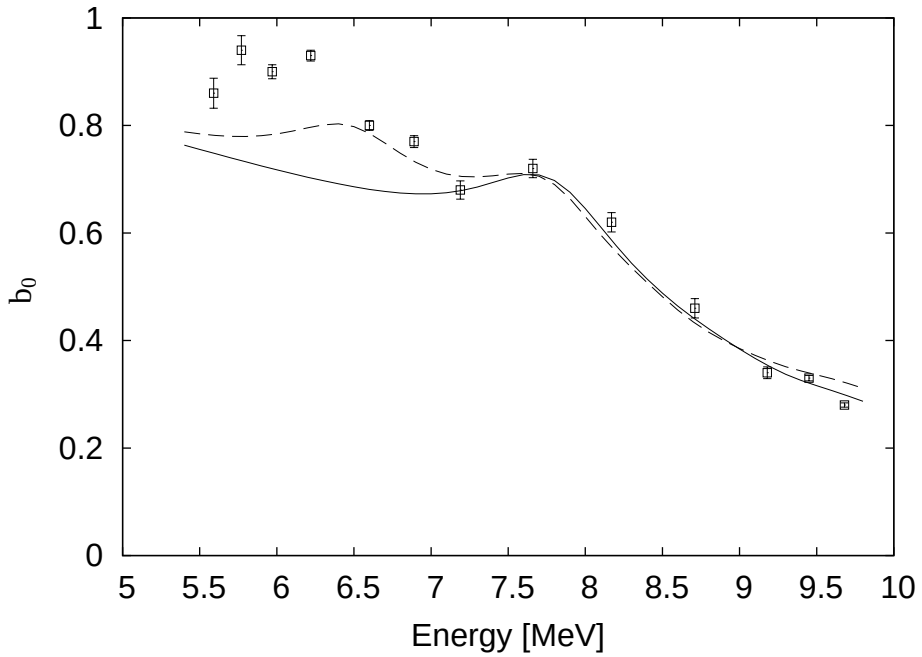

Figure 6.2: The branching ratio of ground state to total cross section. The ratio is calculated following the procedure outlined in Sec. 3.2. Both theoretical lines are calculated using a Lorentzian fit to the GDR. The solid line includes a single PR, and the dashed line is for including two PRs. Different level densities are needed for the two scenarios.

is expected from calculations using either one or two PRs. The b_0 at 6.6 and 6.9 MeV appear to be consistent with having two PRs, but the b_0 values for the energy range from 5.6 to 6.3 MeV are not consistent with either calculation. The total cross section for $E_\gamma = 6.0 - 6.9$ was used to fit the second PR. To include the PR in the γSF, the experimental branching ratios in this region should match the calculated values. Including the second PR also increases the reduced χ^2 from 2.0 to 5.6, and we conclude that the second PR at 6.5 MeV should not be included in the γSF. The parameters for the single PR are listed in Table 6.1.

It was mentioned earlier that the experimental cross sections above 9 MeV were scaled down by a factor of two (see Sec. 5.5.2). The branching ratio is independent of this factor as both the numerator and the denominator are scaled by the same amount, and hence it cancels out. The experimental b_0 values above 9 MeV is consistent with using Lorentzian for the giant dipole resonance with a pygmy resonance at 7.8 MeV, with no additional enhancement

above 9 MeV. A large resonance near threshold is not supported by the cross section for (γ, n) near threshold. It was found that scaling the cross sections down by a factor of 2 satisfied the simultaneous constraint laid down by the b_0 values and the (γ, n) cross sections near threshold (see Sec. 5.5.2).

The branching ratios below 7 MeV suggest that the statistical model is not strictly followed at some point. This is the first experimental evidence that an enhancement in the total photoabsorption cross section should not be included in the γSF. The region from 5.6 to 6.8 MeV is where a pygmy resonance was originally reported in an NRF measurement on ^{142}Nd [Vol06]. The widths of those states have been re-measured, as well as additional states (see Fig. 6.3). It was reported as a pygmy resonance on the basis of a collection of strong individual resonances clustering together around 6.3 MeV and 6.6 MeV. No pygmy resonance was reported around 7.8 MeV while in the experiment no strong, individual states were seen in that region. No branching ratios were measured in that experiment. The measured branching ratios, as seen in Fig. 6.2, indicate that the individual states measured from 5.6 to 6.6 MeV account more than 90% of the photoabsorption cross section, and that they are strongly coupled to the ground state. No branching was detected below 5.6 MeV, and it can be assumed that the excited levels decay almost entirely back to the ground state.

The statistical model calculations use the Porter-Thomas distribution [Por56]. The reduced width amplitudes, or matrix elements, of a state come from the integral of a complex wave function over a large phase space, with effectively $3A$ dimensions, where A is the mass number. Within the Porter-Thomas distribution it is assumed that the wave functions of different states are unrelated, and that the wave functions are extremely complex such that the contribution from various components of the phase space have independent signs and amplitudes. Using the central-limit theorem in statistics, the probability distribution of the matrix elements determined from these complex wavefunctions should be approximately Gaussian. The square of the matrix elements is proportional to the widths. The distribution of level widths is the square of the Gaussian distribution, which is the χ^2 distribution with one degree

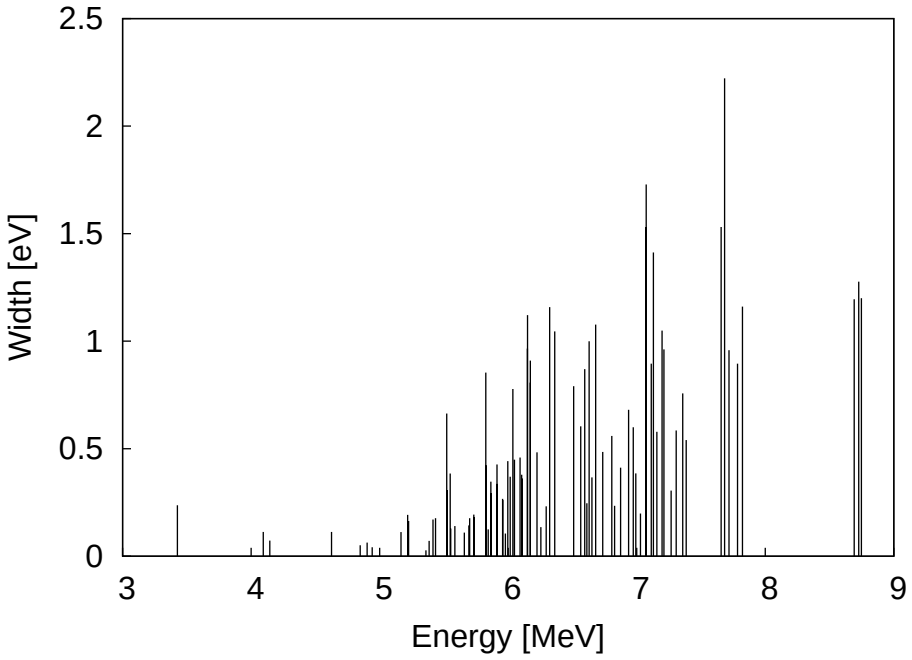

Figure 6.3: The ^{142}Nd ground state, Γ_0, widths. It can be seen that above 7 MeV, fewer and fewer discrete levels are observed. For E_γ = 8.2, 9.2, 9.4, and 9.7 no individual lines were seen; only the total strength was measured.

Table 6.1: Resonance parameters for ^{142}Nd. All resonances were fit to the present data using a standard Lorentzian.

Parameter	GDR	Pygmy	M1 (1)	M1 (2)
E_r [MeV]	14.97(1)	7.78(3)	6.1(1)	8.0(1)
Γ [MeV]	4.43(4)	0.86(9)	1.1(2)	1.0(3)
σ_0 [mb]	359(2)	24.6(24)	0.8(1)	0.9(2)

of freedom (see. Eq. 3.21), referred to as the Porter-Thomas distribution. If different components of the wavefunctions of a particular state are in fact not independent, then the level widths will not follow that of the Porter-Thomas distribution. The complexity of the wavefunctions for a given level is tied to the level density. When the level density is large, the states can mix and the wave functions become quite complicated. When the level density is small, there are no near by states to mix with, and the wave functions remain relatively simple. The known 1^- states at low energy indicate that there is a parity-dependent effect suppressing negative parity states. There should be relatively little mixing, and the observed states will be strongly coupled to the ground state. The branching ratios for ^{142}Nd suggest that between 6.5 and 7 MeV the level density reaches a point where the assumptions laid out above for the Porter-Thomas distribution become valid.

6.2.3 M1 Photoabsorption Cross Section

The M1 photoabsorption cross section was also obtained for ^{142}Nd, and the results are shown in Fig. 6.4. Two peaks are clearly seen in the data. Two Lorentzian's were used to fit the data, and the fit has a χ^2/N of 0.47 with $N = 7$ degrees-of-freedom. The final parameters from the fit to experimental data are included in Table 6.1.

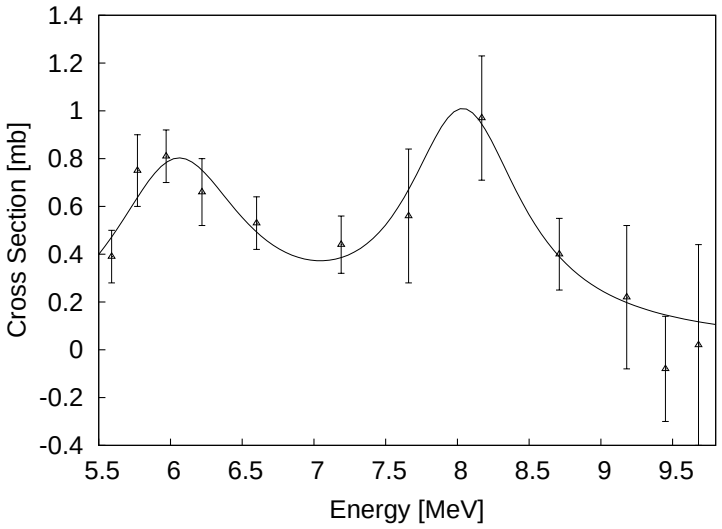

Figure 6.4: The M1 photoabsorption cross section. The solid line is a fit of two Lorentzian's to the data.

6.3 ^{150}Nd

6.3.1 ^{150}Nd(γ, n) Cross Sections

The measured cross sections for ^{150}Nd(γ, n) are shown in Fig. 6.5. This is the first time the (γ, n) cross section has been measured near threshold for ^{150}Nd. The lowest γ-ray energy of the existing data set was 2 MeV above the threshold [Car71]. Both a Lorentzian and an EGLO model were used to fit the combined data set. The low-energy tail of the Lorentzian agrees with the current results near S_n, while the tail from the EGLO model (see Eq. 3.4) under predicts the observed cross section. Including a PR with the EGLO model fit to the GDR matches the experimental cross sections near threshold. The calculations done with the QRPA by Goriely [Gor07] for the photodisintegration cross section agree well with the experimental data.

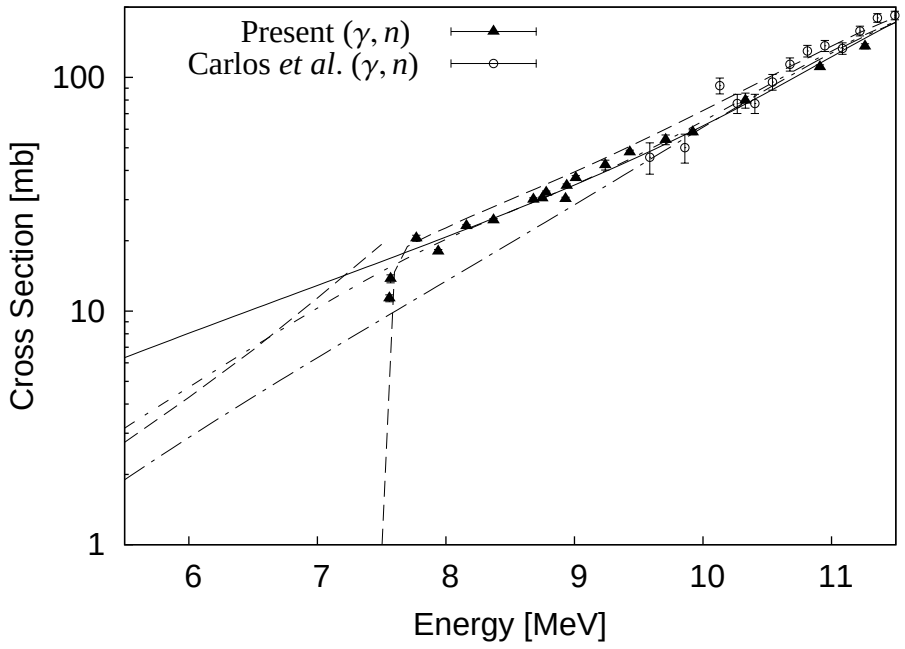

Figure 6.5: The measured ^{150}Nd(γ, n) cross section with previously measured values by Carlos *et al.* [Car71] compared with calculations. The solid line is a Lorentzian fit to the GDR. The long dash-dot line is a fit to the GDR using the EGLO model. The cross section near threshold is clearly under predicted using the EGLO model. Including a PR in the EGLO model can bring it into agreement with the (γ, n) cross sections near threshold, as is shown with the short dash-dot line. A Lorentzian shape was assumed for the PR. The parameters for the pygmy resonance are E_r = 8.25 MeV, Γ_r = 1.37 MeV, and σ_r = 7.5 mb. The QRPA calculations of the (γ, n) cross section above S_n, and the total photoabsorption cross section below S_n by Goriely [Gor07] shown in the dashed line reasonably agree with experimental data.

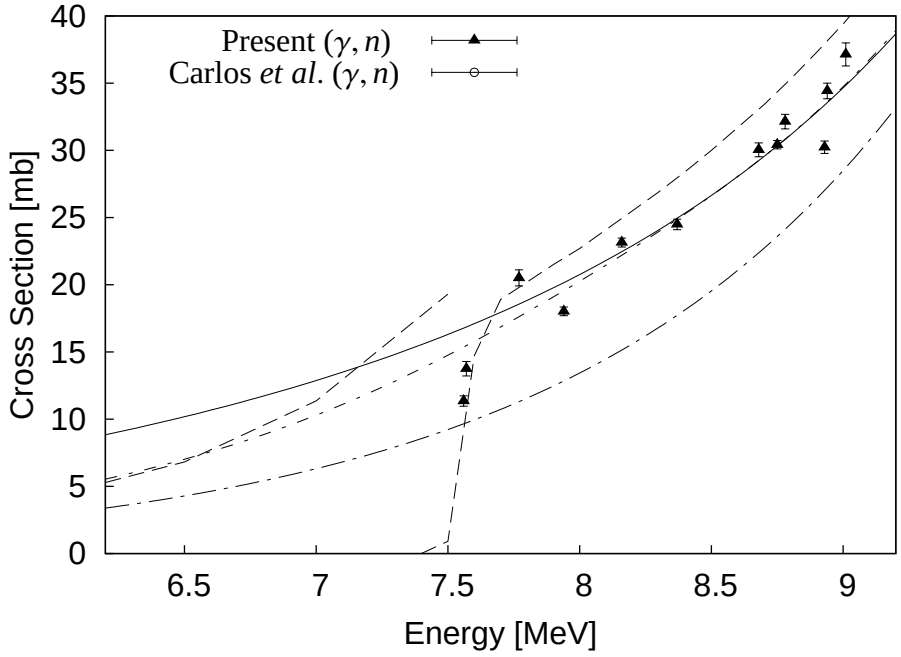

Figure 6.6: The same as Fig. 6.5, except in linear scale. The disagreement of the EGLO model with the measured cross sections near threshold can be clearly seen.

6.3.2 ^{150}Nd(γ, γ') Partial Cross Sections

The partial cross sections measured for ^{150}Nd are presented along with the calculations in Figs. 6.7, 6.8, and 6.9, using a Lorentzian with PR, EGLO with two pygmy resonances, and Lorentzian without PR, respectively. The cross section for the ground state is for E1 transitions only. The partial cross sections were calculated for the various models using methods similar to the one used in the branching ratio calculations in Sec 6.2.2. In the present case, the partial cross sections were calculated using Eq. 3.30, repeated here:

$$\sigma_{\gamma\gamma i} = \sigma_{\gamma T}(E_\gamma - E_i)\frac{R}{1+c} f_i^2, \tag{6.3}$$

with c calculated using Eq. 3.32 (repeated as 6.2), and R calculated using Eq. 3.26, which is:

$$R = \frac{1 + c - E}{c}. \tag{6.4}$$

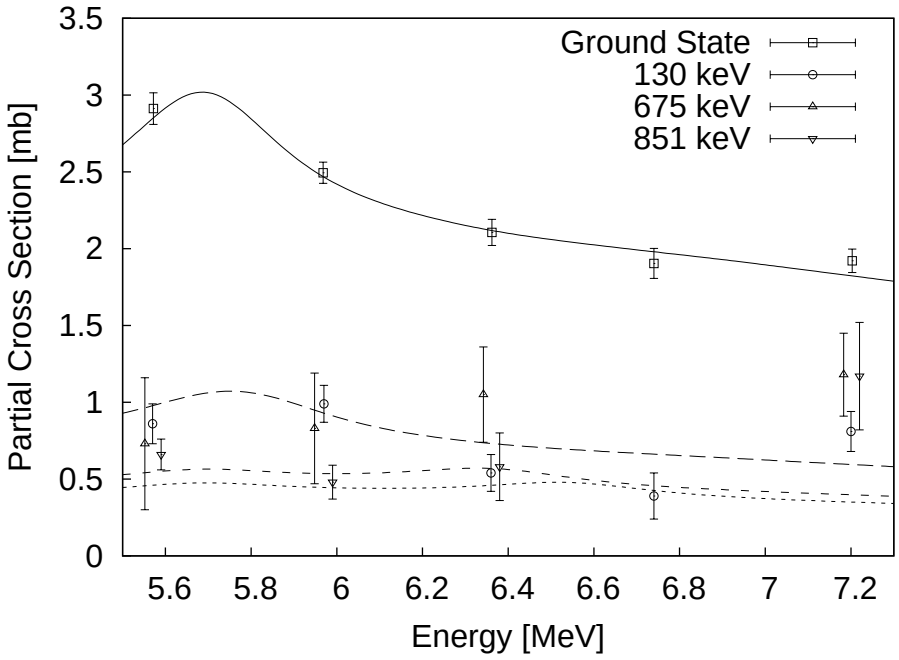

Figure 6.7: The measured partial cross section for ^{150}Nd(γ,γ') to the ground state (E1 only), the first 2^+ state at 130 keV, the first 0^+ state at 675 keV, and the second 2^+ state at 851 keV. The points for the last two transitions are offset on the x axis so that their error bars can be seen. The calculated curves are for using a standard Lorentzian fit to the (γ, n) data, with an addition of a PR at 5.6 MeV. The solid curve represents the calculated partial cross section from the initially excited states to the ground state, the long dash curve is to the 130 keV state, the short dash curve is to the 675 keV state, and the dotted curve is to the 851 keV state.

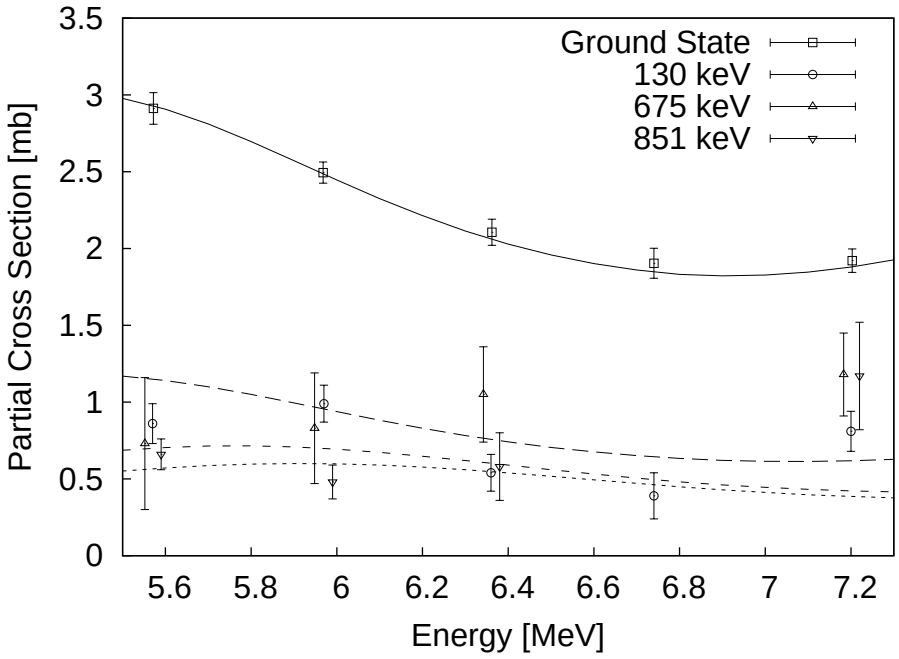

Figure 6.8: The same as Fig. 6.7, except calculations were done with EGLO fi ts to the (γ, n) data with a pygmy near threshold at 8.2 MeV to reproduce the low energy (γ, n) data, and a second PR at 5.6 MeV.

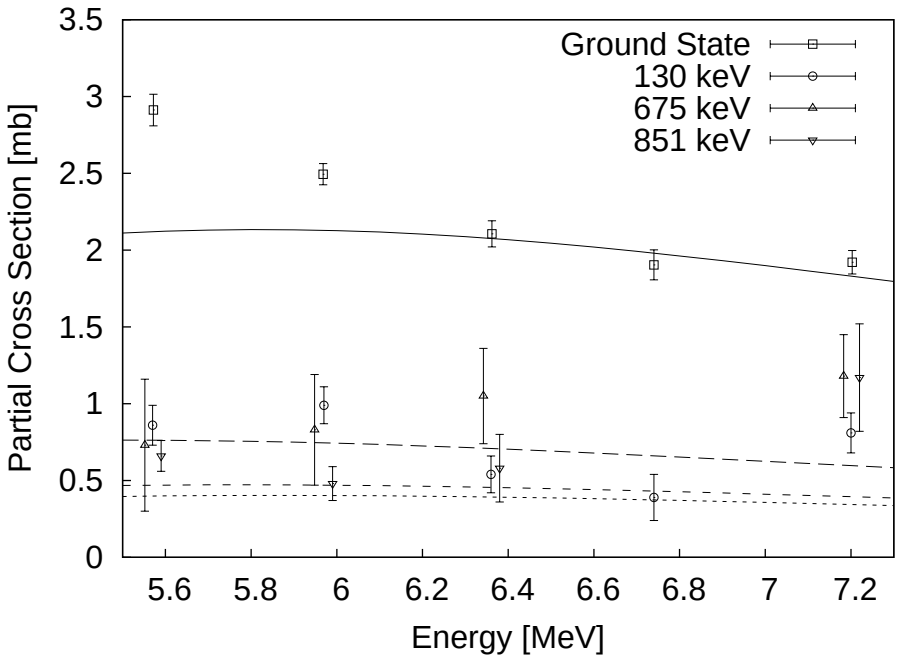

Figure 6.9: The same as Fig. 6.7, no PRs were added.

E is calculated using the following relationship:

$$E = (1 + c)\,\langle b_0 \rangle = (1 + c) \int_0^\infty \frac{3e^{-\alpha\, c}}{(1 + 2\alpha)^{5/2}} d\alpha. \tag{6.5}$$

The cut off energy for the calculations was $E_{cut} = 1.94$ MeV. Below E_{cut} the discrete level scheme was used, and above E_{cut} level densities were used. The value of $E1 = .55$ for the BSFG level density was obtained from systematics [vE05]. The parameters for the pygmy resonances using the SLO model, and the level density parameter a, were fit to the experimental partial cross sections. The partial cross sections to excited states at $E_\gamma = 7.2$ MeV were excluded from the fit as it was found that no combination of models could reproduce the observed ratio between them and the ground state cross section.

An E1 PR included in the γSF around 5.6 MeV is needed to bring calculations in line with the experimental data. Using a Lorentzian fit to the (γ, n) data, the properties of the PR were determined from a fit to the experimental partial cross sections (see Fig. 6.7). The parameters determined from the fit are $a = 15.8 \pm .1$, $E_p = 5.69 \pm 0.03$ MeV, $\Gamma_p = 0.55 \pm 0.09$ MeV, and $\sigma_p = 2.3 \pm .2$ mb. This fit has a $\chi^2/N = 1.5$, with N = 11 degrees-of-freedom.

Using a EGLO fit to the (γ, n) data, and an additional PR at 8.2 MeV, the PR parameters were fit to the partial cross sections (see Fig. 6.8). The parameters determined from the fit are $a = 16.4 \pm .1$, $E_p = 5.52 \pm 0.04$ MeV, $\Gamma_p = 2.14 \pm 0.23$ MeV, and $\sigma_p = 4.5 \pm .2$ mb. This fit has a $\chi^2/N = 1.5$, with N = 11 degrees-of-freedom.

The QRPA calculation is similar to the Lorentzian fit above S_n, however it decreases sharply below S_n, becoming similar to the fit with the EGLO model and one PR. Using the QRPA calculation for the GDR, the parameters of the PR were fit to the experimental data. The parameters determined from the fit are $a = 17.0 \pm .1$, $E_p = 5.47 \pm 0.03$ MeV, $\Gamma_p = 3.0 \pm 0.1$ MeV, and $\sigma_p = 6.3 \pm .3$ mb. This fit has a $\chi^2/N = 1.3$, with N = 11 degrees-of-freedom.

Fits were also performed using no PR below S_n, for both the SLO and EGLO models, varying the level density parameter a. The fit using the SLO yielded a $\chi^2/N = 9.13$, with

$N = 14$ and $a = 15.48 \pm .08$, and can be seen in Fig. 6.9. The fit using the EGLO yielded a $\chi^2/N = 46$, also with $N = 14$ and $a = 15.8 \pm .1$.

It is apparent that a PR around 5.6 MeV is needed to explain the experimental partial cross section regardless of the model used for the GDR. However, very different values for Γ_p, the width, and σ_p, the peak cross section, are obtained depending on the model of the GDR adopted.

The partial cross sections for de-excitation to excited states from 5.6 to 6.8 MeV are reproduced well with the inclusion of a PR. However, the partial cross sections at 7.2 MeV to the excited states don't agree with the calculated values for any scenario. Preliminary calculations show tentative agreement by modifying the Porter-Thomas distribution from $\nu = 1$ to $\nu = 2$ (two degrees-of-freedom). This corresponds to going from predominantly one decay channel to two decay channels. To understand the physical mechanism of having two decay channels to the same state in the radiative decay, it is enlightening to consider the Brink-Axel hypothesis and the GDR (see Sec. 3.1.2). The GDR is a door-way state which almost entirely determines the average reduced radiative decay widths, and hence the distribution of widths at low energies. If a different door-way state is available, or in other words, a second resonance that also follows the Brink-Axel hypothesis, then there are two different distributions of reduced width amplitudes. The reduced width amplitudes are Gaussian distributions about their respective mean values. When squared together, a χ^2 distribution with $\nu = 2$ degrees-of-freedom is obtained. However, this result must be verified by measurements on a wider range of targets before it can be accepted. If verified, it will be definitive evidence, rather than inference, that both the Porter-Thomas and Brink-Axel hypothesis are true for radiative decay widths in heavy nuclei.

The outstanding question is which model to adopt for the description of the GDR. A Lorentzian can reproduce both the (γ, n) cross sections, and the partial cross section for (γ, γ') with a PR included. The EGLO model with a second PR above S_n added, and the QRPA calculations can do the same and it gives the same quality of fit. However, there is no other

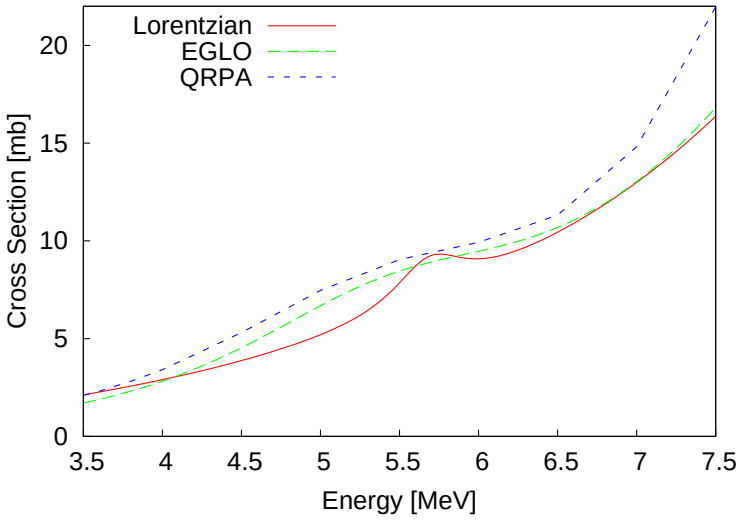

Figure 6.10: The total photoabsorption cross section using different models of the γSF, with pygmy resonances included. The models parameters are fit to the experimental data above 5.6 MeV, and all give roughly the same photoabsorption cross section. Below 5.6 MeV, the models predict very cross sections. There is a roughly 10% difference between the QRPA and EGLO models.

direct evidence for a PR above S_n, and the QRPA calculations will need further testing before being accepted as definitive. There is also no compelling theoretical reason to adopt the EGLO model in the case of ^{150}Nd, as the theoretical calculations using the QRPA agree with the SLO model. The simplest explanation is a single PR, and the SLO model for the GDR, and is the one adopted in the present work. The parameters for all the models have been fit to the data above 5.6 MeV, and the total photoabsorption cross sections are shown in Fig. 6.10. As can be seen, the three models are in rough agreement above 5.6 MeV, but below 5.6 MeV the Lorentzian model gives different total cross sections compared to the EGLO or QRPA, which has similar total cross sections. Further experiments that either measure the strength of the PR below 5.6 MeV will be able to distinguish between the different models.

The remaining question to be asked is whether or not the PR should be included in the γSF. If the partial cross sections to excited states can be explained using only the GDR in the γSF, then an enhancement in the scattering to the ground state should not be included in the downward γSF. A fit was done limited to the partial cross sections to the excited states

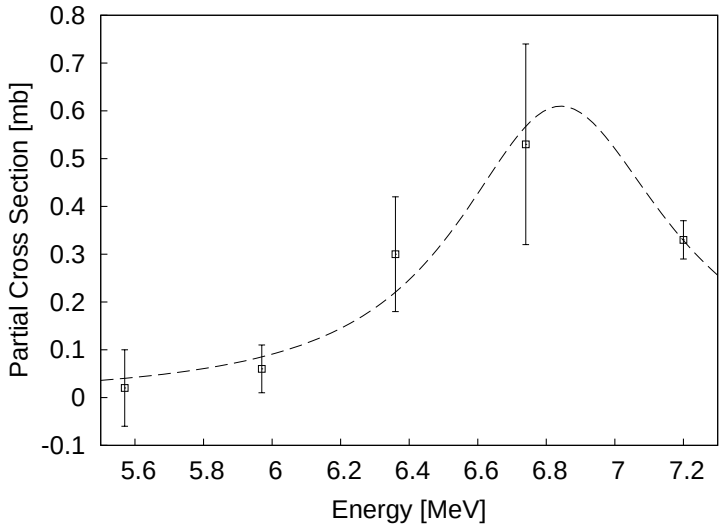

Figure 6.11: The M1 partial cross section for ^{150}Nd with Lorentzian fit to the data.

without a PR for both the SLO and EGLO models. For the SLO, a $\chi^2/N = 2.8$ and $a = 15.5 \pm .4$ was obtained, and for the EGLO, a $\chi^2/N = 7.1$ and $a = 14.9 \pm .5$ was obtained. Both had $N = 9$ degrees-of-freedom. Considering only the partial cross sections to excited states, the fit is worse without a PR. The PR at around 5.6 MeV should be therefore included in both the upward and downward γSF. The parameters for the SLO GDR and the PR are listed in Table 6.2, and for the EGLO GDR, and two PRs, are listed in Table 6.3.

6.3.3 ^{150}Nd M1 Cross Section

In ^{150}Nd, the M1 partial cross section was also measured as seen in Fig. 6.11. The cross sections have been corrected for contributions from E1 transitions due to the finite size of the detectors. A resonance like shape is seen in the data. A Lorentzian was fit to the M1 partial cross sections, and the χ^2/N is 0.61 with $N = 2$ degrees-of-freedom. The results are included in Table 6.2.

Table 6.2: Resonance parameters for ^{150}Nd using the SLO model for the GDR. The E1 PR parameters depend on what model is adopted for the GDR, but the M1 resonances parameters are independent of what model is adopted for the GDR. The pygmy resonances parameters with the QRPA calculations used for the GDR are also presented. All values were obtained from fits to the present data.

Parameter	GDR(1)	GDR(2)	PR (E1)	M1	QRPA
E_r [MeV]	12.3(9)	16.0(1)	5.69(3)	6.84(4)	5.47(3)
Γ [MeV]	2.7(2)	5.1(4)	0.55(9)	0.75(18)	3.0(1)
σ_0 [mb]	178(12)	236(8)	2.3(2)	0.61(14)	6.3(3)

Table 6.3: Resonance parameters for ^{150}Nd using the EGLO model for the GDR. The E1 PR parameters depend on what model is adopted for the GDR. All values were obtained from fits to the present data.

Parameter	GDR(1)	GDR(2)	PR	PR (E1)
E_r [MeV]	12.84(14)	16.37(10)	8.3(3)	5.51(4)
Γ [MeV]	4.6(3)	4.6(5)	3.3(2)	2.75(26)
σ_0 [mb]	203(9)	177(10)	7.1(7)	5.3(2)

6.4 Predictions for Pygmy Resonances

6.4.1 Pygmy Resonance Systematics

Now that the parameters of the PRs have been established for ^{142,150}Nd, the results can be compared to the previous measurements. The discussion will be restricted to the E1 PR. The results of previous experiments that observed the PR were presented in Sec. 3.3.1, with predictions made for ^{142,150}Nd shown in Table 3.1. The PR measured in ^{142}Nd is clearly not in agreement with the predicted values of E_{PR} = 0.9 MeV and σ_0 = .02 mb. However, the PR measured in ^{150}Nd can be considered in agreement with the predicted values of E_{PR} = 4.6 MeV and σ_0 = .7 mb. The experimental results are shown along with the previous measurements in Fig. 6.12 and 6.13 using only the ^{150}Nd PR parameters determined from using a Lorentzian for the GDR. The agreement of ^{150}Nd and disagreement of ^{142}Nd with the previous measurements can be clearly seen.

The agreement observed for the properties of the PR in ^{150}Nd suggests that its underlying structure is the same as to those measured previously with inelastic scattering and neutron capture (see Sec. 3.3.1 and App. 7 for references). The previous measurements using inelastic scattering of ^{3}He and α particles, and neutron capture measured the PR in the downward γSF. In the present experiment both the upward and downward γSF were used to determine the properties of the PR, for the first time, and it was shown that a PR must be included in both γSFs in both ^{142,150}Nd for the calculations to agree with the experimental branching ratios and cross sections. The PRs measured in the previous experiments should also be observed in photon scattering experiments.

The results for ^{142}Nd are clearly not in agreement with the systematics of the previous measurements with inelastic scattering and neutron capture. This suggests that the nature of the PR in ^{142}Nd is different from those measured previously. The previous observations of the PR were in the deformed nuclei, with the exception of closed shell nuclei ^{130,132}Sn which were measured with Coulomb excitation. Both ^{130,132}Sn the $g_{9/2}$ proton shell is closed, and ^{132}Sn

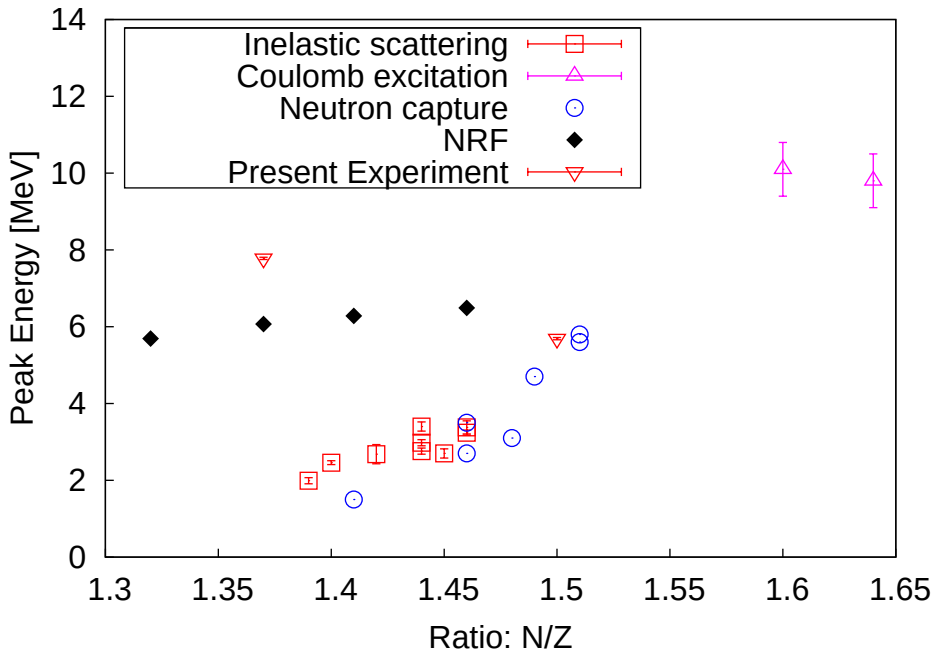

Figure 6.12: The excitation energy of the PR vs. N/Z with previous experiments, and the present experimental results included. ^{142}Nd has N/Z = 1.37, and ^{150}Nd has N/Z = 1.5. The PR energy for ^{150}Nd agrees with previous the PR measured in inelastic scattering and neutron capture (see Sec. 3.3.1 and App. 7). All models adopted for the GDR in ^{150}Nd require an additional PR at about 5.5 MeV to match experimental data. This energy for this PR is shown, but the second PR required by the EGLO model at 8.3 MeV is not considered in this graph.

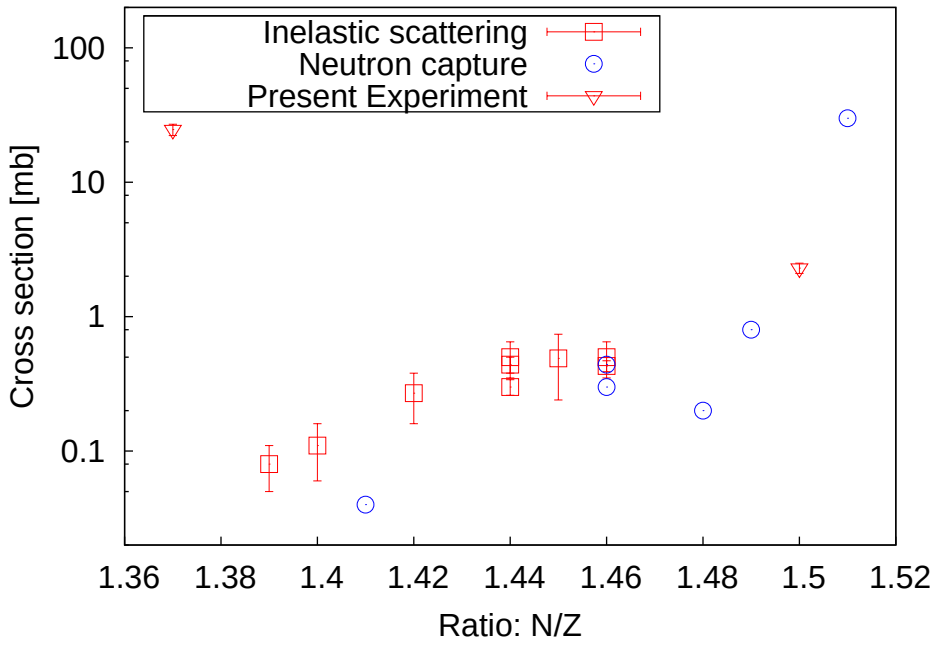

Figure 6.13: The PR peak cross section vs. N/Z with previous experiments, and the present experimental results are included. ^{142}Nd has N/Z = 1.37, and ^{150}Nd has N/Z = 1.5. Considering only the PR parameters determined using the Lorentzian fit to the GDR, the peak cross section for the ^{150}Nd PR agrees with the previous measurements using inelastic scattering and neutron capture (see Sec. 3.3.1 and App. 7).

is doubly-magic with the $h_{11/2}$ neutron shell also closed. The nature of the PR in ^{130,132}Sn may be the same as that in ^{142}Nd, which has the $h_{11/2}$ neutron shell closed, since they are all closed shell nuclei. It should be noted that no excitation mechanism has been unambiguously assigned to any of the PRs that have been previously measured. The primary mechanism that has been suggested has been that of a neutron skin oscillation (see Sec. 3.3). Theoretical calculations are needed in order to understand the nature of the PR, and of the potential effects that a closed shell or deformation may have on the parameters of the PR. The observation of PR in a wide range of nuclear deformations will provide a key test to proposed theories.

6.4.2 Theoretical Calculations

Calculations have been done by Piekarewicz [Pie08] for ^{142,150}Nd using the QRPA. The goal is to see if any additional resonances and low energies (ie below the GDR) is correlated with the development of a neutron skin. The same model was used to study the correlation of a PR with the development of a neutron skin in the tin isotopes using recent measurements of the PR in ^{130,132}Sn [Adr05] as a constraint [Pie06], with the calculations being in agreement with experimental data. The present calculations are shown in Fig. 6.14. No corrections were added for deformation or pairing. Two different models were used in the calculations, the FSU and NL3 models. These models use different density dependence for the symmetry energy. For ^{142,150}Nd, the models give similar results, and the present data cannot be used to distinguish between the two.

In both models, an additional resonance is seen at low energies, and predict about the same energy for the PR. They predict an excitation energy of 8.2 MeV and 7.8 MeV for ^{142}Nd and ^{150}Nd respectively. For ^{142}Nd, the observed PR excitation energy is within 400 keV of the calculations. The PR for ^{150}Nd is observed at 5.6 MeV, which is 2 MeV lower than the value calculated by Piekarewicz, but the using the EGLO model for the GDR would require a PR at 8.3 MeV, which is very close to the predict excitation energy. The present agreement with the ^{142}Nd data is quite remarkable. The three nuclei (^{130,132}Sn and ^{142}Nd) are all closed shell

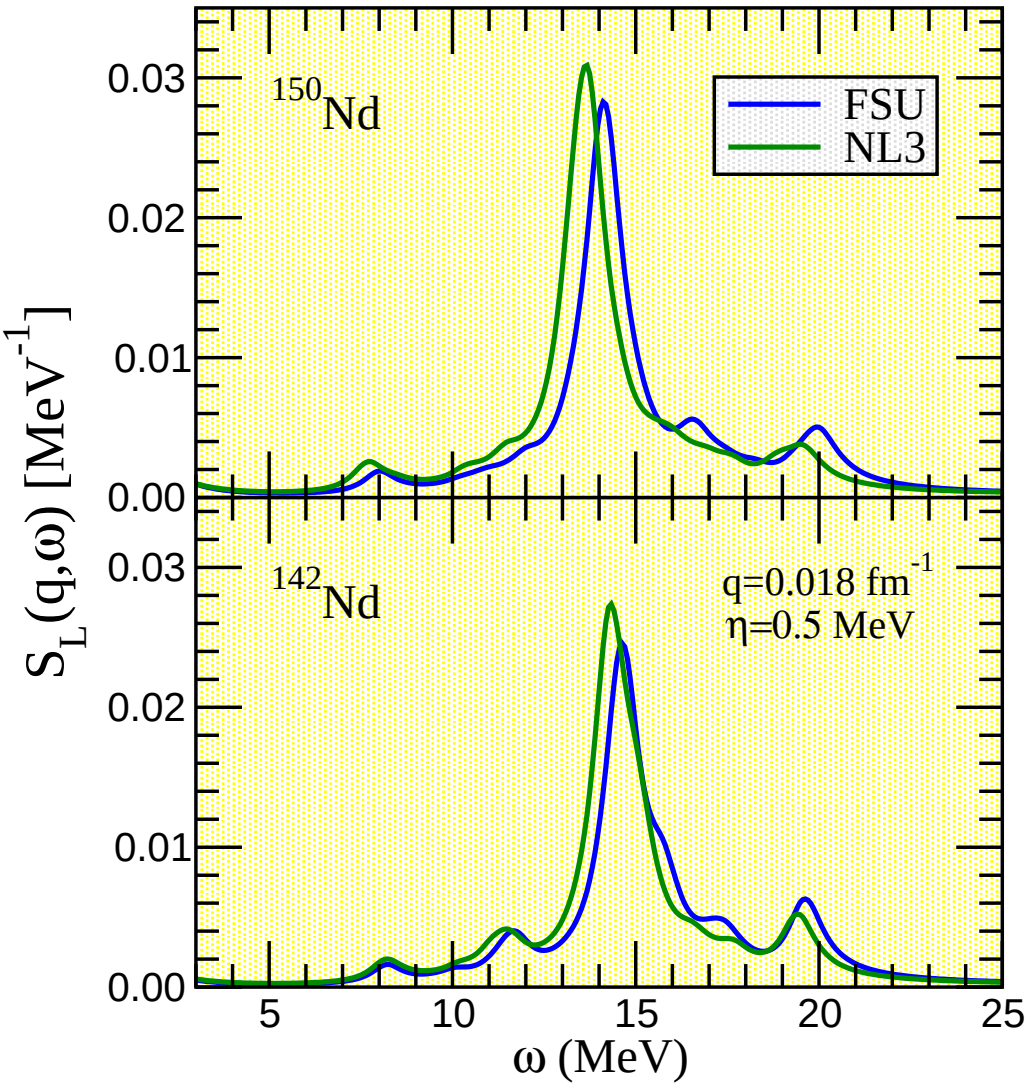

Figure 6.14: Calculations for the γSF in ^{142,150}Nd. The calculations were done by Piekarewicz [Pie08] using the QRPA including the GDR, and neutron skin oscillations. The x-axis is the excitation energy, and the y-axis is the γSF in units of MeV^{-1}.

Table 6.4: The integrated cross sections of the pygmy resonance for both ^{142,150}Nd. The integrated cross section is presented for the several models used for the GDR. Two PR are needed in the case of the EGLO model.

Nucleus	GDR Model	E_{pr} [MeV]	$\int \sigma_{pr} dE$ [mb·MeV]
^{142}Nd	SLO	7.78(3)	33(5)
^{150}Nd	SLO	5.69(3)	2.0(5)
^{150}Nd	EGLO	8.3(3)	37(4)
^{150}Nd	EGLO	5.51(4)	23(2)
^{150}Nd	QRPA	5.47(3)	30(2)

nuclei, with the $g_{9/2}$ shell being closed for the Sn isotopes, and the $h_{11/2}$ shell closed for ^{132}Sn and ^{142}Nd. The additional resonance at low energy may in fact come from the same structural origin, which has been proposed to be a neutron skin oscillation.

Studying the relative strength of the PR between ^{142}Nd and ^{150}Nd may help understand if they have similar structural origin. The FSU model predicts a 17% increase in the PR strength when going from ^{142}Nd to ^{150}Nd, and the NL3 model predicts a 28% increase in strength. However, comparison is slightly complicated because different strengths of the PR in ^{150}Nd are predicted depending on the model adopted for the GDR. The integrated cross sections for the PR for different models of the GDR are shown in Table 6.4. If the Lorentzian is adopted for the GDR in ^{150}Nd, the experimental cross section for the PR is smaller by an order of magnitude in ^{150}Nd than in ^{142}Nd. Using the EGLO model, two PRs are required. The integrated cross section of the PR at 8.3 MeV is comparable to that of the PR in ^{142}Nd, and is in agreement with the prediction from the QRPA calculations. However, a second resonance at 5.5 MeV is not predicted in the calculations. Considering, finally, the PR determined from using the QRPA for the low-energy photoabsorption cross section, the integrated cross section is within uncertainties of the PR of ^{142}Nd, but the excitation energy is at 5.5 MeV. It can be seen that the QRPA calculations do not adequately predict the the PR properties regardless of

the the model used for the GDR. The assumption of a spherical nucleus was made for ^{150}Nd in the calculations, however it is in reality highly deformed. This points to deformation as the likely origin of the disagreement between calculated and observed properties of the PR. Adding deformation may dampen the neutron skin oscillation mode, or having closed shell may enhance the effect. Further experiments on nuclei that are not closed shells themselves, but close to the Z=50 or N=82 shell closure could help to shed more light on this question, along with measurements on successively more deformed nuclei. Such measurements on Sm and Nd isotopes were proposed at HIγS. To remedy the theoretical situation, QRPA models which include deformation are needed [Ter08].

6.5 Conclusions

It has been seen that cross sections from (γ, n) and (γ, γ') experiments can be combined into one consistent data set to provide maximal information of the low-energy γSF. PRs were observed in both ^{142,150}Nd, with the evidence pointing to their nature being collective in origin. The PRs observed must be included in both the upward and downward γSF to be consistent with the observed partial cross sections. It was also seen that a clustering of states that was previously identified as a PR in ^{142}Nd should not be included as a PR in the γSF. It appears that it is probably of single particle origin. This is the first time that such a distinction can be made as to whether or not a particular enhancement should be included as a PR in the γSF. This is also the first time that the statistical model has been shown to be valid in photon scattering experiments. As a result the Brink-Axel hypothesis has been directly tested, and shown to be valid for a resonance other than the GDR. These results were made possible by use of mono-energetic γ-ray beams, and highlights the unique advantage that comes from using combined data from (γ, n) and (γ, γ') experiments in determining the low-energy γSF.

Chapter 7

Conclusions

This dissertation began with the following question in mind: what is the effect of pygmy resonances on p-process nucleosynthesis? The presence of PRs could considerably enhance the photodisintegration reaction rate. However, the effect sensitively depends on their excitation energy, and whether or not they are built on excited states. If a PR cannot be built on the excited states, then it will have little to no effect on the stellar photodisintegration reaction rate. Measuring partial cross sections to both the ground state and excited states in NRF experiments probes the upward and downward γSF simultaneously. Only NRF experiments can be used in this way to determine the key property of PRs of whether or not it must be included in both γSFs. Additionally, extracting the total strength of the PR depends sensitively on the extrapolation of the low-energy tail of the GDR. Cross section measurements of the (γ, n) reaction can be used to constrain this extrapolation, which in turn helps determine the properties of PRs observed in NRF experiments. In this way, (γ, n) and NRF experiments complement each other in the study of PRs.

The (γ, n) cross section measurements were accomplished a the AIST TERAS γ-ray facility in Tsukuba, Japan, in collaboration with the experimental nuclear physics group from Konan U. in Kobe. The ^{142}Nd(γ, n) cross section was measured at 15 energies from just above S_n at E_γ = 9.9 MeV to 13.3 MeV. The ^{150}Nd(γ, n) cross section was measured at 19 energies from just above S_n at E_γ = 7.6 MeV to 11.3 MeV. This is the first time that the ^{150}Nd(γ, n)

cross section has been measured below 9.5 MeV. At the HIγS facility NRF measurements were done on both ^{142,150}Nd targets. For the ^{142}Nd target, the total photoabsorption cross section, and ground state branching ratio, b_0, were measured at 13 energies from 5.6 to 9.7 MeV. The properties of 74 discrete $J = 1$ states were also measured from 3.4 to 8.7 MeV, 35 of which were observed for the first time. This is the first time that the parity of all 74 discrete states has been measured. Only one state at 4094 keV had $J^\pi = 1^+$, all others were $J^\pi = 1^-$.

For ^{150}Nd, the partial cross sections for the de-excitation to the ground state, and to three excited states were measured at 5 energies from 5.6 to 7.2 MeV. A PR was observed in ^{142}Nd at $E_\gamma = 7.8$ MeV, and in ^{150}Nd at $E_\gamma = 5.6$ MeV. Both of the PRs should be included in both the upward and downward γSF. A resonance around 6.5 MeV in ^{142}Nd observed in the total photoabsorption cross section was determined to be due to single particle excitations, and as such should not be included in the γSF. The present experiment is the first time that partial cross sections have been obtained in a model-independent way from NRF experiments. It has also been demonstrated that the statistical model using the Brink-Axel hypothesis, and Porter-Thomas distribution for level widths, can be successfully applied to (γ, γ') reactions.

The determined properties of the PR in ^{142,150}Nd were compared with QRPA calculations by Piekarewicz [Pie08], and with systematics of the properties of the PR from previous experiments (see Sec. 6.4). The excitation energy of the PR in ^{142}Nd agrees with the excitation energy of a resonance seen in the QRPA calculations, as was established before in ^{130,132}Sn [Pie06]. It is thought that this resonance may be the neutron skin oscillation. Comparison with ^{150}Nd is complicated different PR parameters are obtained depending on the model adopted for the GDR. It was seen that regardless of the model adopted for the GDR, PR parameters are not adequately described by the QRPA. The disagreement is likely to arise from the fact that deformation effects were not included in the calculations. However, the PR in ^{150}Nd does agree with the systematics obtained from previous experiments, which include both even-even and even-odd nuclei over a wide range of masses. This implies that it's presence is a property of the nuclear medium, and not due to shell structure effects. If the pygmy resonances in

both ^{142,150}Nd are indeed the neutron skin oscillation, then the data suggests that the neutron skin oscillation may have a strong dependence on deformation. QRPA codes which include deformation are needed to answer this question.

The resonance in ^{142}Nd at 6.8 MeV corresponds to a clustering of individual $J^{\pi} = 1^{-}$ states. It is shown in the present work that those should not be included in the downward γSF. These are most likely single particle states that may correspond to transitions to the $h_{9/2}$ neutron shell. A similar scenario has been suggested for clustering of states observed in ^{112,124}Sn [Bos08]. The measurements made here highlight the importance of measuring the total photoabsorption cross section along with branchings to lower excited states. Strong, discrete states observed in NRF experiments may in fact not correspond to excitations which should be included in the γSF.

The QRPA calculations and systematics from previous experiment are indicative that the PRs in ^{142,150}Nd are collective in nature. It has also been observed in the present experiment that they must be included in both the upward and downward γSF, which means that the Brink-Axel hypothesis is applies to both of these resonances. The Brink-Axel hypothesis originally stated that the GDR can be built on excited states, which has the corollary that the upward and downward γSF are equal, and are determined largely by the GDR. From the present experiment, it is seen that the Brink-Axel hypothesis should be expanded to include the PR, and that only collective excitations should be included in the γSF. That the PR should follow the BA hypothesis is all the more remarkable because there is no theoretical work supporting the hypothesis.

The PRs observed in the present experiments will have an impact on the calculations for the *p*-process. Including the PR will enhance the rates of the photodisintegration reactions proceeding from thermally excited states, which could substantially enhance the total stellar reaction rate. In a recent paper, Rauscher showed that for neutron capture, a PR in the region of 3 to 4 MeV will have the greatest impact on the capture rate [Rau08]. Some of the pygmy resonances thus far observed do fall in this region (see Fig. 6.12). Though small, these reso-

nances will have a considerable impact, particularly on the photodisintegration of neutron rich nuclei. Calculations will have to be done to study the effect of incorporating these resonances of *p*-process reaction rates.

The current measurements could help in guiding future investigations of ^{138}La, and help in evaluating the background of $0\nu2\beta$-decay experiments using ^{150}Nd. The QRPA calculations of the neutron skin excitation verified by ^{142}Nd suggest that it may be seen with similar strength in all N=82 nuclei. There has been a long standing dilemma of the underproduction of ^{138}La [Arn03]. A resonance of the size of of that seen in ^{142}Nd if it exists in ^{139}La could substantially enhance the photodisintegration reaction rate. NRF measurements on ^{139}La should be done to investigate this possibility. With respect to ^{150}Nd $0\nu2\beta$-decay experiments like SNO++ [Che05], if the pygmy resonance observed in ^{150}Nd is also in ^{151}Nd, as the systematics suggest, then the neutron capture rate on ^{150}Nd will be enhanced. This could significantly increase the background rate.

It is known that there is no theoretical support for the Brink-Axel hypothesis. Observation of a PR which actually follows the Brink-Axel hypothesis is truly remarkable. In summary, these experiments have successfully demonstrated that the properties of PR can be studied in photon scattering experiments in a model independent way.

Appendix A

Tables of Pygmy Resonance Parameters

Experiments measuring the γSF can be broken up into two categories. Experiments that probe the upward γSF do so by measuring the total photoabsorption cross section. This is dominated by (γ, n) cross section measurements. A more exotic approach has recently been taken by Adrich *et.al.*[Adr05] using Coulomb dissociation of in-flight fission fragments as a corollary of (γ, n) to measure the total photoabsorption cross section on the far-from-stability nuclei, ^{130,132}Sn. To measure the photoabsorption cross section below the neutron separation energy, the NRF technique must be used (see Sec. 3.2). Experiments that probe the downard γSF are done by observing the cascade of γ-rays from an initially excited state. According to the Brink-Axel hypothesis, the upward and downward γSF should be equal. The probability of emitting a γ-ray is the same independent of the configuration of the nucleus, and depends only on the γ-ray energy. The measured cascade spectrum from such experiments are a convolution of the level density with the γSF. The level density and the γSF must be fitted simultaneously. Reactions that are have been used for this technique are (n, γ), $(^3He,^3 He')$, and $(^3He, \alpha)$ reactions.

The data gathered via these experiments has been summarized in the accompanying tables. These tables are complete as of December, 2006. The notable exception is pygmy resonances in light isotopes (Z < 30). These have been ommitted as their presence in light isotopes is disputed, and is likely from single particle origins.

Table A.1: Parameters for the Pygmy resonance obtained via neutron capture. All data taken from Igashira *et. al.*[Iga86]. No uncertainties were reported in cited paper.

Nucleus	Reaction	E_{max} [MeV]	Γ [MeV]	σ_{max} [mb]
^{142}Pr	(n,γ)	1.5	0.8	0.04
^{160}Tb	(n,γ)	2.7	1.0	0.30
^{166}Ho	(n,γ)	3.1	1.0	0.20
^{176}Lu	(n,γ)	3.5	1.7	0.44
^{182}Ta	(n,γ)	4.7	1.0	0.80
^{198}Au	(n,γ)	5.6	1.7	30.0

Table A.2: Pygmy resonance parameters observed in the Coulomb dissociation of ^{130}Sn and ^{132}Sn[Adr05]. The integral cross-section of the PDR is given instead of the peak cross-section.

Nucleus	Reaction	E_{max} [MeV]	Γ [MeV]	$\int \sigma_{max}$ [mb MeV]
^{130}Sn	Coulomb	10.1(7)	< 3.4	130(55)
^{132}Sn	Coulomb	9.8(7)	< 2.5	75(55)

Table A.3: Mean energies and $\sum B(E1\uparrow)$ strengths for PDR seen in even-even N=82 isotones[Vol06].

Nucleus	Reaction	E_{mean} [MeV]	$\sum B(E1\uparrow)$
^{138}Ba	NRF	6.49	681(119)
^{140}Ce	NRF	6.28	308(59)
^{142}Nd	NRF	6.07	184(31)
^{144}Sm	NRF	5.69	208(35)

Table A.4: Parameters for the pygmy resonance obtained by ^{3}He induced reactions. Note the different values obtained from different reactions and different data sets.

Nucleus	Reaction	E_{max} [MeV]	Γ [MeV]	σ_{max} [mb]
^{148}Sm[Sie02]	$(^3He, \alpha\gamma)$	1.99(8)	2.5(2)	0.08(3)
^{149}Sm[Sie02]	$(^3He,^3 He'\gamma)$	2.46(5)	1.4(2)	0.11(5)
^{160}Dy[Gut03]	$(^3He, \alpha\gamma)$	2.68(25)	0.9(5)	0.27(11)
^{161}Dy[Voi01]	$(^3He, \alpha\gamma)$	2.69(4)	1.4(2)	0.49(5)
^{161}Dy[Gut03]	$(^3He, \alpha\gamma)$	2.73(12)	1.0(2)	0.42(9)
^{161}Dy[Gut03]	$(^3He,^3 He'\gamma)$	2.86(7)	0.9(1)	0.40(4)
^{162}Dy[Gut03]	$(^3He, \alpha\gamma)$	2.74(22)	0.3(1)	0.78(34)
^{162}Dy[Gut03]	$(^3He,^3 He'\gamma)$	2.61(8)	1.0(2)	0.28(4)
^{162}Dy[Voi01]	$(^3He,^3 He'\gamma)$	2.73(5)	1.4(2)	0.42(4)
^{166}Er[Mel01]	$(^3He, \alpha\gamma)$	2.98(8)	1.3(3)	0.30(4)
^{167}Er[Mel01]	$(^3He,^3 He'\gamma)$	3.24(7)	1.7(2)	0.43(4)
^{171}Yb[Voi01]	$(^3He, \alpha\gamma)$	3.35(6)	1.0(2)	0.65(7)
^{171}Yb[Agv04]	$(^3He, \alpha\gamma)$	3.35(19)	1.0(3)	0.34(6)
^{171}Yb[Agv04]	$(^3He,^3 He'\gamma)$	3.5(1)	0.9(2)	0.50(9)
^{172}Yb[Agv04]	$(^3He, \alpha\gamma)$	3.38(27)	1.0(6)	0.58(29)
^{172}Yb[Agv04]	$(^3He,^3 He'\gamma)$	3.28(18)	1.4(4)	0.48(12)
^{172}Yb[Voi01]	$(^3He,^3 He'\gamma)$	3.48(7)	1.3(2)	0.45(5)

Table A.5: Nuclei in which the PDR has been observed, yet no parameters for it were given. The nuclei are grouped according to the paper in which they were published.

Nucleus	Reaction
^{48}Ca[Har00]	NRF
^{92}Mo[Rus06a]	Bremms
^{98}Mo	Bremms
^{100}Mo	Bremms
^{140}Ce[Sav06]	$(\alpha, \alpha'\gamma)$
^{204}Pb[End03]	NRF
^{206}Pb	NRF
^{207}Pb	NRF
^{208}Pb	NRF

Appendix B

Experimental Widths of Discrete Levels in ^{142}Nd

Table B.6: Measured widths for ^{142}Nd.

Energy [keV]	J^π	Γ_o^2/Γ [meV]	Volz *etal*.[Vol06]
3426.0(2)	1^-		295(44)
4094.1(1)	1^+		112(17)
4144.8(1)	1^-		136(21)
4625.5(2)	1^-		97(16)
Branches to 1576 keV state:			
3049.8(5)		29(4)	
4848.5(3)	1^-	51(7)	
4902.3(2)	1^-	64(8)	78(14)
4942.1(3)	1^-	42(5)	
5166.1(3)	1^-	113(14)	62(12)
5217.4(5)	1^-	192(31)	208(34)

Continued on next page

Table B.6 (*continued)*

Energy [keV]	J^π	Γ_o^2/Γ [meV]	Volz *etal*.[Vol06]
5224.7(6)	1^-	164(29)	
5360.1(8)	1^-	27(5)	
5384.9(4)	1^-	71(9)	69(16)
5414.8(2)	1^-	170(19)	141(24)
5434.6(2)	1^-	177(20)	139(23)
5522.7(2)	1^-	370(34)	459(71)
5549.2(3)	1^-	179(21)	156(28)
5585.0(6)	1^-	140(19)	107(22)
5658.6(7)	1^-	110(17)	150(28)
5696.9(6)	1^-	155(17)	
5734.7(5)	1^-	187(19)	135(26)
5826.3(3)	1^-	457(48)	237(40)
5844.5(10)	1^-	124(21)	
5865.1(4)	1^-	310(31)	136(27)
5913.2(3)	1^-	374(36)	518(82)

Continued on next page

Table B.6 (*continued)*

Energy [keV]	J^π	Γ_o^2/Γ [meV]	Volz *etal*.[Vol06]
5956.9(5)	1^-	265(29)	101(23)
5977.8(12)	1^-	105(20)	
5997.1(4)	1^-	442(52)	305(49)
6016.0(5)	1^-	369(46)	315(51)
6036.1(4)	1^-	777(92)	510(79)
6048.6(6)	1^-	449(63)	308(50)
6091.8(6)	1^-	459(60)	
6108.9(7)	1^-	365(45)	
6150.0(3)	1^-	1035(97)	869(133)
6172.2(4)	1^-	848(84)	874(134)
6224.2(6)	1^-	483(66)	538(85)
6254.7(18)	1^-	135(30)	
6295.9(18)	1^-	232(45)	
6322.1(4)	1^-	1158(148)	1272(194)
6361.7(6)	1^-	1045(150)	891(139)

Continued on next page

Table B.6 (*continued)*

Energy [keV]	J^π	Γ_o^2/Γ [meV]	Volz *etal*.[Vol06]
6509.3(8)	1^-	791(131)	
6564.1(6)	1^-	604(86)	427(72)
6595.5(6)	1^-	870(114)	386(70)
6612.1(20)	1^-	246(56)	261(53)
6630.0(4)	1^-	1000(121)	476(82)
6651.3(11)	1^-	366(61)	209(46)
6680.6(4)	1^-	1077(132)	372(65)
6735.1(8)	1^-	485(80)	512(86)
6806.0(12)	1^-	559(104)	372(68)
6827.4(13)	1^-	234(72)	
6874.0(10)	1^-	411(67)	
6918.2(2)	1^-	2491(281)	
6936.4(7)	1^-	681(92)	283(59)
6972.8(8)	1^-	600(87)	
6992.7(12)	1^-	385(74)	

Continued on next page

Table B.6 (*continued)*

Energy [keV]	J^π	Γ_o^2/Γ [meV]	Volz *etal*.[Vol06]
7029.4(31)	1^-	198(70)	
7072.7(6)	1^-	1645(198)	1075(172)
7113.4(8)	1^-	895(165)	820(135)
7129.5(10)	1^-	1412(218)	
7156.7(8)	1^-	579(96)	
7197.2(8)	1^-	1049(156)	
7211.6(15)	1^-	962(149)	
7267.5(8)	1^-	305(65)	
7306.6(13)	1^-	585(87)	
7357.6(19)	1^-	757(164)	
7384.7(10)	1^-	540(159)	
7656.6(6)	1^-	1531(244)	
7683.7(13)	1^-	2222(296)	
7717.5(15)	1^-	958(164)	
7783.8(16)	1^-	895(177)	

Continued on next page

Table B.6 (*continued)*

Energy [keV]	J^π	Γ_o^2/Γ [meV]	Volz *etal*.[Vol06]
7822.6(18)	1^-	1161(224)	
8691.6(12)	1^-	1195(250)	
8726.9(13)	1^-	1277(213)	
8748.3(19)	1^-	1200(223)	

Bibliography

[Adr05] P. Adrich et al., "Evidence for Pygmy and Giant Dipole Resonances in ^{130}Sn and ^{132}Sn", Phys. Rev. C **95**, 132501 (2005).

[Agv04] U. Agvaanluvsan, A. Schiller, J. Becker, L. Bernstein, P. Garrett, M. Guttormsen, G. Mitchell, J. Rekstad, S. Siem, A. voinov, and W. Younes, "Level densities and γ-ray strength functions in ^{170,171,172}Yb", Phys. Rev. C **70**, 054611 (2004).

[Ala87] R. Alarcon, R. M. Laszewski, A. M. Nathan, and S. D. Hoblit, "Photon scattering from *Zr*90 below neutron emission threshold", Phys. Rev. C **36**, 954 (1987).

[Arn03] M. Arnould and S. Goriely, "The p-process of stellar nulceosynthesis: Astrophysics and nuclear physics status", Physics Reports **384**, 1 (2003).

[AS90] F. Ajzenberg-Selove, Nucl. Phys. **A506**, 1 (1990).

[Axe62] P. Axel, "Electric Dipole Ground-State Transition Width Srength Function and 7-MeV Photon Interactions", Phys. Rev. **126**, 671 (1962).

[Axe70] P. Axel, K. K. Min, and D. C. Sutton, "Intermediate Structure in the Photon Interaction Cross Sections of Sn and Zr", Phys. Rev. C **2**, 689 (1970).

[Ber] M. Berger, J. Hubbell, S. Seltzer, J. Chang, J. Coursey, R. Sukumar, and D. Zucker, "XCOM: Photon Cross Sections Database", http://physics.nist.gov/PhysRefData/Xcom/Text/XCOM.html.

[Ber75] B. L. Berman and S. C. Fultz, "Measurements of the giant dipole resonance with monoenergetic photons", Rev. Mod. Phys. **47**, 713 (1975).

[Beu98] T. Beuschel, J. P. Draayer, D. Rompf, and J. G. Hirsch, "Microscopic description of the scissors mode and its fragmentation", Phys. Rev. C **57**, 1233 (1998).

[Bos08] M. Boswell, Ph.D. thesis, University of North Carolina at Chapel Hill, 2008.

[Bri57] D. Brink, "Individual particle and collective aspects of the nuclear photoeffect.", Nucl. Phys. **A4**, 215 (1957).

[Car71] P. Carlos, H. Beil, R. Bergere, A. Lepretre, and A. Veyssiere, "The giant dipole resonance in the transition region for the neodymium isotopes", Nucl. Phys. **A172**, 437 (1971).

[Che05] M. Chen, "The SNO Liquid Scintillator Project", Nucl. Phys. **B145**, 65 (2005).

[Cra46] H. Cramer, *Mathematical Methods of Statistics*, Princeton University Press, Princeton, 1946.

[End03] J. Enders, P. von Brentano, J. Eberth, A. Fitzler, C. Fransen, R. D. Herzberg, h. Kaiser, L. Kaubler, P. von Neuman-Cosel, N. Pietralla, V. Y. Ponomarev, A. Richter, R. Schwengner, and I. Wiedenhover, "Nuclear Resonance flourescence experiments on ^{204,206,207,208}Pb up to 6.75 MeV", Nucl. Phys. **A724**, 243 (2003).

[Fox08] R. Fox, *Spectrodaq*, NSCL, Michigan State University, East Lansing, MI, USA, 2008.

[Gag06] N. D. Gagunashvili, "Comparison of weighted and unweighted histograms", arXiv:physics/0605123, 2006.

[Gol48] M. Goldhaber and E. Teller, Phys. Rev. **74**, 1046 (1948).

[Gor02] S. Goriely and E. Khan, "Large-scale QRPA calculation of E1-strength and its impact on the neutron capture cross section", Nucl. Phys. **A706**, 217 (2002).

[Gor07] S. Goriely, Private communication, 2007.

[Gor08] S. Goriely, Private communication, 2008.

[Gut03] M. Guttormsen, A. Bagheri, R. Chankova, J. Rekstad, and S. Siem, "Thermal properties and radiative strengths in ^{160,161,162}Dy", Phys. Rev. C **68**, 064306 (2003).

[Gut05] M. Guttormsen, R. Chankova, U. Agvaanluvsan, E. Algin, L. A. Bernstein, F. Ingebretsen, T. Lonnroth, S. Messelt, G. E. Mitchell, J. Rekstad, A. Schiller, S. Siem, A. C. Sunde, A. Voinov, and S. Odegard, "Radiative strength functions in $^{93-98}$Mo", Phys. Rev. C **71**, 044307 (2005).

[Har00] T. Hartmann, J. Enders, P. Mohr, K. Vogt, S. Volz, and A. Zilges, "Measurement of the Dipole and Electric Quadrupole Strength Distributions up to 10 MeV in the Doubly Magic Nuclei ^{40}Ca and ^{48}Ca", Phys. Rev. Lett. **85**, 274 (2000).

[Has08] J. Hasper, S. Muller, D. Savran, L. Schnorrenberger, K. Sonnabend, and A. Zilges, "Investigation of photoneutron reactions close to and above the neutron emission threshold in the rare earth region", Physical Review C (Nuclear Physics) **77**, 015803 (2008).

[Hut07] A. Hutcheson, C. T. Angell, J. A. Becker, M. Boswell, A. S. Crowell, D. Dashdorj, B. Fallin, N. Fotiades, C. R. Howell, H. J. Karwowski, J. H. Kelley, M. Kiser, R. A. Macri, R. O. Nelson, R. S. Pedroni, A. P. Tonchev, W. Tornow, D. J. Vieira, G. J. Weisel, and J. B. Wilhelmy, "Pulsed and monoenergetic beams for neutron cross-section measurements using activation and scattering techniques at Triangle Universities Nuclear Laboratory", Nuclear Instruments and Methods in Physics Research Section B: Beam Interactions with Materials and Atoms, **261**, 369 (2007).

[Hut08a] A. Hutcheson, Ph.D. thesis, Duke University, 2008.

[Hut08b] A. Hutcheson, Private communication, 2008.

[Iga86] M. Igashira, H. Kitazawa, M. Shimizu, H. Komano, and N. Yamamuro, "Systematics of the pygmy resonance in keV neutron capture γ-ray spectra of nuclei with N $\approx$ 82-126", Nucl. Phys. **A457**, 301 (1986).

[Kin57] B. Kinsey, "Nuclear Reactions, Levels, and Specta of Heavy Nuclei", in *Handbuch der Physik*, edited by S. Flügge, volume XL, page 316, Springer-Verlag, Berlin, 1957.

[Kne96] U. Kneissl, H. Pitz, and A. Zilges, "Investigation of Nuclear Structure by Resonance Fluorescence Scattering", Prog. Part. Nucl. Phys. **37**, 349 (1996).

[Kne06] U. Kneissl, N. Pietralla, and A. Zilges, "Low-lying dipole modes in vibrational nuclei studied by photon scattering", Journal of Physics G: Nuclear and Particle Physics **32**, R217 (2006).

[Kop90] J. Kopecky and M. Uhl, "Test of gamma-ray strength functions in nuclear reaction model calculations", Phys. Rev. C **41**, 1941 (1990).

[Kuc98] G. Kuczera and E. Parent, "Monte Carlo assessment of parameter uncertainty in conceptual catchment models: the Metropolis algorithm", Journ. Hydro. **211**, 96 (1998).

[Li06] T. C. Li, N. Pietralla, A. P. Tonchev, M. W. Ahmed, T. Ahn, C. Angell, M. A. Blackston, A. Costin, K. J. Keeter, J. Li, A. Lisetskiy, S. Mikhailov, Y. Parpottas, B. A. Perdue, G. Rainovski, W. Tornow, H. R. Weller, and Y. K. Wu, "First evidence for spin-flip M1 strength in ^{40}Ar", Phys. Rev. C **73**, 054306 (2006).

[Lid06] A. R. Liddle, P. Mukherjee, D. Parkinson, and Y. Wang, "Present and future evidence for evolving dark energy", Phys. Rev. D **74**, 123506 (2006).

[Lit97] V. N. Litvinenko et al., "Gamma-ray production in a storage ring free-electron laser", Phys. Rev. Lett. **78**, 4569 (1997).

[Mak08] A. Makinaga, Ph.D. thesis, Konan University, 2008.

[Mel01] E. Melby, M. Guttormsen, J. Rekstad, A. Schiller, S. Siem, and A. Voinov, "Thermal and electromagnetic properties of ^{166}Er and ^{167}Er", Phys. Rev. C **63**, 044309 (2001).

[Met53] N. Metropolis, A. Rosenbluth, M. Rosenbluth, , A. Teller, and E. Teller, "Equation of State Calculations by Fast Computing Machines", Journ. Chem. Phys. **21**, 1087 (1953).

[Moh03] P. Mohr, M. Babilon, D. Galaviz, K. Sonnabend, K. Vogt, and A. Zilges, "Nucleosynthesis by photon-induced reactions", Nucl. Phys. **A719**, 90c (2003).

[Moh04] P. Mohr, "Photon-induced Reactions in Stars and in the Laboratory: A Critical Comparison", in *AIP Conf. Proc.*, volume 704, page 532, 2004.

[Moh07] P. Mohr, Z. Fülöp, and H. Utsunomiya, Eur. J. Phys. A (2007).

[Mye77] W. D. Myers, W. J. Swiatecki, T. Kodama, L. J. El-Jaick, and E. R. Hilf, "Droplet model of the dipole resonance", Phys. Rev. C **15**, 2032 (1977).

[Ohg91] H. Ohgaki, S. Sugiyama, T. Yamazaki, T. Mikado, m. Chiwaki, K. yamada, R. Suzuki, T. Noguchi, and T. Tomimasu, "Measurement of laser-induced Compton backscattered photons with anti-Compton spectrometer", IEEE Trans. Nucl. Sci. **38**, 386 (1991).

[Pie02] N. Pietralla, H. R. Weller, V. N. Litvinenko, M. W. Ahmed, and A. P. Tonchev, "Parity measurements of nuclear dipole excitations using FEL-generated γ-rays at HIγS", Nucl. Inst. and Meth. A **483**, 556 (2002).

[Pie06] J. Piekarewicz, "Pygmy dipole resonance as a constraint on the neutron skin of heavy nuclei", Phys. Rev. C **73**, 044325 (2006).

[Pie08] J. Piekarewicz, Private communication, 2008.

[Plu07] V. Plujko, I. Kadenko, E. Kulich, S. Goriely, O. Davidovskaya, and O. Gorbachenko, "Verification of Models for Calculation of E1 Radiative Strength", in *Photon Strength Functions and Related Topics*, page 002, 2007.

[Por56] C. E. Porter and R. G. Thomas, "Fluctuations of Nuclear Reaction Widths", Phys. Rev. **104**, 483 (1956).

[Rau08] T. Rauscher, "Astrophysical relevance of gamma transition energies", Physical Review C (Nuclear Physics) **78**, 032801 (2008).

[Rus06a] G. Rusev, E. Grosse, M. Erhard, A. Junghans, K. Kosev, K. D. Schilling, R. Schwengner, and A. Wagner, "Pygmy dipole strength close to particle separation energies — The case of the Mo isotopes", Eur. Phys. J. A **27**, 171 (2006).

[Rus06b] G. Rusev, *Dipole-strengthdistributions below the giant dipole resonance in ^{92}Mo, ^{98}Mo, and ^{100}Mo,* Ph.D. thesis, Technische Universität Dresden, 2006.

[Rus08a] G. Rusev, R. Schwengner, F. Dönau, M. Erhard, E. Grosse, A. Junghans, K. Kosev, K. Schilling, A. Wagner, F. Becvar, and M. Krticka, "Low-energy tail of the giant dipole resonance in ^{98}Mo and ^{100}Mo deduced from photon-scattering experiments", Phys. Rev. C **77**, 064321 (2008).

[Rus08b] G. Rusev, Private Communication, 2008.

[Sav06] D. Savran, M. Babilon, A. M. van den Berg, M. N. Harakeh, J. Hasper, A. Matic, H. J. Wortche, and A. Zilges, "Nature of the Pygmy Dipole Resonance in ^{140}Ce Studied in $(\alpha, \alpha'\gamma)$ Experiments", Phys. Rev. Lett. **97**, 172502 (2006).

[Sch00a] A. Schiller, L. Bergholt, M. Guttormsen, E. Melby, J. Rekstad, and S. Siem, "Extraction of level desnity and γ strength function from primary γ spectra", Nucl. Instr. Meth. **A447**, 498 (2000).

[Sch00b] E. Schreiber, *Measurement of a High-Intensity Gamma-Ray Beam and the Analyzing Power for $^{2}H(\vec{\gamma}, n)p$ Near Threshhold,* Ph.D. thesis, Duke University, 2000.

[Sch07] R. Schwengner, G. Rusev, N. Benouaret, R. Beyer, M. Erhard, E. Grosse, A. R. Junghans, J. Klug, K. Kosev, L. Kostov, C. Nair, N. Nankov, K. D. Schilling, and A. Wagner, "Dipole response of ^{88}Sr up to the neutron-separation energy", Physical Review C (Nuclear Physics) **76**, 034321 (2007).

[Shi05] T. Shizuma, H. Utsunomiya, P. Mohr, T. Hayakawa, S. Goko, A. Makinaga, H. Akimune, T. Yamagata, M. Ohta, H. Ohgaki, Y. W. Lui, H. Toyokawa, A. Uritani, and S. Goriely, "Photodisintegration cross section measurements on ^{186}W, and ^{187}Re, and ^{188}Os: implications for the Re-Os cosmochronology", Phys. Rev. C **72**, 025808 (2005).

[Sie02] S. Siem, M. Guttormsen, K. Ingeberg, E. Melby, J. Rekstad, A. Schiller, and A. Voinov, "Level densities and γ-ray strength functions in ^{148,149}Sm", Phys. Rev. C **65**, 044318 (2002).

[Ski06] J. Skilling, Bayesian Analysis **1**, 833 (2006).

[Ste50] H. Steinwedel and J. Jensen, Z. Naturforsch. **52**, 413 (1950).

[Sun08] C. Sun, Private Communication, 2008.

[Ter08] J. Terasaki, Private communication, 2008.

[The00] J. Theuerkauf, S. Esser, S. Krink, M. Luig, N. Nicolay, O. Stuch, and H. Wolters,

Program Tv, Institute for Nuclear Physics, Cologne, Germany, 2000.

[Ton05] A. P. Tonchev, M. Boswell, C. R. Howell, H. J. Karwowski, J. H. Kelley, W. Tornow, and Y. K. Wu, "The high intensity γ-ray source (HIγS) and recent results", Nucl. Inst. and Meth. B **241**, 170 (2005).

[Tso04] N. Tsoneva, S. Lenske, and C. Stoyanov, "Pygmy Dipole Resonances as a Manifestation of the Structure of the Neutron-Rich Nuclei", Nucl. Phys. **A731**, 273 (2004).

[Uts03] H. Utsunomiya, H. Akimune, S. Goko, M. Ohta, H. Ueda, T. Yamagata, and K. Yamasaki, "Cross section measurments of the ^{181}Ta$(\gamma, n)^{180}$Ta reaction near neutron threshold and the *p*-process nucleosynthesis", Phys. Rev. C **67**, 015807 (2003).

[Uts06] H. Utsunomiya, A. Makinaga, S. Goko, T. Kaihori, H. Akimune, T. Yamagata, M. Ohta, H. Toyokawa, S. Müller, Y.-W. Lui, and S. Goriely, "Photoneutron cross section measurements on the N = 82 nuclei ^{139}La and ^{141}Pr: Implications for *p*-process nucleosynthesis", Physical Review C (Nuclear Physics) **74**, 025806 (2006).

[van92] P. van Isacker, M. A. Nagarajan, and D. D. Warner, "Effect of the neutron skin on collective states of nuclei", Phys. Rev. C **45**, 13 (1992).

[vE05] T. von Egidy and D. Bucurescu, "Systematics of nuclear level density parameters", Phys. Rev. C **72**, 044311 (2005).

[Voi01] A. Voinov, M. Guttormsen, E. Melby, J. Rekstad, A. Schiller, and S. Siem, Phys. Rev. C **63**, 044313 (2001).

[Vol06] S. Volz, N. Tsoneva, m. Babilon, M. Elvers, J. Hasper, R. D. Herzberg, H. Lenske, K. Lindenberg, D. Savran, and A. Zilges, "The photoresponse of stabel N=82 nuclei below 10 MeV", Nucl. Phys. **A**, doi:10.1016/j.nuclphysa.2006.08.012 (2006).

[Wer06] V. Werner, Private Communication, 2006.